TURBINE PLATFORM FILM COOLING EFFECTIVENESS AND ROTATIONAL EFFECT ON INTERNAL COOLING PASSAGES WITH A CONVERGING TIP TURN

A Dissertation

by

ANDREW F CHEN

Submitted to the Office of Graduate and Professional Studies of
Texas A&M University
in partial fulfillment of the requirements for the degree of

DOCTOR OF PHILOSOPHY

Chair of Committee,	Je-Chin Han
Committee Members,	Meinhard Taher Schobeiri
	Waruna Kulatilaka
	Kuang-An Chang
Head of Department,	Andreas A. Polycarpou

May 2018

Major Subject: Mechanical Engineering

ABSTRACT

Through the advancement of gas turbine cooling technologies, gas turbine engines remain one of the most reliable technologies in the aviation and power generation industries. The combined cycle efficiency of a power generation gas turbine is expected to reach 65% by the year of 2020. The internal and external cooling designs of gas turbine components play an essential role in achieving this goal.

In the first part, experimental investigations were conducted on a five-blade linear rotor cascade platform with upstream purge flow, slashface leakage flow, and discrete film cooling using both cylindrical and fan-shaped holes. Detailed film cooling effectiveness distributions were obtained using the pressure sensitive paint (PSP) technique. Parametric studies on the coolant to mainstream mass flow ratio (0.5% - 1%), blowing ratio (0.5 - 1.5), density ratio (1 – 2), or the purge flow swirl ratio (0.6 and 1) were performed. The area-averaged film cooling effectiveness values of the two film hole geometries are compared and discussed. In general, the design with the fan-shaped cooling holes provides better film effectiveness and coverage at higher blowing, density, and momentum flux ratios.

In the second part, heat transfer and pressure measurements were performed in a two-pass rectangular channel with varying aspect ratios: AR = 4:1 in the first pass and AR = 2:1 in the second pass after a 180 deg converging tip turn. In addition to the smooth-wall case, surfaces roughened with 60 deg angled ribs and 45 deg angled ribs with three different rib coverages were investigated. Regionally averaged heat transfer measurement method was used to obtain the heat transfer coefficients on all surfaces within the flow passages. The Reynolds number ranges from 10,000 to 70,000 in the first passage, and the rotational

speed ranges from 0 to 400 rpm. Under a pressurized condition, the highest rotation number achieved was Ro = 0.39 in the first passage and 0.16 in the second passage. The results showed that both heat transfer and pressure coefficients are sensitive to the geometrical and rib design of the channel. More importantly, significant heat transfer reduction was identified on the tip wall under rotation.

ACKNOWLEDGEMENTS

I would like to express my deep gratitude to my advisor, Professor Je-Chin Han, for his support, guidance, and encouragement throughout my graduate study. I would also like to thank my committee members, Dr. Schobeiri, Dr. Kulatilaka, and Dr. Chang, for their kindness and support throughout the course of this research.

Thanks also go to my friends and colleagues and the department faculty and staff for making my time at Texas A&M University a great experience. Special thanks go to Dr. Chao-Cheng Shiau for his collaboration on many projects at the Turbine Heat Transfer Lab and the Turbomachinery Lab; also go to Mr. Zahir Udovicic (Dept. of Aerospace Engineering), Mr. Garrick Garza (Dept. of Physics and Astronomy), and Mr. John Newkirk (Dept. of Mechanical Engineering) for their excellent machining works.

CONTRIBUTORS AND FUNDING SOURCES

Contributors

This work was supported by a dissertation committee consisting of Professor Je-Chin Han, Professor Meinhard Taher Schobeiri, and Professor Waruna Kulatilaka of the Department of Mechanical Engineering, and Professor Kuang-An Chang of the Department of Civil Engineering. All work for the dissertation was completed independently by the student.

Funding Sources

Graduate study was supported by the G. H. Thompson graduate fellowship, the Wilkes Family fellowship, and a fellowship awarded by the University Turbine System Research (UTSR) program administered by the South West Research Institute (SWRI) and sponsored by the Department of Energy (DOE).

This work was made possible in part by the funding from MAN Diesel and Turbo SE, Oberhausen, Germany.

NOMENCLATURE

A	Surface area
AR	Channel aspect ratio
C	Gas concentration by volume
C_{ax}	Axial chord length of the blade
C_p	Coolant specific heat capacity
D	Diameter of the film cooling hole
D_h	Channel hydraulic diameter
DR	Coolant to mainstream density ratio = ρ_c/ρ_∞
e	Rib height
h or HTC	Heat transfer coefficient
HT	Heat transfer
I	Emission intensity of PSP; Momentum flux ratio = $DR*(v_c/v_\infty)^2$
k	Thermal conductivity of coolant
K	Pressure loss coefficient = $2\Delta P/\rho U_b^2$
L	Length of the cooling hole
LS	Leading surface
M	Blowing ratio = $\rho_c v_c/\rho_\infty v_\infty$
$\dot{m}$	Mass flow rate
MFR	Coolant to mainstream mass flow ratio (%)
n	Streamwise region (n = 1 to 12)
Nu	Nusselt number

Nu_0	Reference Nusselt number (Dittus-Boelter correlation)
P	Pressure; Pitch of the cooling holes or rib turbulators
Pr	Prandtl number
Q_{loss}	Heat loss
$Q_{loss,\ no\text{-}flow}$	Heat loss under no-flow (calibration) condition
Q_{net}	Net heat input to the fluid
R	Resistance of the heater
Re	Reynolds number = $\rho U_b D_h/\mu$
Ro	Rotation number = $\Omega D_h/U_b$
SR	Swirl ratio = coolant circumferential velocity / blade tangential velocity
T	Temperature
TS	Trailing surface
U	Internal flow velocity
W	Molecular weight
v	Velocity of external flow or coolant
V	Voltage across the heater
x	Axial distance
x1	Radial distance from the inlet in passage 1
x2	Radial distance from the tip wall in passage 2

Greek Letters

α	Rib angle to the streamwise direction
σ	Scaling factor for heat loss estimation

μ	Dynamic viscosity of the coolant
η	Film cooling effectiveness
ρ	Fluid density
Ω	Rotational speed

Subscripts

∞	Mainstream property
air	Property with air injection
area ave	Area-averaged value
ave	Average value
b	Bulk property
blk	Black or dark condition
c	Coolant
energy	Property obtained by energy balance method
fg	Property with foreign gas injection
inlet	Property at the inlet
inter	Interpolated property
outlet	Property at the outlet
r	Rotating condition
ref	Reference condition
s	Stationary condition
w	Wall

TABLE OF CONTENTS

Page

LIST OF FIGURES

Page

LIST OF TABLES

Page

1. INTRODUCTION

Gas turbine engines are widely used for aircraft propulsion, land-based power generation, and numerous industrial applications. The efficiency of such technology is, therefore, a paramount issue for gas turbine researchers and designers. To achieve a higher thermal efficiency, one way is to increase the turbine inlet temperature (TIT) based on the working principle of gas turbine engines. The TIT of a modern gas turbine engine may exceed 1700 deg C, which is far higher than the yielding temperature of advanced nickel based superalloys. As a result, advanced cooling designs are used to ensure the safety and reliability of the engine. At this high TIT, the combined cycle thermal efficiency reaches 60% or higher. With more research and development, the government, industry and the academia are working together to push the thermal efficiency to over 65% in around year 2020.

The thermal load and temperature of a turbine airfoil can be reduced by two active cooling mechanisms: internal cooling and external (film) cooling, as illustrated in Figure 1. For internal cooling, high-pressure air at a much lower temperature from the compressor stage is sent to the internal passages of the airfoils as shown in Figure 1 (a). Heat is removed from the internal surfaces to the cooling air (coolant). Several techniques can be used to increase the heat transfer rate inside the passages, including artificial roughened surfaces (ribs or pin-fins) and jet impingement cooling. Several parameters that would affect the internal heat transfer of the cooling channels have been identified, such as channel geometry and aspect ratio, rib configuration, rotation, 180 deg turn and turn geometry, and

Reynolds number effects. A comprehensive review of various effects on internal heat transfer can be found in Han et al. [1].

For external cooling, coolant is discharged from the internal cooling passages or plenums into the mainstream through discrete film cooling holes, upstream stator-rotor seal, or the slashface gap as illustrated in Figure 1 (b). Parameters that influence the film cooling effectiveness or distribution include coolant to mainstream blowing ratio (M), density ratio (DR), mass flow ratio (MFR) and momentum flux ratio (I). The swirl effect of the upstream purge flow also influences the purge flow effectiveness and coolant coverage. Other than these flow parameters, the geometrical design of the cooling features plays an important role in the film cooling outcome, such as the hole shape and hole location, etc. A comprehensive review of various effects on film cooling can also be found in reference [1]. Experimental studies on the external film cooling will be presented in Section 2. And it is worthy to note that the content is reprinted from two previously published papers by Chen et al. [2, 3]. Detailed literature survey and experimental methods will be presented in the following sections.

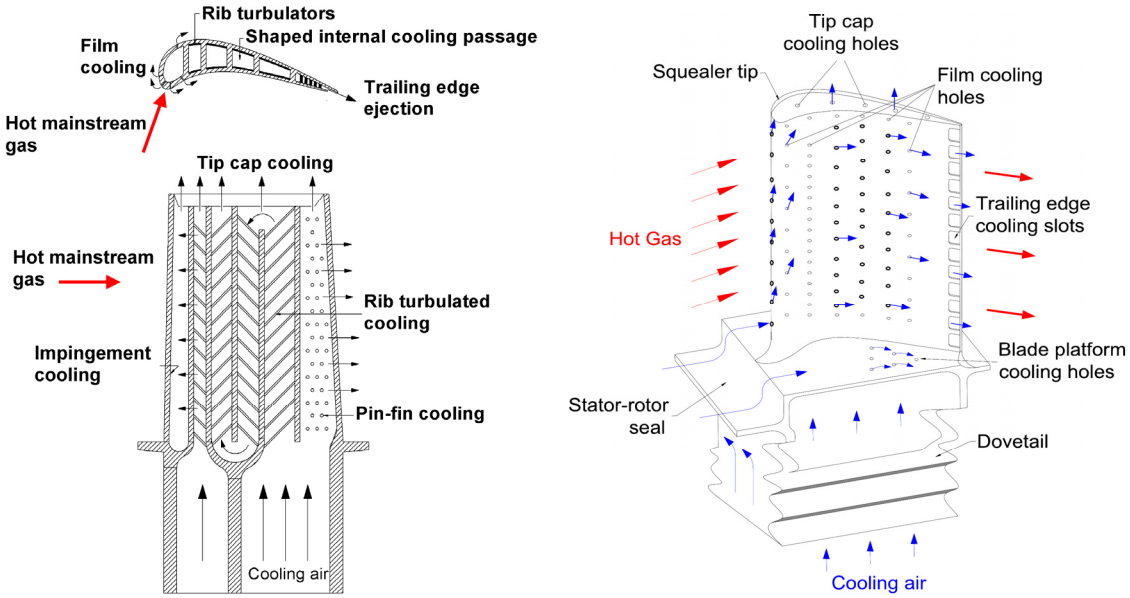

(a) (b)

Figure 1 Typical gas turbine cooling schematic for (a) internal cooling and (b) external (film) cooling. (Reprinted from Han and Rallabandi [54])

2. TURBINE BLADE PLATFORM FILM COOLING WITH SIMULATED SWIRL PURGE FLOW AND SLASHFACE LEAKAGE CONDITIONS

2.1 Literature Survey

As discussed in the introduction, several parametric and geometric effects on the endwall film cooling will be addressed in the literature survey. These parameters include the hole geometry, upstream purge flow, rotation induced purge flow swirl effect, slashface leakage flow, and studies with combined cooling features.

2.1.1 Fundamental Studies

Since the early 1970s, film cooling has become one of the most effective approaches to maintain turbine components in the hot gas path at acceptable temperatures. Han et al. [1] documented comprehensively the key developments in film cooling as well as internal cooling technologies. A general review of gas turbine film cooling can be found in Bogard and Thole [4] and Han [5]. Most of the fundamental research on film cooling was carried out on a flat plate. Goldstein [6] characterized the fundamental flow and heat transfer behaviors of a film cooled flat surface. Chen et al. [7] studied comprehensively the blowing ratio, density ratio, mainstream turbulence and hole geometry effects on flat plate

---

*Reprinted with permission from Andrew F Chen, Chao-Cheng Shiau, Je-Chin Han, 2017, "Turbine Blade Platform Film Cooling With Simulated Swirl Purge Flow and Slashface Leakage Conditions", Journal of Turbomachinery, 139(3), pp. 031012-031012-10, Copyright 2017 by ASME.
And from Andrew F Chen, Chao-Cheng Shiau, Je-Chin Han, 2018, "Turbine Blade Platform Film Cooling With Fan-Shaped Holes Under Simulated Swirl Purge Flow and Slashface Leakage Conditions", Journal of Turbomachinery, 140(1), pp. 011006-011006-11, Copyright 2018 by ASME.

film cooling. In addition, parametric effects on backward injection film cooling can also be found in Chen et al. [8] and Li et al. [9]. Studies on flat plate film cooling may serve as a general guideline for different parametric effects on film cooling. Nevertheless, the results can be quite different when cooling holes are implemented on surfaces of various gas turbine components. Hence, studies on real hardware or a simulated model are essential for a better understanding of film cooling.

Turbine endwall or platform film cooling has been a challenging research topic due to its multiplex geometry and film cooling characteristics that are associated with complex three-dimensional flows in the passages. The mainstream flow adjacent to the platform and coolant trajectories are dominated by the blade induced secondary flows such as horseshoe vortex, passage vortex and passage crossflows. Visualization of secondary flows in a passage can be found in Langston [10, 11] and Wang et al. [12]. An overview of the platform flow and heat transfer can be found in Chyu [13], and Simon and Piggush [14]. Some early studies on discrete-hole endwall film cooling can be found in Refs. [15-17].

2.1.2 Upstream Purge Flow

Several studies on the effects of inlet leakage flow from between the combustor and first stage nozzle guide vane with or without endwall film cooling can be found in Refs. [18-23]. Results showed that the inlet leakage flow could promote film cooling in the upstream endwall, however, endwall film cooling was markedly influenced by the aforementioned secondary flows. Crossflow swiped coolant traces from pressure side to suction side. Horseshoe vortices near the vane leading edge abated the coolant coverage. Some studies [18, 21] demonstrated the use of a contoured endwall to reduce the strength

of the secondary flows and improve film cooling performance. A thinner boundary layer and a vortical structure were seen near the flat endwall at the exit plan ($x/C_{ax} = 1$) and the vortical structure was not seen near the contoured endwall.

Apart from many studies on a first stage vane with inlet leakage flow, a series of studies on a linear rotor blade cascade with inlet purge flow can be seen in Refs. [24-28]. The platform film cooling behavior of purge flow with discrete film cooling holes under various hole geometries and layouts, different coolant density ratios or flow conditions were documented. The results also showed secondary flow (the horseshoe/passage vortices and cross flows) effects and the effects can be more pronounced in a rotor passage. Papa et al. [29] measured the heat and mass transfer on the rotor endwall and blade suction surface in a linear cascade using naphthalene sublimation technique and visualized the flow on the endwall by oil-dot visualization. Takeishi et al. [30] studied the leakage flow effects on flow field and film cooling on a turbine blade platform and found that the strength of secondary flow may be enhanced with leakage flow rate.

2.1.3 Rotation Induced Swirl Effects

In an operating gas turbine engine, the purge flow exiting from the stator-rotor cavity has a circumferential velocity relative to the rotating platform. A rotating facility can be used to study the swirl effects of purge flow. Suryanarayanan et al. [31, 32] studied stator-rotor purge flow through the wheel space cavity of a first stage rotating platform. The facility has a rotational speed up to 3000 rpm. The results showed that the effectiveness on the rotating platform decayed faster than the effectiveness measured on a stationary platform. A continued study by Rezasoltani et al. [33] implemented non-axisymmetric

endwall contouring. The strength of secondary flows was reduced and a higher effectiveness was achieved near the leading edge portion. Schobeiri et al. [34] conducted extensive CFD simulations on the same test facility and similar conclusions were obtained, except that the predicted efficiency and effectiveness values are generally higher than the experimental results.

It has been evidenced that rotation has a significant effect on the rotor platform film cooling. Nevertheless, it is challenging to conduct experiments under a rotating condition in a laboratory setting. Recently, attempts have been made to simulate the swirl motion of the purge flow between the rotor and stator in a stationary test rig. Barigozzi et al. [35] simulated the swirl purge flow by installing a number of inclined fins inside the injection slot. The results showed that the secondary flow near the platform was reinforced and the film cooling coverage was reduced at an injection angle of -10° (simulate the rotation effect). Stinson et al. [36] used turning vanes to impose swirl on the leakage flow. They also found that the film cooling coverage was improved with a higher flow rate and with a decreased swirl effect. Li et al. [37] investigated the purge flow swirl effects as well as the suction surface phantom cooling effects over a wide range of swirl ratios and coolant-to-mainstream MFRs in a linear cascade.

2.1.4 Slashface Leakage Flow

Turbine vane or blade is made of individual casting piece. After assembly, there will be a gap in between the casting pieces on the hub endwall, which allow thermal expansion during service cycles. The gap is also known as slashface gap. A fundamental study on gap flow injection/extraction downstream of film cooling holes was performed by Yu and Chyu [38] on a flat plate. The results demonstrated that a combination of upstream holes and gap could promote film cooling effectiveness under some blowing conditions. Detailed heat transfer and flow measurements on the inlet and slashface leakage flows in a first-stage nozzle cascade were done by Piggush and Simon [39, 40]. They observed an increased heat transfer and passage loss with slashface ejection as compared with a smooth endwall. Several other studies on a first stage nozzle endwall with the combustor-turbine interface, slashface, and film cooling holes can be seen from Refs. [41-45]. These studies showed different gap effects on endwall film cooling: misalignment, roughness, blowing rate, or density ratio effects. One thing in common is that the slashface leakage flow can only be seen at the downstream portion due to high acceleration of the mainstream flow.

2.1.5 Studies with Combined Effects

There are only very limited studies on a rotor blade platform with upstream and slashface gaps. The combined effects of upstream slot film cooling and slashface film cooling was first investigated by Ranson et al. [46]. Roy et al. [47] investigated the combined effect of upstream purge and platform leakage flows on heat transfer and cooling effectiveness. Slashface film cooling was found to have a pronounced effect on downstream suction side platform. More recently, studies on a combination of upstream

purge flow, slashface leakage flow and discrete film cooling on a blade platform can be seen in the open literature. Lynch and Thole [48] investigated the platform gap leakage MFR effect on the endwall film cooling. The area-averaged effectiveness and heat transfer increased with gap leakage MFR from 0% to 0.3% and 0.6%. Many of the aforementioned studies including Refs. [46-48] are based on heat transfer measurement techniques, and the coolant-to-mainstream density ratios are close to 1. Unlike real engine conditions where the coolant-to-mainstream density ratios are close to 2 due to considerable temperature differences.

In the present study, fan-shaped film cooling holes are used in addition to cylindrical holes. There are many studies on shaped hole film cooling on a flat plate, including Refs. [7-9, 49]. Barigozzi et al. [50] studied the MFR effect on the aero-thermal performance of a vane endwall with cylindrical and fan-shaped holes. In terms of effectiveness, shaped holes provide a better coverage and the optimum MFR is higher than the cylindrical holes. Colban et al. [51] investigated the freestream turbulence effect on a vane endwall with cylindrical and fan-shaped holes. A 75% increase in film cooling effectiveness was seen by using fan-shaped holes. Higher turbulence level has a negative effect on shaped hole film cooling. Liu et al. [26] compared cylindrical and fan-shaped hole performances on a blade platform. The results indicated that density ratio has a smaller impact on shaped hole film cooling. Effectiveness increases with blowing ratio for shaped holes. Excellent reviews of shaped hole film cooling on gas turbines were documented by Bunker [52] and Ekkad and Han [53].

2.2 Objectives

This study aims at combining realistic film cooling features on a turbine blade platform. With the newly designed endwall and plenums, sophisticated film cooling schemes can be achieved. High resolution film cooling effectiveness contours and laterally averaged effectiveness are presented and discussed. Film cooling effectiveness comparisons between cylindrical and fan-shaped holes will be made by means of area-averaged effectiveness versus blowing, density, and momentum flux ratios. Parametric effects on backward injection near the blade leading edge, upstream simulated (swirl) purge flow, slashface leakage flow and discrete hole film cooling provide new information for the gas turbine designers and researchers.

2.3 Experimental Setup and Design

2.3.1 Five-blade Linear Cascade

Experiments were conducted in a five-blade linear cascade test facility as shown schematically in Figure 2 and Figure 3. The region of interest on the platform is located next to the pressure side of the center blade. The inlet and exit cross-sections of the wind tunnel were 19.6 cm (width) × 12.7 cm (height) and 12.9 cm (width) × 12.7 cm (height), respectively. The mainstream air was supplied by a centrifugal compressor which can deliver a volume flow rate up to 6.2 m^3/s. The mainstream volume flow rate was regulated by a frequency controller, which has an operational range from 0 to 60 Hz. A 7.62 cm thick honeycomb with a cell size of 1.27 cm was placed 1.78 m upstream of the center blade leading edge to straighten the incoming flow. A planer square bar turbulence grid with a bar width of 0.635 cm was placed 2.5 times of the axial chord length (C_{ax}) upstream of the

center blade leading edge. The grid was perpendicular to the approaching flow and generated an average turbulence intensity of 10.5% at the cascade inlet. The average integral length scale was 0.56 cm, slightly smaller than the bar width. More details regarding the mainstream flow turbulence can be found in Narzary et al. [50]. The cascade inlet and exit velocities were 95 m/s and 153 m/s, measured at $1.35C_{ax}$ upstream of the center blade leading edge and $1.47C_{ax}$ downstream of the center blade trailing edge, respectively by a Pitot-Static probe. The corresponding inlet and exit Mach numbers were 0.26 and 0.43. The cascade inlet and exit Reynolds numbers based on the axial chord length were 4.75×10^5 and 7.2×10^5, respectively. Periodic flow conditions were reached in the middle two passages as reported in previous studies [22, 24]. Some of the key mainstream flow conditions and dimensions of the cascade are listed in Table 1.

Table 1 Cascade geometry and mainstream flow conditions

Cascade Geometry			
Blade height	12.64 cm	Inlet area	249 cm^2
Axial chord length, C_{ax}	8.13 cm	Exit area	164 cm^2
Pitch	7.69 cm	Inlet angle	50.5°
Total turning angle	116.9°	Exit angle	66.4°
Mainstream Flow Conditions			
Inlet Mach No.	0.26	Inlet Re No.	4.75×10^5
Exit Mach No.	0.43	Exit Re No.	7.2×10^5
Pressure Ratio (P_t/P_{exit})	1.16		
Turbulence intensity	10.5%		

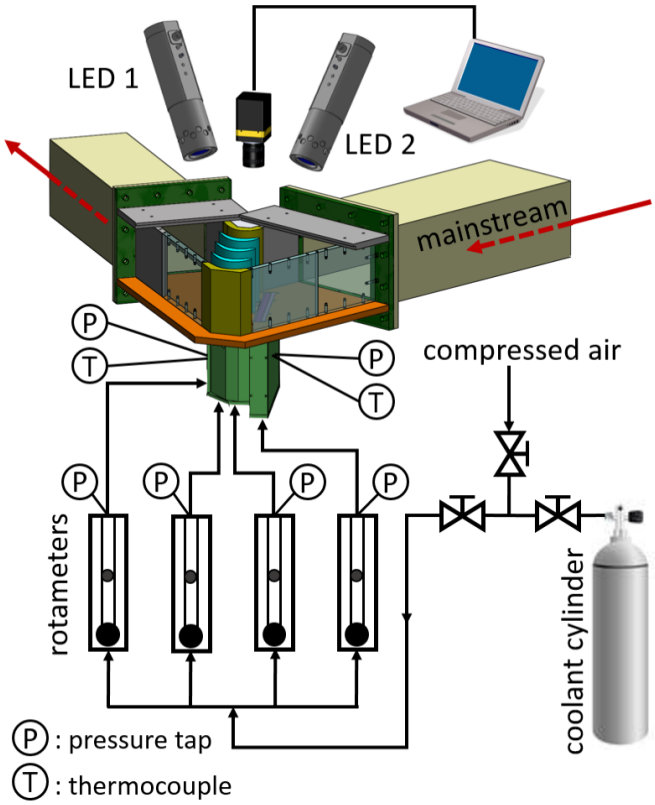

Figure 2 Schematic of the platform film cooling test facility. (Reprinted from Chen et al. [2])

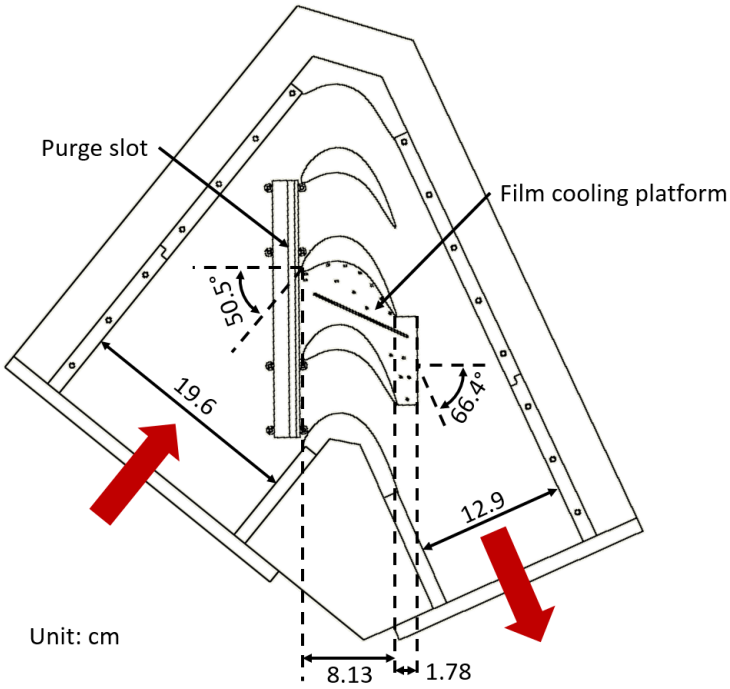

Figure 3 Top view of the five-blade linear cascade. (Reprinted from Chen et al. [2])

2.3.2 Simulated Purge Flow Design

In the current study, a generic single-tooth seal was used to simulate the stator-rotor gap as shown in Figure 4. It is composed of a pair of upstream tooth and downstream tooth. The seal was built by stereolithography (SLA) process with DSM Somos NanoTool resin. The inclination angle of the slot to the platform surface is 25°. The slot opening at the neck of the seal is 0.20 cm. The distance from the slot downstream edge to the blade leading edge is 0.59 cm. The slot covers more than 2.5 passages of the cascade. An injection plate was attached underneath the seal. There are two different designs of the injection plate. The baseline design comes with radial outward injection (no swirl effect). A row of 30 equally-spaced injection holes is at 90° to the surface. The diameter of the holes is 0.33 cm and the plate thickness is 1.27 cm. The second design has a row of 30 equally-spaced injection holes at a 45° angle to the surface toward the blade suction side. The diameter of the holes is 0.28 cm. The cross-sectional view of the second design is shown in Figure 4. The inclined holes were used to simulate the swirl effect at a typical swirl ratio (SR) of 0.6. A swirl ratio of 0.6 was defined such that the purge coolant moves in the same direction of the blades and has a circumferential velocity that equals 60% of the blade tangential velocity. That means the coolant to blade relative velocity (in the circumferential direction) is 40% of the blade tangential velocity. In the current study, analogy has been made between a real engine and a stationary cascade. The circumferential velocity of the ejected coolant at SR = 0.6 was about 60% of the mainstream inlet velocity. From the same definition, the baseline non-swirl design has a swirl ratio of 1 (SR = 1). A plenum was attached to the bottom of the injection plate for coolant supply.

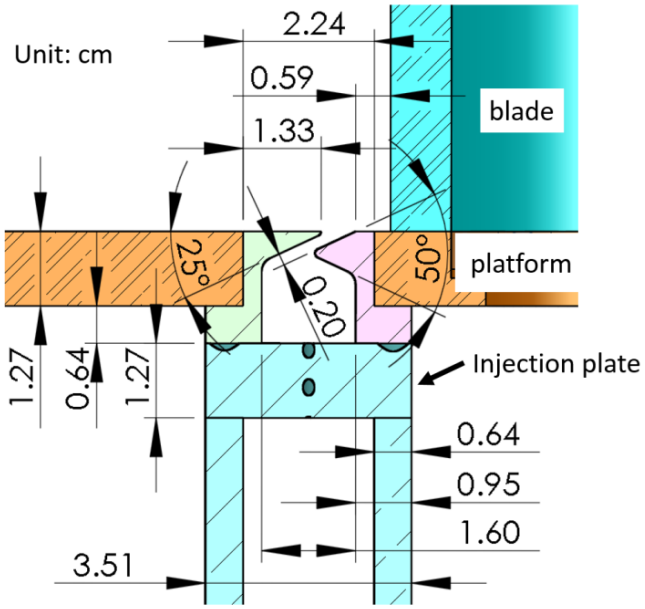

Figure 4 Sectional view of the geometry of the inlet purge seal, (swirl) injection plate, and part of the plenum. (Reprinted from Chen et al. [2])

2.3.3 Platform Film Cooling Design

Extra cooling was offered on the newly designed platform by 16 discrete film cooling holes and a slashface, as shown in Figure 5 and Figure 6. The 0.635 cm thick platform was fabricated by the same SLA process and the same resin as the seal. The layer thickness of the SLA process was 50 μm (~0.002 in). The parts have been sanded and finely blasted for a smoother surface. The slashface has a 65° angle to the front of the platform. The slashface gap is 8.91 cm in length, 0.16 cm in width, and 0.43 cm in depth. A row of thirty 0.08 cm diameter normal injection holes are equally distributed at the bottom of the slashface gap to simulate the leakage flow. These tiny holes in the slashface have an L/D ratio of (0.635-0.43)/0.08 = 2.56 and a hole spacing of 8.91 cm/30 ≈ 0.3 cm. Underneath the slashface, a plenum with a slightly larger cross-section is attached. The dimensions of

the plenum are about 9.5 cm (L) * 0.635 cm (W) * 15 cm (H). The slashface has a distance from the upstream edge (~1.35 cm) and downstream edge (0.84 cm) of the endwall, which is an inherent limitation arose from the design of the plenums.

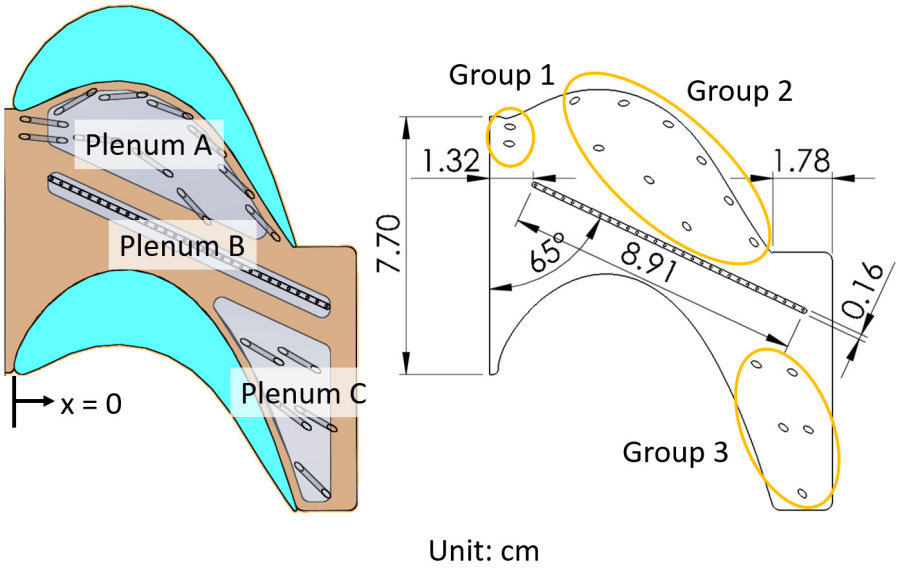

Figure 5 Design of the platform film-cooling and plenum cavities (cylindrical hole). (Reprinted from Chen et al. [2])

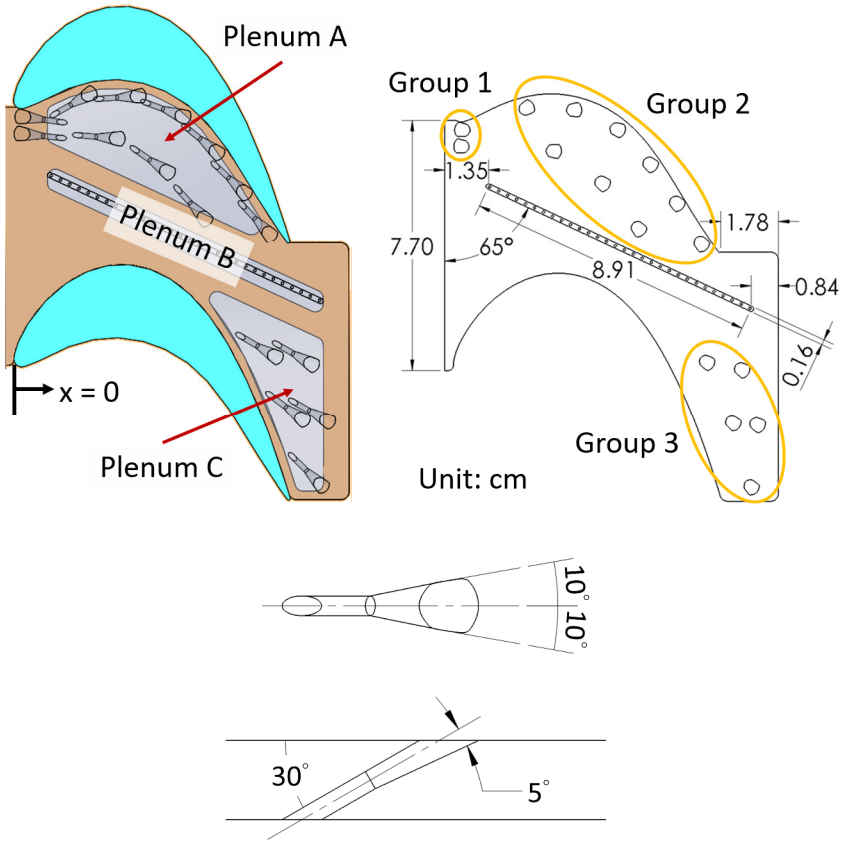

Figure 6 Design of the platform film-cooling, plenum cavities, and fan-shaped hole. (Reprinted from Chen et al. [3])

There are three groups of cooling holes on the endwall. Each cooling hole has a diameter of 1.588 mm, an L/D ratio of 8, and are inclined at 30° to the platform surface. For shaped hole design, laidback fan-shaped holes are characterized with a lateral expansion of 10° on both sides and a forward expansion of 5° from the hole axis. The hole expands at L/D = 4. The resultant exit to inlet cross-sectional area ratio is 2.8. Group 1 includes two backward injection holes in an attempt to reduce the strength of the horseshoe vortex and to cover the pressure side leading edge area. A complete study of backward

injection film cooling on a flat plate can be found in Refs. [6, 7]. Group 2 contains nine forward injection holes located in between the pressure side edge and the slashface. One row of holes is adjacent to the pressure side edge and is offset from the pressure side edge by about 0.25 cm. These holes have a compound angle of 30° toward pressure side and a P/D ratio of 9.1. The other row is offset from the pressure side edge by about 1.7 cm. These holes have a compound angle of 5° toward the suction side and a P/D ratio of 11.2. Group 3 has five holes located in between the downstream suction side edge and the slashface. The two rows of holes are offset from the suction side edge by about 0.9 cm and 1.7 cm and the P/D ratios are 12.8 and 11.2, respectively. Group 3 holes have a compound angle of 30° toward pressure side. The area between the slashface and the upstream suction side portion was left without film cooling holes since the inlet purge flow is expected to cover this area. The axial coordinate x = 0 is located at the leading edge of the blade.

It is difficult to control local blowing ratios of each cooling hole due to considerable pressure variations on the platform. Three plenums were used to individually control coolant supply, as shown in Figure 5 and Figure 6. Group 1 and group 2 holes located at high pressure area are fed by plenum A. Plenum B is used to feed the slashface gap. Group 3 holes at the low pressure area are fed by plenum C. It should be noted that the inlet purge slot has a separate plenum and all plenums are installed with flow conditioning elements such as wire meshes and honeycombs.

2.4 Experimental Method and Data Reduction

Film cooling effectiveness distributions were measured using pressure sensitive paint (PSP) technique through a mass analogy method. PSP is composed of fluorescent molecules and an oxygen-permeable polymer binder. As shown in Figure 7, a 400 nm LED lamp (Innovative Scientific Solutions, Inc., LM2X-DM-400) was used to excite the fluorescent molecules embedded in the polymer binder. The excited fluorescent molecules will emit fluorescent light at a wavelength around 650 nm as it relax from the excited state to the ground state. The emission intensity will be recorded by a scientific grade CCD camera (Innovative Scientific Solutions Inc., PSP-CCD-M) with a long pass filter (600 nm). When the paint is exposed to oxygen (O_2), the fluorescent molecules will go through another emission-free path to the ground state. Consequently, the surface emission intensity will be diminished. This phenomenon is known as the oxygen-quenching effect.

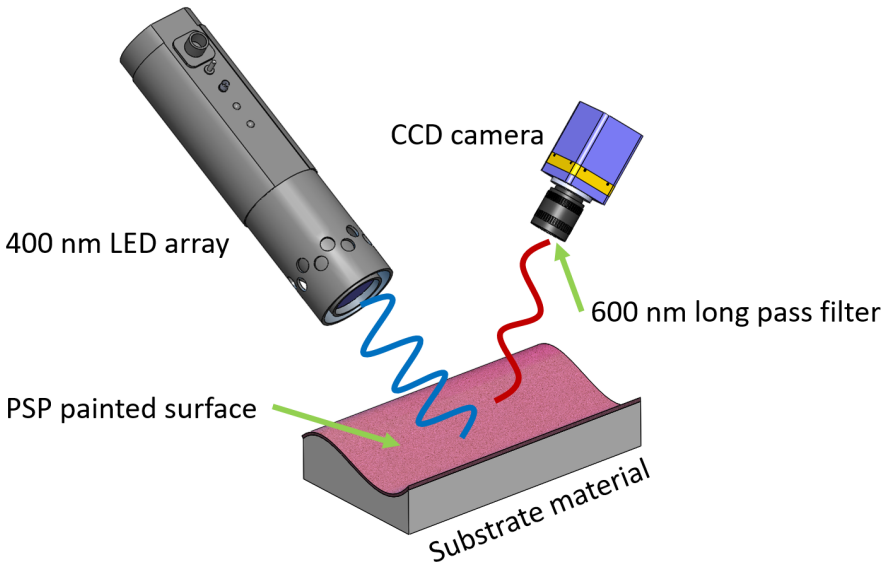

Figure 7 Schematic diagram of PSP measurement. (Reprinted from Chen et al. [2])

The endwall test plate used in the experiments (shown in Figure 5 and Figure 6) was carefully painted with PSP (Innovative Scientific Solutions Inc., UF-750). In order to find out the relationship between the PSP emission intensity and the oxygen partial pressure (or air pressure since there is a constant concentration of oxygen in the ambient air) on the painted surface, an airtight calibration chamber was used. A vacuum pump and a compressed air source were connected to the chamber to control the pressure inside the chamber. The LED lamp and CCD camera were positioned at the same distance and angle to the test plate as they were in the test section. The emission intensity (I) of the PSP was recorded at pressures (P) from 0 inHg (gauge pressure, which is equivalent to 1 atm, 1atm = 29.92 inHg) to -26 inHg (gauge pressure) at a 2 inHg interval and from 2 psig to 8 psig at a 2 psi interval. The pressure and emission intensity acquired under ambient pressure were used as references and were denoted as P_{ref} and I_{ref}, respectively. Background noise of the camera (I_{blk}) was recorded when there is no excitation light, and it will be subtracted from I and I_{ref}. A hundred gray-scale images were recorded for each case and were saved in TIF format. The emission intensity of each case was calculated by averaging those 100 images so as to cancel out the noise. The resulting calibration curve is shown in Figure 8 and a power fitting curve was used to fit the data points. The partial pressure of oxygen (or air) in close proximity to the painted surface can then be deduced from the surface emission intensity through the calibration curve.

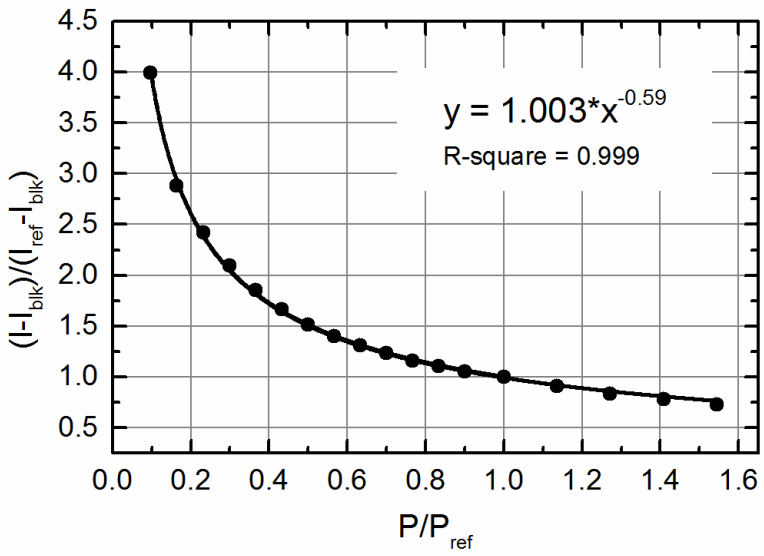

Figure 8 PSP calibration curve. (Reprinted from Chen et al. [2])

Four sets of data are required to determine film cooling effectiveness under each test condition. Those data include: (1) background intensity taken under no light condition (I_{blk}). (2) reference intensity (I_{ref}) taken with LED illumination and no flow. (3) air injection intensity (I_{air}) acquired with mainstream flow and LED light illumination while compressed air was injected as coolant. The corresponding oxygen concentration and partial pressure are $C_{O2,air}$ and $P_{O2,air}$. (4) foreign gas injection intensity (I_{fg}) measured with mainstream flow and LED light illumination. A foreign gas was injected as coolant. The corresponding oxygen concentration and partial pressure are $C_{O2,fg}$ and $P_{O2,fg}$.

When the molecular weight of the foreign gas is close to that of air (e.g. nitrogen), the adiabatic film cooling effectiveness can be calculated by Eq. (1):

$$\eta = \frac{T_{aw} - T_\infty}{T_c - T_\infty} \approx \frac{C_{O_2,wall} - C_{O_2,\infty}}{C_{O_2,c} - C_{O_2,\infty}} \approx 1 - \frac{C_{O_2,fg}}{C_{O_2,air}}$$
$$= 1 - \frac{P_{O_2,fg}}{P_{O_2,air}} = 1 - \frac{P_{O_2,fg}/P_{O_2,ref}}{P_{O_2,air}/P_{O_2,ref}} \quad (1)$$

When the molecular weight of the foreign gas is different from that of air, the equation needs to be modified in order to account for the variation of the effective molecular weight of the mixed gas in the cooling film. Adiabatic film cooling effectiveness can be calculated by Eq. (2):

$$\eta = 1 - \frac{1}{\left[1 + \left(\frac{P_{O_2,air}/P_{O_2,ref}}{P_{O_2,fg}/P_{O_2,ref}} - 1\right)\frac{W_{fg}}{W_{air}}\right]} \quad (2)$$

where W_{air} is the molecular weight of ambient air and W_{fg} is the molecular weight of the foreign gas coolant. There is a known temperature effect of the PSP (about 1% decrease in intensity per 1 °C temperature increment). According to Shiau et al. [44], the temperature effect of the PSP can be ruled out by taking all images (reference, air injection and coolant injection) under the same surface temperature. In another word, the calibration curve derived under room temperature can be used as long as all images are taken under the same local surface temperature. An in depth documentation respecting PSP measurement technique can be found in Han and Rallabandi [54].

2.5 Experimental Uncertainty

Part of the uncertainty of the experiment comes from the fluctuation of mainstream velocity (± 2%) and the fluctuation of coolant flow rate (± 3%). Fluctuation of the aforementioned quantities will reflect in variations in both distribution and value of the effectiveness. In terms of the calculation of the effectiveness, the primary uncertainty comes from the variation of the recorded PSP emission intensity, which can be affected by several factors such as the fluctuation of LED light intensity or surface temperature. 10 different sets of reference images were examined to evaluate the uncertainty. Use the method proposed by Kline and McClintock [55], based on a 95% confidence level, the uncertainties of film cooling effectiveness deduced from the calibration curve at $\eta = 0.1$, 0.3, 0.5 and 0.7 are 15%, 3.9%, 1.7% and 0.7%, respectively. Besides, surface aerodynamic heating might affect the film cooling effectiveness results since the PSP emission intensity is also a function of surface temperature. However, the calculated difference in adiabatic wall temperature from inlet to exit was less than 1 °C. Furthermore, as mentioned in the experimental method, the effect of temperature variation will be automatically canceled out when all images are acquired at the same local surface temperature. Therefore, the surface aerodynamic heating effect is considered negligible.

2.6 Test Matrix

The definition of blowing ratio is given in the nomenclature. However, as discussed earlier, it is difficult to control the blowing rate through each cooling hole in the cascade. As a result, an average blowing ratio (M) is defined in Eq. (3):

$$\dot{m}_{c,i} = M \times (\rho_\infty v_\infty)_i \times A_{c,i} \tag{3}$$

where $\dot{m}$ is the coolant mass flow rate of each plenum at a given average blowing ratio M; i refers to plenums A, B or C; $\rho_\infty v_\infty$ is the average mainstream mass flux above each plenum, and A_c is the overall cross-sectional area of cooling holes fed by the plenum. The average mainstream mass flux $\rho_\infty v_\infty$ is determined from the average local static pressure information obtained from the PSP measurement, as shown in paragraph 2.7.1. For simplicity, the term "blowing ratio" will be used instead of "average blowing ratio" in the following discussions.

At SR = 1, the platform film cooling blowing ratio effects were studied at three different blowing ratios M = 0.5, 1, and 1.5. The effects of inlet purge flow coolant-to-mainstream mass flow ratio (MFR) were studied at MFR = 0.5%, 0.75% and 1%. The MFRs were calculated based on the coolant mass flow rate and mainstream mass flow rate per passage. The effects of coolant-to-mainstream density ratio (DR) were tested at DR = 1, 1.5, and 2. The coolant-to-mainstream density ratios 1, 1.5, and 2 were achieved by utilizing industrial grade N_2, industrial grade CO_2, and a mixture of SF_6 (15% by volume)

and Argon (85% by volume) as coolant, respectively. The inlet purge swirl ratio (SR) effects were examined among SR = 1 and SR = 0.6 particularly at DR = 1, MFR = 1% and M = 1. There are 16 test cases for each cooling hole design and are summarized in Table 2. The corresponding MFRs for plenums A, B, and C at each blowing ratio (M = 0.5, 1, or 1.5) are also provided in Table 3. As can be seen, the total coolant mass flow rate that was supplied to the platform has a linear relationship to the blowing ratio. The total platform MFR percentage can be easily calculated by multiplying blowing ratio by 0.74.

Table 2 Test matrix for platform film cooling study

Hole Geometry	SR	DR	MFR (%)	M
Cylindrical and Fan-shaped Holes	1	1	0.5, 1	1
			0.75	0.5, 1, 1.5
		1.5	0.5, 1	1
			0.75	0.5, 1, 1.5
		2	0.5, 1	1
			0.75	0.5, 1, 1.5
	0.6	1	1	1

Table 3 Corresponding coolant supply MFR at different blowing ratios on the platform

Corresponding MFR (%)	M = 0.5	M = 1	M = 1.5
Plenum A	0.14	0.27	0.41
Plenum B	0.13	0.26	0.39
Plenum C	0.10	0.21	0.31
Total Platform	0.37	0.74	1.11

2.7 Results and Discussion – Cylindrical Holes

Experimental results of adiabatic film cooling effectiveness will be presented in the form of either contour plots or span-wise averaged line plots. The effects of inlet purge mass flow ratio, blowing ratio, density ratio, and swirl ratio will be discussed.

2.7.1 Surface Static Pressure Distribution

The static pressure distribution was measured by pressure sensitive paint with the test (endwall) plate installed under a fixed mainstream condition, as shown in Figure 9. As can be seen from the contour, there is a high pressure zone near the pressure side of blade. The pressure gradually decreases toward the suction side. This pressure difference is the main driving force of the strong cross flow inside the passage. It is also how the turbine can produce work. Non-uniform pressure distribution at the inlet affects the inlet purge flow significantly. Inlet purge flow will be suppressed by the high pressure near the pressure side. The static pressure decreases from upstream to downstream as the flow accelerates. There is a wedge shape low pressure zone right after the slashface near trailing edge. It can be attributed to flow trapping and recirculation after passing through the slashface gap.

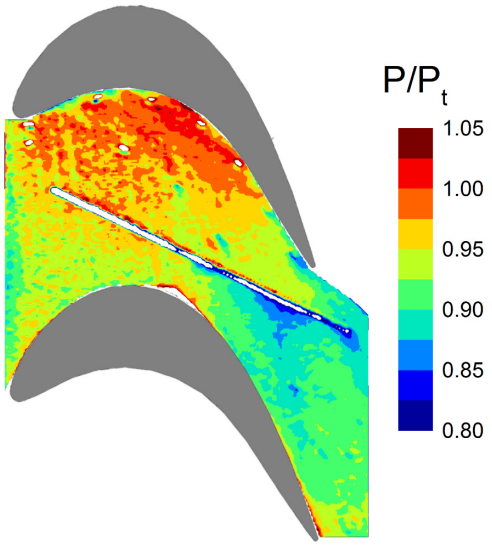

Figure 9 Static pressure distributions without coolant injection for cylindrical hole design (P_t is inlet total pressure). (Reprinted from Chen et al. [2])

2.7.2 General Observation

From the pressure distribution discussed above, it can be expected that the inlet purge flow will be more concentrated near the suction side. Film cooling traces, including slashface leakage and discrete-hole discharges, are swiped toward the suction side by strong cross flows in the passage. Film cooling is ineffective near the pressure side edge due to high local pressure and complex three-dimensional flow structures. Coolant ejection was suppressed at lower blowing ratios and higher density ratios. Coolant traces near the pressure side edge follow the edge curvature. Upstream-hole and gap interactions have been observed. Film cooling ejection from an upstream hole seemed to promote the effectiveness of the downstream gap leakage flow, which agreed with the results from [38]. Downstream cooling holes present much better protection due to low local static pressure

compared to the upstream pressure side holes. The upstream pressure side endwall remains a hard to cool region, where more advanced cooling schemes are needed.

2.7.3 Effect of Inlet Purge Mass Flow Ratio

The effects of inlet purge mass flow ratio were examined at three different density ratios and a platform average blowing ratio of 1. Detailed film cooling effectiveness contours are shown in Figure 10. At a low inlet purge MFR (MFR = 0.5%), the coolant only covers the leading edge portion near the suction side. This is caused by the non-uniform pressure distribution as stated earlier. The triangular shape of the inlet purge film coverage as seen in the contour is due to strong vortices. The horseshoe vortex and passage vortex separation line formed from the pressure side leading edge to the suction side trailing edge, which prevents the coolant from spreading across the line. There is a low effectiveness area at the suction side leading edge, which is caused by downwash suction side leg horseshoe vortex. By increasing the MFR, the coolant coverage and film effectiveness increase monotonically. At MFR = 1%, the purge flow is so strong that the film coverage expands to the pressure side leading edge. However, the coverage is still limited by the boundary layer separation line associated to the vortices.

From the span-wise averaged line plots (Figure 11), effectiveness is high at the inlet and then gradually decrease. Higher MFR results in higher effectiveness. The effectiveness values at different MFRs gradually merge together, and then coincide with each other after $x/C_{ax} \approx 0.5$.

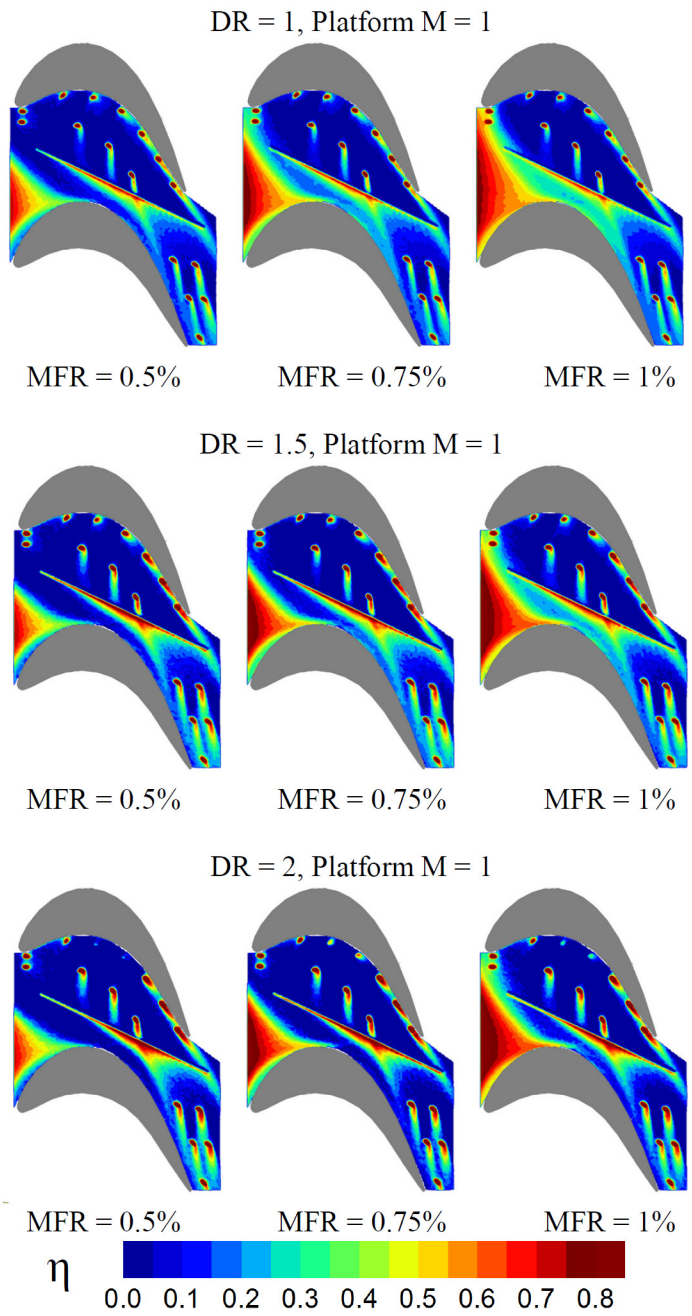

Figure 10 Film-cooling effectiveness contour showing inlet purge MFR effect at DR = 1, 1.5, and 2 (M = 1) for cylindrical hole design. (Reprinted from Chen et al. [2])

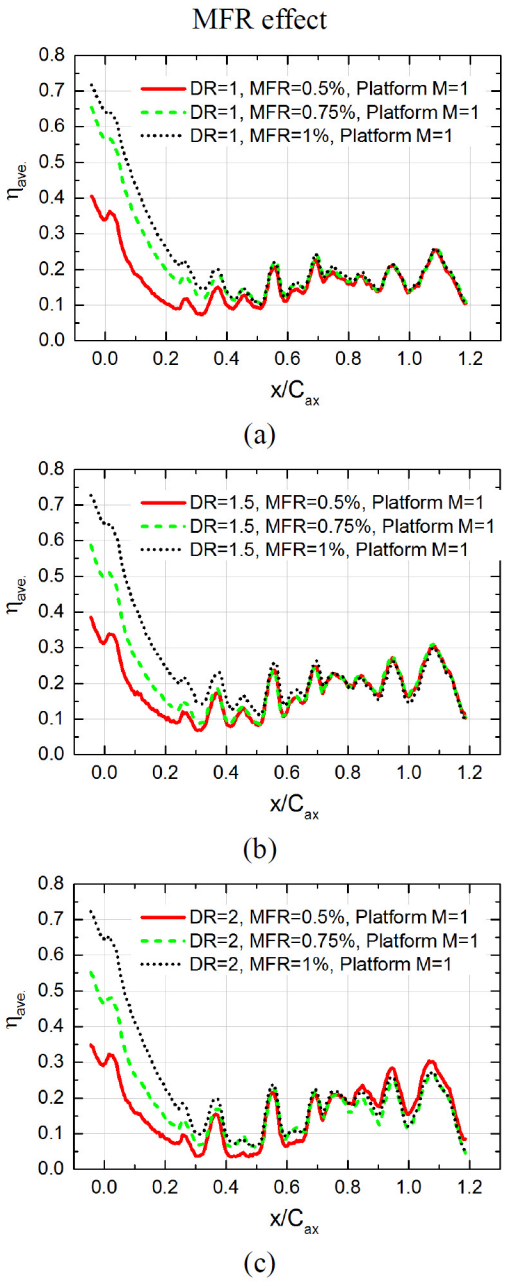

Figure 11 Spanwise-averaged film cooling effectiveness showing inlet purge MFR effect. (a) DR = 1, (b) DR = 1.5, and (c) DR = 2. Platform M = 1 for cylindrical hole design. (Reprinted from Chen et al. [2])

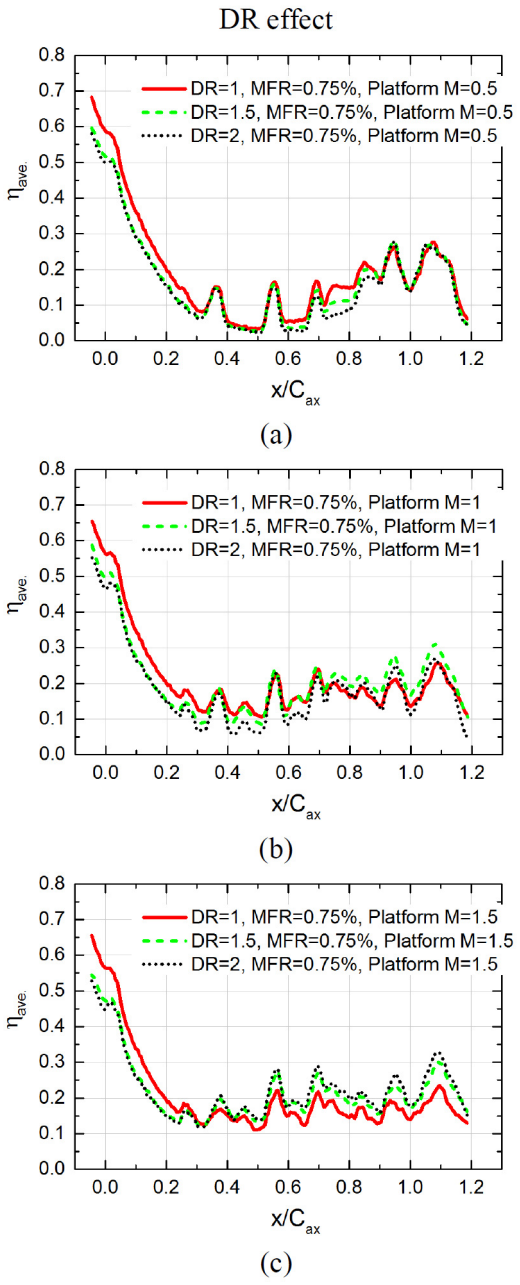

Figure 12 Spanwise-averaged film cooling effectiveness for DR = 1, 1.5, and 2 at (a) M = 0.5, (b) M = 1, and (c) M = 1.5. Inlet purge MFR = 0.75% for cylindrical hole design. (Reprinted from Chen et al. [2])

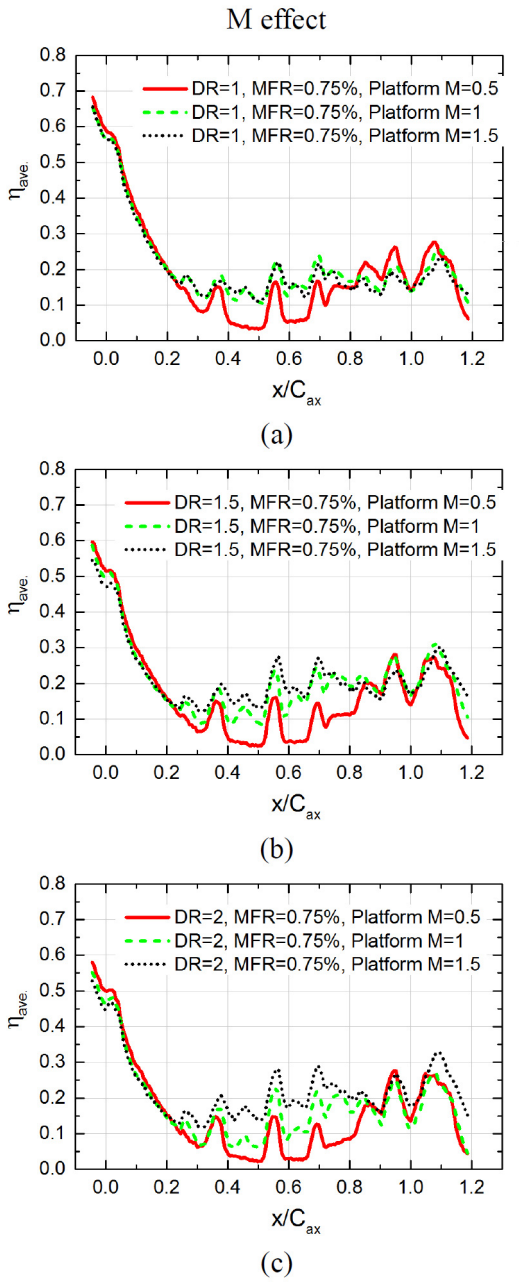

Figure 13 Spanwise-averaged film cooling effectiveness for M = 0.5, 1, 1.5 at (a) DR = 1, (b) DR = 1.5, and (c) DR = 2. Inlet purge MFR = 0.75% for cylindrical hole design. (Reprinted from Chen et al. [2])

2.7.4 Effect of Density Ratio

Span-wise averaged line plots for density ratio effect and blowing ratio effect are shown in Figure 12 and Figure 13. The effectiveness contour plots for three density ratios with a range of blowing ratios are presented in Figure 14. A nominal inlet purge MFR = 0.75% was chosen among all cases. For the inlet purge flow, coolant coverage seems to be slightly reduced with increasing density ratio. Although the coolant is heavier at higher density ratios, the coolant injection velocity (momentum) and coolant volume flow rate are lower under the same MFR.

For the film holes and slashface at low blowing ratio (i.e., M = 0.5), increase the density ratio may reduce the film coverage and effectiveness due to similar reasons for the inlet purge flow. At medium and high blowing ratios (i.e., M = 1 and 1.5), the film coverage becomes wider and longer with increasing density ratio. The reason is that at low density ratio and high blowing ratios, the coolant jet momentum is high, which allow the jet to penetrate into the mainstream. This jet penetration or lift-off effect significantly reduces the film-cooing effectiveness. When the density ratio increases, the jet momentum becomes lower so that it is more likely to attach to the surface.

From the line plots shown in Figure 10, it can be seen clearly that the inlet purge effectiveness ($x/C_{ax} < 0.3$) decreases at higher density ratios DR = 1.5 and 2. The span-wise averaged effectiveness for DR = 1.5 and 2 are almost identical. It can be a result of the counteracting effects where lower volume flow rate reduce the film coverage and the reduced momentum facilitate the coolant attachment. For the downstream side, increase density ratio results in a negative effect in effectiveness at a low blowing ratio of M = 0.5. On the contrary, at a high blowing ratio M = 1.5, higher density ratio leads to higher

effectiveness. The transition of density ratio effects on the platform at the downstream portion ($x/C_{ax} > 0.6$) can be seen clearly from low blowing ratio M = 0.5 to medium and high blowing ratios M = 1 and 1.5.

2.7.5 Effect of Blowing Ratio

The contour plots in Figure 14 also show the blowing ratio effects for three different density ratios at a fixed inlet purge MFR of 0.75%. The most interesting thing is that the slashface coolant traces extend upstream with increasing blowing ratio. At the meantime, the coolant jets coming out from the slash face have a higher tendency to penetrate into the mainstream at higher blowing ratios, which results in a lower effectiveness. The results indicate that a carefully designed blowing condition for the slash face has a great impact on the platform film cooling. Both the film coverage and effectiveness change dramatically with blowing ratio. At M = 0.5, a wedge shape trace can be seen at the downstream. This is a typical result for a vane passage, where there is a stronger pressure variation from leading to trailing edge for flow acceleration. For a blade passage, the main objective is to create power, hence the pressure gradient from pressure side to suction side is stronger than that in the vane passage. As the blowing ratio increase, the increased pressure in the slashface plenum allow coolants to overcome the pressure on the blade endwall surface. At DR = 1 and M = 1 and 1.5, the slashface coolant almost merge with the inlet purge coolant and provide exceptional protection between the slashface and blade suction side surface.

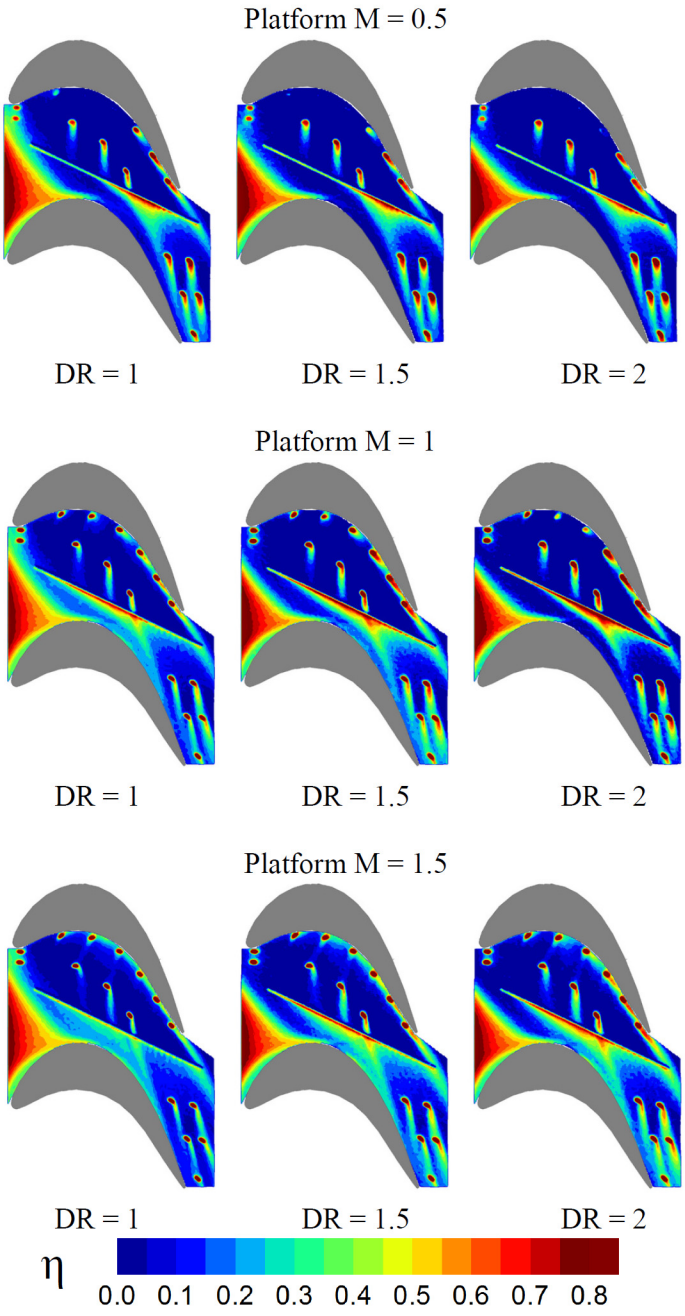

Figure 14 Film cooling effectiveness contours for density and blowing ratio effects under inlet purge MFR = 0.75% for cylindrical hole design. (Reprinted from Chen et al. [2])

Another interesting thing is that among all cases studied, the two backward injection holes at the leading edge always lit up, which implies that the coolant came out but detached from the surface. Only at M = 0.5, a scarce film from the two cooling holes can be seen in the very leading edge portion. The film covers the immediate surroundings of the holes and then gradually migrates toward the suction side. It eventually merges with the inlet purge film. The vigorous turbulent mixing of the coolant and the mainstream by the complex three-dimensional vortical structures at the blade leading edge significantly reduced the effectiveness. Nevertheless, the results indicate a possible way to cool the leading edge region with backward injection holes. At M = 1 and 1.5, it is likely that the coolant jets directly shoot into the mainstream, leaving no traces around the holes.

For pressure side holes, coolants cannot eject from some of the film cooling holes due to low momentum and low plenum pressure relative to the endwall surface pressure, especially at a low blowing ratio (M = 0.5). At M = 0.5, the first few holes near the pressure side edge did not light up, which implies no coolant ejection and possible mainstream ingression. As discussed earlier, coolant jets have a lower momentum at a higher density ratio. This can explain why there were more pressure side edge holes lit up near the trailing edge at M = 0.5 and DR = 1 (three holes) than at M = 0.5 and DR = 2 (two holes). For other film holes, generally, coolant traces become longer and narrower with increasing blowing ratio. Lift-off effect of coolant jets can be seen from M = 0.5 to M = 1.5, especially at DR = 1.

The span-wise averaged effectiveness comparisons for blowing ratio effects are presented in Figure 13. The benefit of increasing the blowing ratio becomes more pronounced at DR = 2 than at DR = 1 in the mid-passage portion (x/C_{ax} = 0.2 to x/C_{ax} =

0.8). It is due to the aforementioned mechanism: higher density ratio coolant has a reduced tendency to lift off. For the downstream part ($x/C_{ax} > 0.8$), effectiveness is higher at M = 0.5 and DR = 1. For DR = 1.5 and 2, there are only small differences in effectiveness among three blowing ratios.

2.7.6 Effect of Inlet Purge Swirl Ratio

Effects of inlet purge swirl ratio were assessed at MFR = 1%, DR = 1 and platform film cooling M = 1. Two swirl ratios were examined: SR = 1 (non-swirled case) and SR = 0.6 (swirled case). Due to the circumferential velocity component of the coolant at SR = 0.6, the inlet purge flow possessed high momentum toward the blade suction side which led to lower effectiveness values and a reduced coverage. As shown in Figure 15 (a), the purge flow coolant trace for SR = 0.6 is more skewed than SR = 1. The area near the slashface before the throat is less covered by the purge flow. The effect of the suction side leg horseshoe vortex seems to be reduced by the swirled purge flow. At SR = 1, the effectiveness at the edge of suction side endwall is around $\eta = 0.5$ (yellow). At SR = 0.6, the purge coolant reaches the blade suction side surface and the effectiveness on the endwall increases to about $\eta = 0.6$~0.65 (orange).

From the span-wise averaged data shown in Figure 15 (b), the inlet purge swirl ratio has no effect on the downstream ($x/C_{ax} > 0.4$) portion. For $0 < x/C_{ax} < 0.3$, the span-wise averaged effectiveness drops apparently at SR = 0.6.

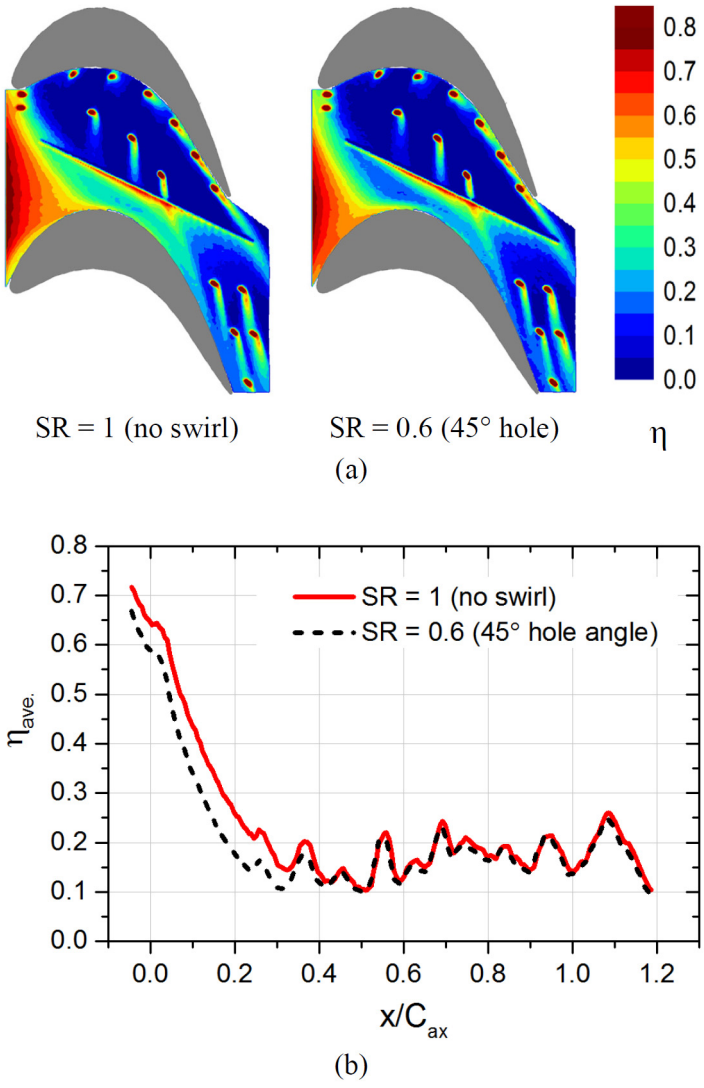

Figure 15 Inlet purge swirl ratio effects on the platform film cooling for cylindrical hole design: (a) contour plot and (b) spanwise-averaged plot. (Reprinted from Chen et al. [2])

2.7.7 Conclusions – Cylindrical Holes

Detailed static pressure and film cooling effectiveness measurements are presented for a turbine blade endwall with upstream (swirl) purge slot, slashface gap, and discrete film cooling holes using pressure sensitive paint (PSP) measurement technique. Parametric effects were studied on coolant-to-mainstream density ratio (up to close engine condition DR = 2.0), inlet purge mass flow ratio (0.5% - 1%) and platform film cooling blowing ratio (0.5 – 1.5). Inlet purge swirl effects were also studied at SR = 0.6. High resolution effectiveness contours reveal important findings in backward injection near the blade leading edge, upstream hole-gap interactions, swirl purge flow as well as the slashface leakage flow. The main conclusions are drawn as follows:

Inlet Purge MFR Effect

The inlet purge MFR has a significant impact on the platform film-cooing near leading edge $x/C_{ax} < 0.5$. It provides superior film coverage on the endwall. Both the film coverage and span-wise averaged effectiveness were greatly improved with increasing MFR.

Density Ratio Effect

The span-wise averaged effectiveness at inlet ($x/C_{ax} < 0.3$) decreases at higher density ratios (DR = 1.5 and 2) due to a reduced coolant coverage of purge flow. For the downstream portion ($x/C_{ax} > 0.6$), increasing density ratio has a negative effect on effectiveness at a low blowing ratio M = 0.5, whereas it has a positive effect at a high blowing ratio M = 1.5.

Blowing Ratio Effect on Slashface Film Cooling

Distribution of the coolant ejected from the slashface is highly dependent on the blowing ratio. At M = 0.5, coolant only covers the downstream portion. The slashface leakage flow

coverage extends toward upstream with increasing blowing ratio, however, the effectiveness may be lower due to turbulent mixing with mainstream. Upstream-hole and gap interactions can be seen at M = 1 and 1.5, where film coverage of slashface leakage flow is enhanced with the presence of a nearby upstream hole.

Blowing Ratio Effect on Endwall Film Cooling Holes

Low density coolant has a higher tendency to lift off from the surface, and vice versa. This is valid for both the slashface leakage flow and film cooling holes. Generally, effectiveness reduces as coolant lifts off and penetrate into the mainstream (at higher blowing ratios and lower density ratios). Scarce film was seen near the backward injection holes at M = 0.5. Film cooling holes at pressure side edge were inactive at a low blowing ratio M = 0.5, yet, better coverage was achieved at M = 1.5. Film cooling protection near the pressure side remains a challenge.

Inlet Purge Swirl Ratio Effect

The increased relative motion towards the blade suction side resulted in a more skewed wedge shape coverage and a lower span-wise averaged effectiveness. Some of the high momentum coolant impinges on the blade suction surface, brings about an elevated effectiveness near the suction side edge. The influence of the suction side leg horseshoe vortex is reduced. It has no effect at downstream after $x/C_{ax} > 0.4$.

2.8 Results and Discussion – Fan-Shaped Holes

Experimental results of adiabatic film cooling effectiveness will be presented in the form of contour plots, laterally averaged line plots, or area averaged plots. The effects of inlet purge mass flow ratio, swirl ratio, platform blowing ratio and density ratio will be discussed.

2.8.1 Surface Static Pressure Distribution

The static pressure distribution was measured by pressure sensitive paint with the test (endwall) plate installed under a fixed mainstream condition, as shown in Figure 16. A high-pressure zone can be identified near the pressure side of the blade. The pressure gradually decreases toward the suction side. This pressure gradient is the main driving force of the strong cross flow inside the passage. It is also how work is produced by rotating blades. The static pressure also decreases from upstream to downstream as the flow accelerates. This two-dimensional surface pressure distribution greatly affects the trajectories of coolant traces. There is a wedge shape low-pressure zone right after the slashface near trailing edge. It can be attributed to flow trapping and recirculation after passing through the slashface gap.

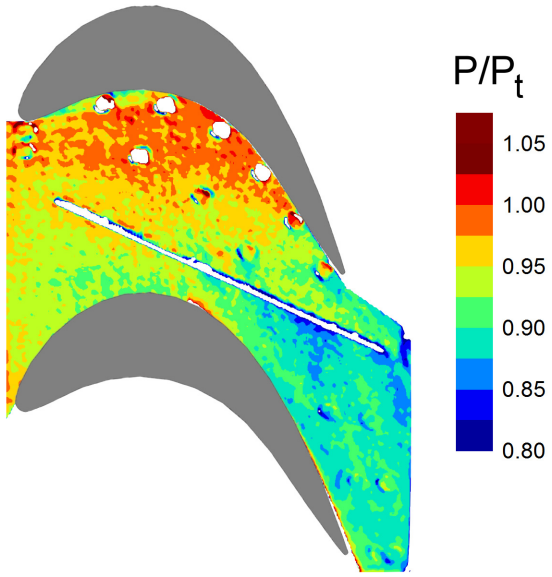

Figure 16 Static pressure distributions without coolant injection for shaped hole design (P_t is inlet total pressure). (Reprinted from Chen et al. [3])

2.8.2 General Observation

The inlet purge flow is more concentrated near the suction side due to a higher static pressure near the pressure side endwall. There is only scarce film coverage near the mid-chord pressure side edge as the coolant can hardly overcome the high static pressure. Contrarily, for the downstream portion, discrete film cooling holes provide a much better film coverage. Film cooling traces on the endwall are being swiped from the pressure side toward the suction side by the strong cross flow. Coolant ejection from the slashface gap forms a triangular shape trace that covers the downstream area between the gap and the suction side edge at M = 0.5. The trace extends upstream as blowing ratio increases. The upstream pressure side endwall remains a hard to cool region and the results suggest that more cooling holes may be used to improve film coverage.

2.8.3 Effect of Inlet Purge Mass Flow Ratio

The effect of inlet purge mass flow ratio was investigated at three different density ratios and a platform average blowing ratio of 1. Detailed film cooling effectiveness contours are shown in Figure 17. At a low inlet purge MFR (MFR = 0.5%), the coolant only covers the upstream portion near the suction side. This is a result of the non-uniform static pressure distribution as stated earlier. At higher MFRs, the coolant coverage gradually extends toward the pressure side. However, it is still limited by the strong secondary flows in the passage. Horseshoe vortex and passage vortex form a boundary layer separation line from the pressure side leading edge to the mid-chord of the suction side. This vortical structure prevents the purge flow coolant from migrating across the line. There is also a low effective area near the suction side leading edge that is associated with the downwash of the suction side leg horseshoe vortex.

Laterally averaged effectiveness values are shown in Figure 18. It can be seen that increasing MFR has a strong positive effect on the effectiveness. The effectiveness is high at the cascade inlet and then gradually decrease downstream. At a fixed density ratio, the effectiveness curves at three different MFRs gradually merge together along x/C_{ax}. The inlet purge MFR effect diminishes at $x/C_{ax} \approx 0.5$.

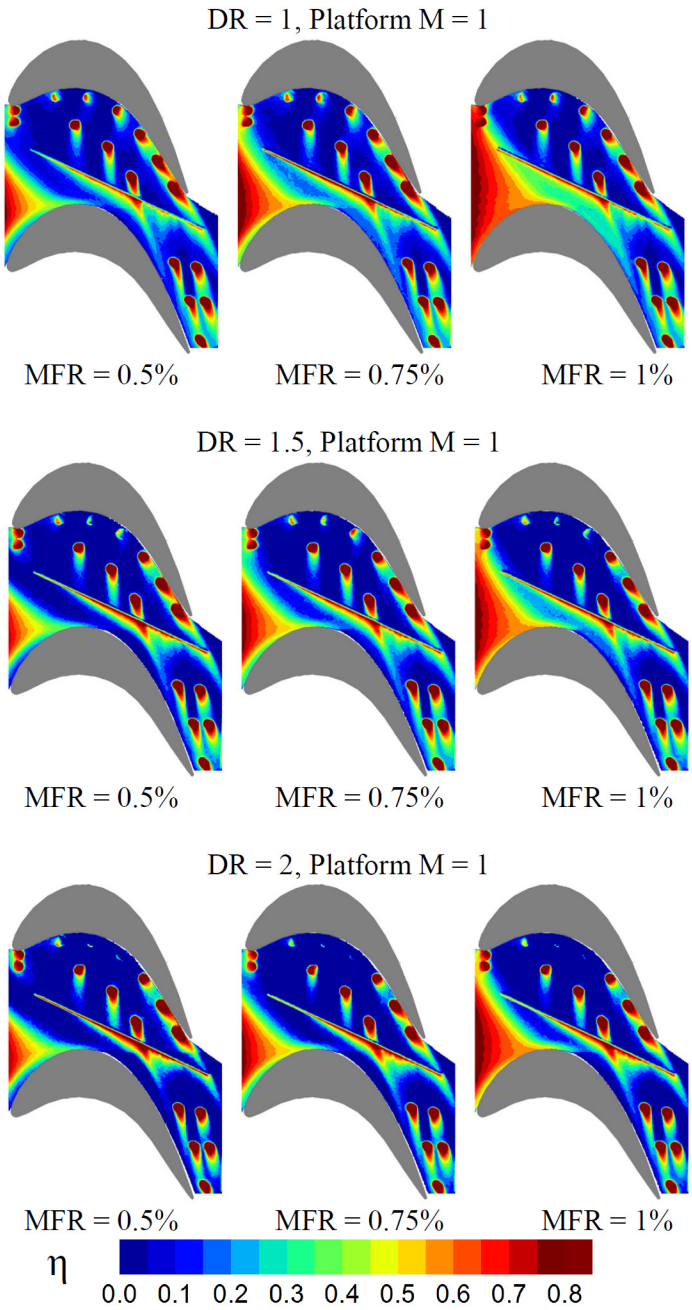

Figure 17 Film-cooling effectiveness contours showing inlet purge MFR effect at DR = 1, 1.5, and 2. Platform M = 1 for shaped hole design. (Reprinted from Chen et al. [3])

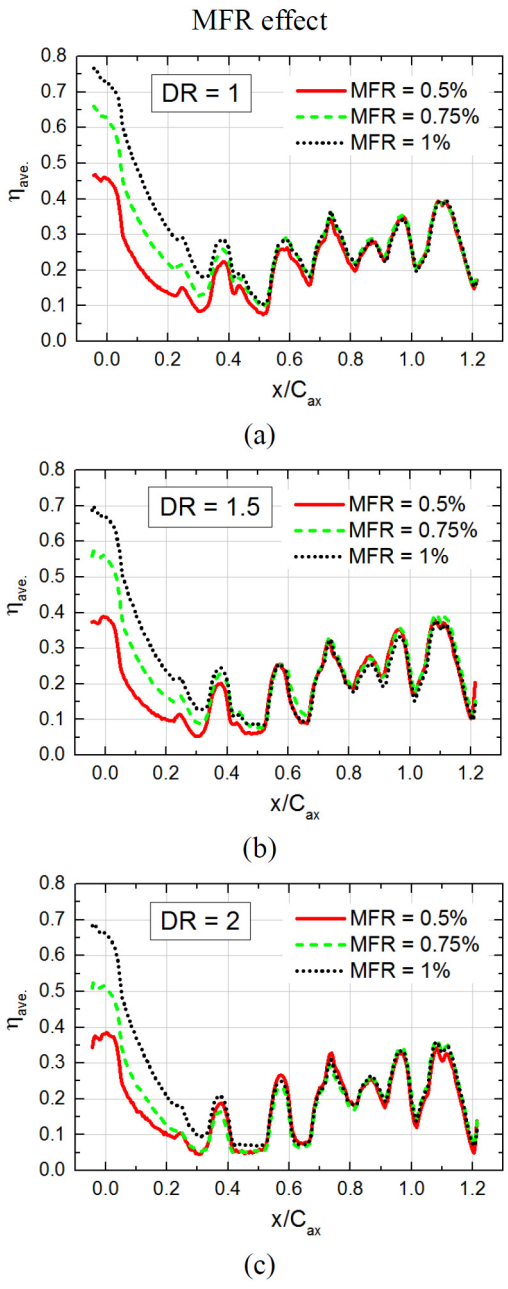

Figure 18 Laterally averaged film cooling effectiveness showing inlet purge MFR effect: (a) DR = 1, (b) DR = 1.5, and (c) DR = 2. Platform M = 1 for shaped hole design. (Reprinted from Chen et al. [3])

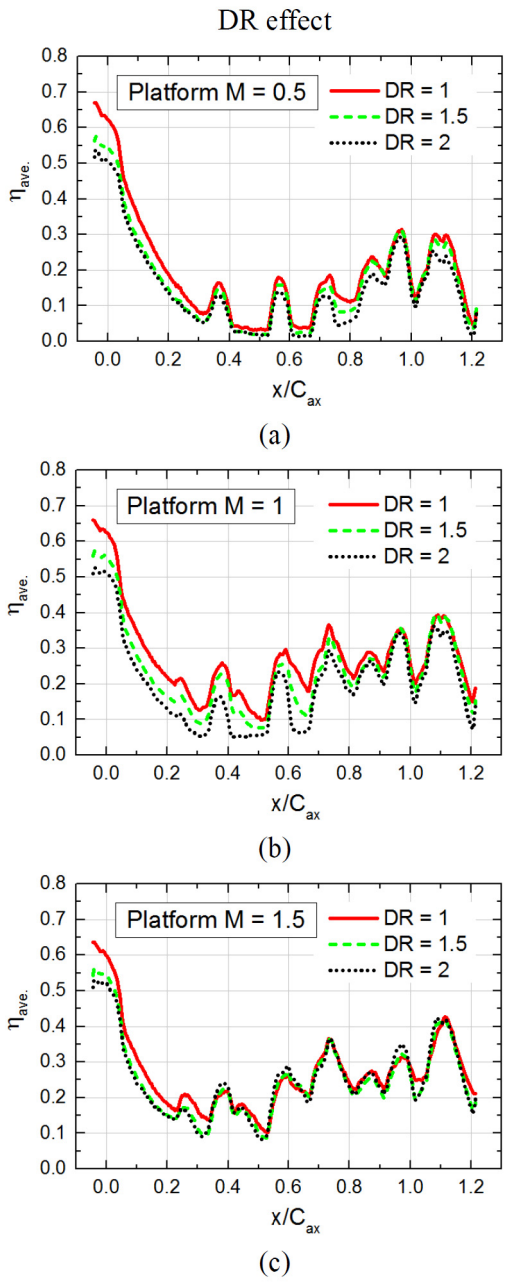

Figure 19 Laterally averaged film-cooling effectiveness for DR = 1, 1.5 and 2 at (a) M = 0.5, (b) M = 1, and (c) M = 1.5. Inlet purge MFR = 0.75% for shaped hole design. (Reprinted from Chen et al. [3])

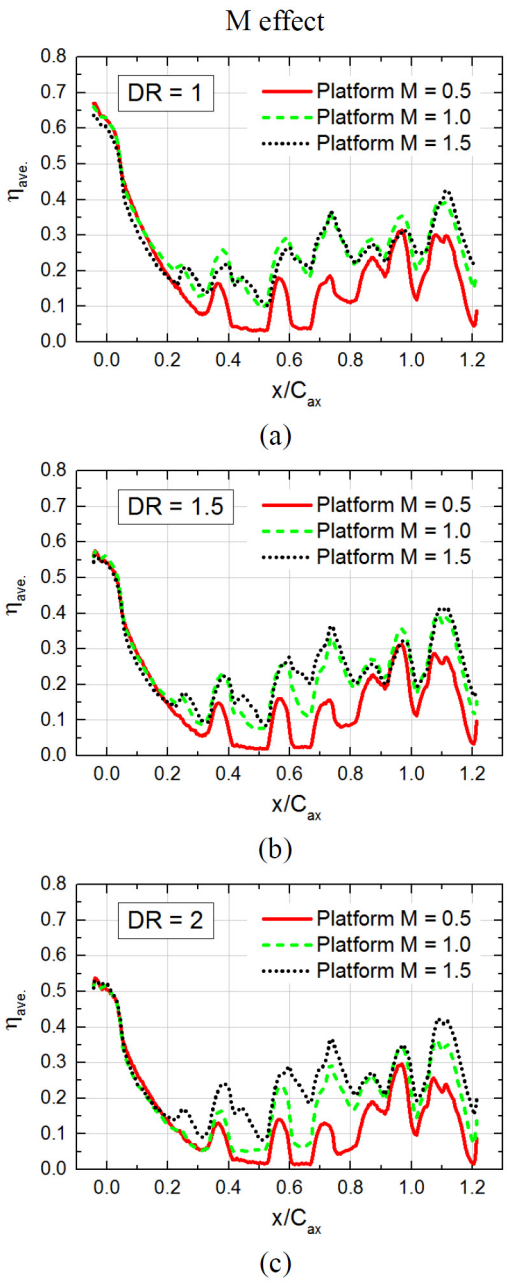

Figure 20 Laterally averaged film-cooling effectiveness for M = 0.5, 1, 1.5 at (a) DR = 1, (b) DR = 1.5, and (c) DR = 2. Inlet purge MFR = 0.75% for shaped hole design. (Reprinted from Chen et al. [3])

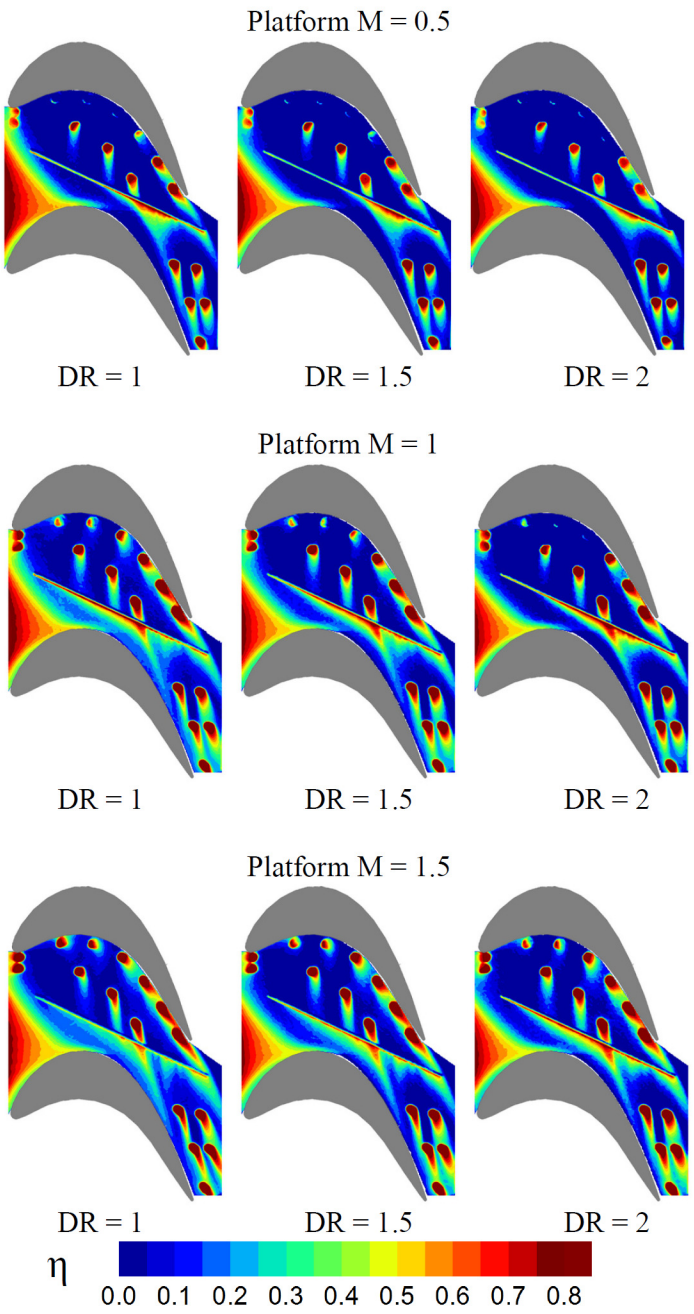

Figure 21 Film-cooling effectiveness contours for density and blowing ratio effects under inlet purge MFR = 0.75% for shaped hole design. (Reprinted from Chen et al. [3])

2.8.4 Effect of Density Ratio

Figure 19 and Figure 20 show the laterally averaged effectiveness for the density ratio and blowing ratio effects, respectively. Figure 21 shows the effectiveness contour plots for three density ratios and three blowing ratios at a fixed inlet purge MFR of 0.75%. The purge flow film coverage reduces with increasing density ratio. This phenomenon can also be seen in Figure 17. It can be explained by the lower coolant momentum and volume flow rate at a higher density ratio for a fixed MFR.

For the film coverage provided by the fan-shaped holes, unlike the cylindrical holes, density ratio effect is not that prominent. There is almost no difference among low density ratio and high density ratio cases. It is because the shaped holes act like a diffuser that reduce the coolant momentum, which facilitates coolant attachment. In another word, the coolant momentum is already low even at a low density ratio. For the slashface gap leakage flow, the film coverage slightly increases with increasing density ratio at a high blowing ratio of M = 1.5. However, the effect is small at M = 0.5 and 1.

From the laterally averaged line plots in Figure 10, it can be seen clearly that the density ratio has a negative effect on the purge flow effectiveness ($x/C_{ax} < 0.3$). Yet, the difference is small between DR = 1.5 and 2. The reason is that the coolant possesses much higher momentum at DR = 1 than DR = 1.5 and 2, which could overcome high surface static pressures and extend coolant coverage. For the downstream portion ($x/C_{ax} > 0.3$), density ratio has a negative effect on film cooling effectiveness at low and medium blowing ratios (M = 0.5 and 1). At M = 1.5, density ratio has nearly no effect on the effectiveness and it is a combined result of a slightly reduced film coverage and a slightly increased local effectiveness as DR increases from 1 to 2.

2.8.5 Effect of Blowing Ratio

Blowing ratio plays an important role in platform film cooling as can be seen from the contour plots in Figure 21. For the slashface leakage flow, coolant accumulates near the downstream portion and forms a triangular shape film at a low blowing ratio of M = 0.5. As blowing ratio increases to M = 1 and 1.5, the coolant trance extends upstream and covers more area between the slashface and the suction side endwall. This is quite different from the typical results of a vane cascade, where coolant traces are confined in the downstream portion owing to a relatively high stream-wise pressure gradient. In a rotor blade passage, the lateral pressure gradient is greater than the stream-wise pressure gradient as shown in Figure 16. As blowing ratio increases, a higher pressure in the plenum allows coolant to overcome the pressure on the endwall surface. As a result, the coolant coverage spreads upstream. On the other hand, the effectiveness of the slashface leakage flow slightly decreases from M = 1 to M = 1.5. It can be explained by the fact that the coolant jets possess higher momentum at M = 1.5 and penetrate deeper into the mainstream.

For the two backward injection holes located at the pressure side leading edge endwall, coolant ejects from the holes under all test conditions. The coolant covers the diffuser shape area of the holes and then migrates toward suction side. Both effectiveness and film coverage increase with increasing blowing ratio. The coolant coverage expands upstream of the holes at higher blowing ratios. Despite the fact that upstream injection may lead to higher pressure loss, the results demonstrate an approach to cool the leading edge region adequately with backward injection shaped holes.

For film cooling holes near the pressure side edge, a high blowing ratio (M = 1.5) is needed to ensure coolant discharge. At low blowing ratios (M = 0.5 and 1), high static

pressure near the pressure side edge inhibits coolant discharge. Those cooling holes without coolant discharge have zero effectiveness (cannot be seen from the contours). It also implies possible mainstream ingression that is undesirable and can be dangerous for an operating engine. As discussed earlier, coolant jets have a lower momentum at a higher density ratio. This can explain why there are more pressure side edge holes lit up near the trailing edge at M = 0.5 and DR = 1 (three holes) than at M = 0.5 and DR = 2 (two holes). The same trend can be seen for M = 1 and 1.5. For other cooling holes, generally, coolant traces become wider and longer with increasing blowing ratio.

The laterally averaged effectiveness comparisons for blowing ratio effects are presented in Figure 20. The difference for the upstream portion ($x/C_{ax} < 0.2$) is negligible since the effectiveness variations of the backward injection holes are small. At DR = 1, there is small difference between M = 1 and 1.5. At DR = 1.5 and 2, higher blowing ratio results in higher effectiveness. A low blowing ratio of M = 0.5 always provides least coverage and effectiveness.

2.8.6 Effect of Inlet Purge Swirl Ratio

Purge flow swirl ratio (SR) effects were studied at a specific condition of MFR = 1%, DR = 1, and a platform blowing ratio of 1. Figure 22 (a) shows the effectiveness contours for SR = 1 (non-swirled case) and 0.6 (swirled case). At SR = 0.6, the coolant jets have a circumferential velocity component toward the blade suction side, which reduces the film coverage as well as the effectiveness. From the laterally averaged plot shown in Figure 22 (b), the purge flow swirl ratio does not affect the effectiveness downstream of $x/C_{ax} = 0.4$. For $x/C_{ax} < 0.4$, the effectiveness at SR = 0.6 is lower than that of SR = 1.

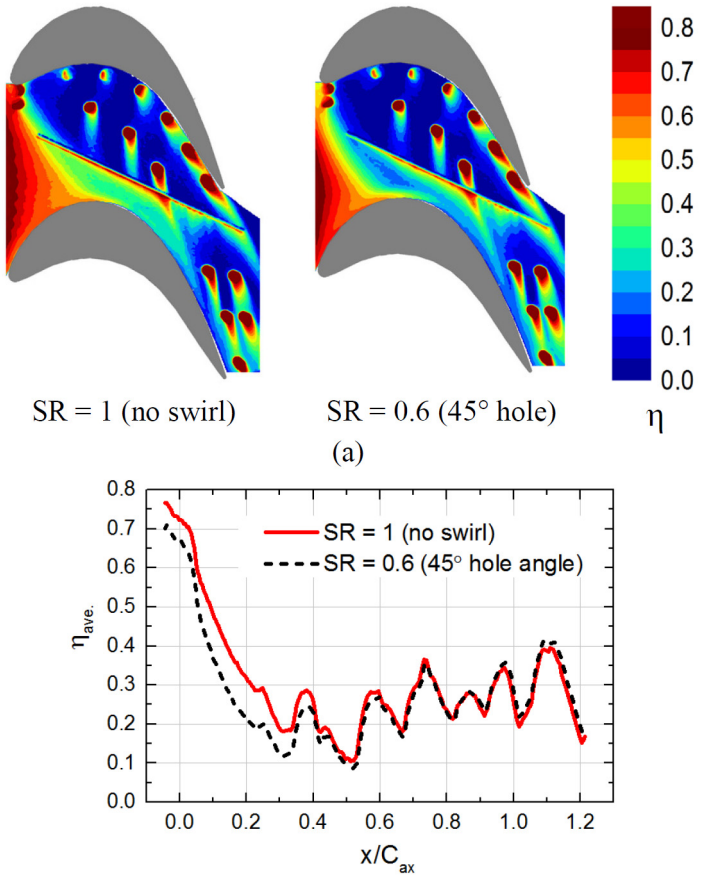

Figure 22 Inlet purge swirl ratio effects on the platform film cooling effectiveness at MFR = 1%, platform M = 1 and DR = 1 for shaped hole design: (a) contour plot and (b) laterally averaged plot. (Reprinted from Chen et al. [3])

2.8.7 Conclusions – Fan-Shaped Holes

Detailed film cooling effectiveness measurements are presented for a turbine blade platform with upstream (swirl) purge slot, slashface gap, and discrete fan-shaped holes using PSP measurement technique. Several important parameters were studied: purge flow MFR (0.5% - 1%), coolant-to-mainstream density ratio (up to engine like condition, DR = 2), platform film cooling blowing ratio (M = 0.5 - 1.5), and purge flow swirl effect. Some of the main conclusions are listed below:

(1) Purge flow provides superior film coverage particularly at the upstream suction side portion. Film coverage and laterally averaged effectiveness were greatly improved with increasing MFR. The MFR effect can be seen at $x/C_{ax} < 0.5$.

(2) Laterally averaged effectiveness at $x/C_{ax} < 0.3$ slightly reduces as DR increases. For $x/C_{ax} > 0.3$, similar effect can be seen at M = 0.5 and 1. It can be attributed to the reduced momentum and coolant volume flow rate at higher DRs. At M = 1.5, however, no significant difference in laterally averaged effectiveness at $x/C_{ax} > 0.3$.

(3) Coolant coverage of the slashface ejection is highly dependent on the blowing ratio. At M = 0.5, coolant accumulates near the downstream portion and forms a triangular trace. At higher blowing ratios, coolant trace extends further upstream, however, the effectiveness value may be lower as M increases from 1 to 1.5 due to stronger mixing with mainstream. An upstream hole nearby the slashface could promote downstream film cooling under some conditions.

(4) Generally, a higher blowing ratio leads to higher film cooling performance for forward/backward film cooling holes. At lower blowing ratios, some of the pressure side

edge holes remained inactive. Film cooling near the pressure side edge remains a challenge due to limited film coverage.

(5) Elevated swirl motion of the purge flow results in a narrower coverage and a lower laterally averaged effectiveness.

2.9 Results and Discussion – Comparison Between Cylindrical and Fan-Shaped Hole Designs

Area-averaged film cooling effectiveness values for three blowing ratios at three different density ratios were derived and compared, as shown in Figure 23. The area-averaged results are calculated (pixel by pixel) from x/C_{ax} = 0.3 to 1.2 to highlight the combined effects of discrete film cooling holes and the slashface film cooling. In other words, the influence of the purge flow is minimized. x/C_{ax} = 0.3 is located at the first pressure side edge hole exit (Group 2). Square, circular, and triangular symbols are used to represent data at DR = 1, 1.5, and 2, respectively. Solid symbols are used for results of fan-shaped holes while open symbols are used for results from cylindrical holes.

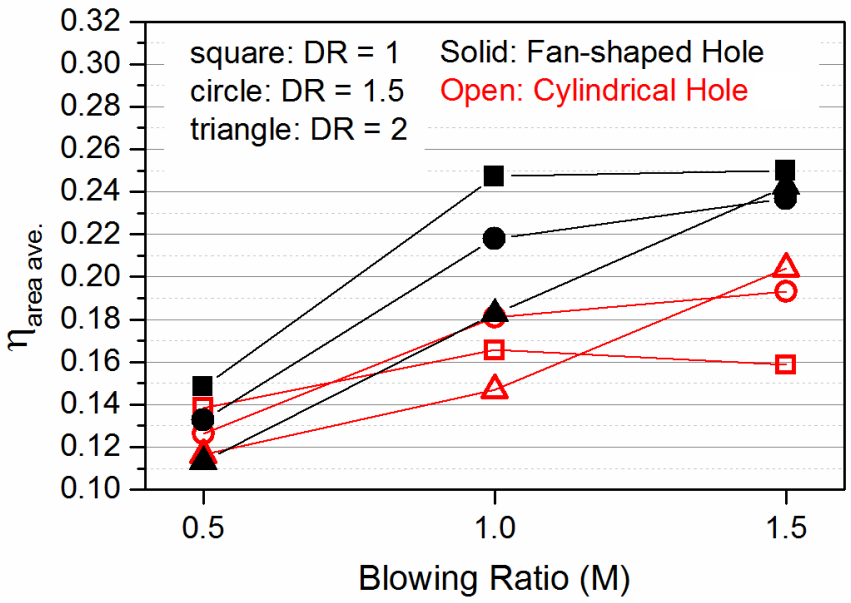

Figure 23 Area-averaged effectiveness comparison between cylindrical and fan-shaped holes. (Reprinted from Chen et al. [3])

There are nine data points for each hole geometry. At M = 0.5, all data points fall within $\eta_{area\ ave.}$ = 0.11 to 0.15. Under such low blowing ratio, cooling holes near the pressure side edge provide no coverage and coolant accumulates near the downstream portion. At higher blowing ratios, shaped hole clearly outperforms cylindrical hole. At DR = 1, effectiveness drops slightly for the cylindrical hole as blowing ratio increases from 1 to 1.5. It can be explained by the coolant lift-off effect of cylindrical holes and the slashface gap. For the shaped hole, the effectiveness remains at around $\eta_{area\ ave.}$ = 0.25. At DR = 1.5, the effectiveness increases for both geometries as blowing ratio increases from 1 to 1.5. Yet, the increment in effectiveness is reduced as compared with the increment from M = 0.5 to 1. At DR = 2, the area-averaged effectiveness seems to increase linearly with blowing ratio for both geometries. A higher effectiveness level can be expected at even higher

blowing ratios. The results indicate that shaped hole is a better choice in terms of platform film cooling. Under a density ratio that is close to engine conditions, a higher blowing ratio is desired for better film cooling performance.

The area-averaged effectiveness values are also plotted against momentum flux ratio (I) as shown in Figure 24. Dashed lines are the second order polynomial fitting of each hole shape at each DR. Solid lines are the second order polynomial fitting for all (nine) data points of each geometry. We can see that the effectiveness is low at $0.1 < I < 0.2$ regardless of hole geometry. Effectiveness increases (almost linearly) with increasing momentum flux ratio for both designs at DR = 2. As stated earlier, a higher effectiveness can be expected at higher I for both geometries at DR = 2. The data for shaped hole seems to be correlated better than the cylindrical hole. It may be explained by the fact that for cylindrical hole design, the slashface gap dominates the area-averaged effectiveness. The coolant coverage from the slashface gap may be larger than the coverage offered by all cylindrical cooling holes. From the solid trend lines, an optimum momentum flux ratio was seen at $I \approx 1.65$ for shaped hole design and $I \approx 1.35$ for cylindrical hole design. Also, the difference between the trend lines keeps increasing with increasing momentum flux ratio.

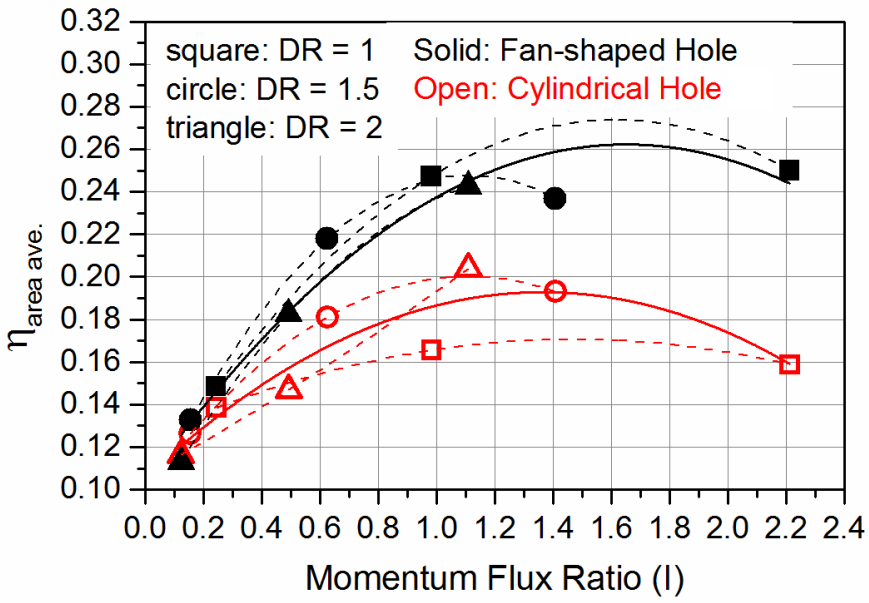

Figure 24 Area-averaged effectiveness comparison between cylindrical and fan-shaped holes versus momentum flux ratio. (Reprinted from Chen et al. [3])

2.10 Summary – Platform Film Cooling

Parametric effects on the purge flow MFR, purge flow swirl ratio, and the blowing and density ratios on the endwall film cooling with slashface gap, backward injection holes, and discrete cylindrical or fan-shaped holes have been studied and reported. Besides the individual film cooling characteristics of each cooling feature, the shaped hole design generally offers better film cooling performance than the cylindrical hole design. This is also true for backward injection holes near the leading edge. At DR = 2, area-averaged effectiveness increases almost linearly with increasing blowing ratio and momentum flux ratio for both hole geometries. As a result, higher effectiveness can be expected at $M > 1.5$ or $I > 1.1$ for density ratio 2 cases. Finally, shaped hole design seems to be better correlated with momentum flux ratio and has a delayed lift-off at $I \approx 1.65$. Effectiveness values between the two designs diverge with momentum flux ratio according to the second-order polynomial fit.

3. HEAT TRANSFER IN A ROTATING TWO-PASS RECTANGULAR CHANNEL FEATURING A CONVERGING TIP TURN WITH RIB COVERAGE EFFECTS

3.1 Literature Survey

Gas turbine engines are widely used for aircraft propulsion, land-based power generation, and numerous industrial applications. The efficiency of such technology is, therefore, a paramount issue for gas turbine researchers and designers. To achieve a higher thermal efficiency, one way is to increase the turbine inlet temperature (TIT) based on the working principle of gas turbine engines. The TIT of an advanced gas turbine engine has reached the 1600 °C level in around 2010. The combined cycle thermal efficiency of such engine has reached around 60%. Under this high TIT, it is imperative to properly cool the gas turbine components to ensure the safety and reliability of the engine.

The thermal load and temperature of a turbine airfoil can be reduced by two active cooling mechanisms: internal cooling and external (film) cooling. For internal cooling, high-pressure air at a much lower temperature from the compressor stage is sent to the internal passages of the airfoils. Heat is removed from the internal surfaces to the cooling air (coolant). Several techniques can be used to increase the heat transfer (HT) rate inside the passages, including artificially roughened surfaces (ribs or pin-fins) and jet impingement cooling. Several parameters that would affect the internal HT of the cooling channels have been identified, such as channel geometry and aspect ratio, rib configuration, rotation, 180 deg turn and turn geometry, and Reynolds number effects. A comprehensive review of various effects on internal HT can be found in Han [56], Han et al. [1, 57], and Ligrani [58].

3.1.1 Early Studies and Channel Geometry/Rib Effects

Heat transfer inside a serpentine internal cooling channel is complicated by nature. It is dependent on many parameters that may be intercorrelated with each other. Studies on these combinations of parameters are important to an improved cooling design. Some early studies focused on the rotation effect on heat transfer in a straight, smooth circular tube [59-61] due to the early designs (in the 1970s). In the 1980s, square or rectangular cooling channels were studied extensively as the internal cooling design evolved. Han et al. [62-64], and Park et al. [65] studied the heat transfer and pressure drop in rectangular channels with various aspect ratios (AR = 1:4 to 4:1) and rib configurations (α = 30-90 deg) in a straight channel under stationary condition. The results suggest that higher heat transfer performance was obtained with P/e = 10 and 45-60 deg ribs for narrower AR channels and 30-45 deg ribs for wider AR channels. Detailed heat transfer enhancement contours on the 60 deg rib-roughened internal surfaces were reported by Ekkad et al. [66]. Detailed heat transfer distributions on the leading and trailing surfaces, outer walls and tip wall with 45 deg ribs were obtained using computational fluid dynamics (CFD) by Schüler et al. [67]. These works offer an insight into the local heat transfer enhancements that are induced by angled ribs.

3.1.2 Rotational Effects in a Smooth Channel

Heat transfer in internal cooling passages can be significantly different under rotating condition. Also, serpentine cooling channels are typically used in an advanced turbine airfoil. Some early studies such as Wagner et al. [68, 69] and Han et al. [70], measured heat transfer in a multi-pass square channel with smooth walls under rotating

condition. It can be concluded that, for radially inward flow, heat transfer is enhanced on the leading surface and reduced on the trailing surface; for radially outward flow, heat transfer is reduced on the leading surface and enhanced on the trailing surface.

3.1.3 Rotation Effects in Ribbed and High Aspect Ratio Channels

Numerous studies on the rotation effect on heat transfer in a multi-pass rib-roughened channel with various channel aspect ratios can be seen in the open literature, such as Taslim et al. [71], Wagner et al. [72], Fu et al. [73], Lei et al. [74], and Huh et al. [75]. Different rib configurations under various flow and rotating conditions were investigated. The general conclusions from the above studies indicate that the heat transfer in rib-roughened wall passages has similar but reduced rotation-induced effects on the leading and trailing surfaces than the smooth wall passages. For high aspect ratio channels (AR = 4:1) in particular, Griffith et al. [76] studied the heat transfer in an open end channel (smooth and 45 deg rib) for Ro up to 0.3. They found a higher heat transfer enhancement in ribbed channel compared to lower AR cases. The leading surface has a lower dependence to rotation than the trailing and side surfaces. Saha and Acharya [77] numerically studied the detailed flow and heat transfer characteristics in ribbed passages. They found that the 4:1 AR duct shows the evidence of multiple rolls in the (rotation induced) secondary flow that reduces the difference between the leading and trailing wall heat transfer compared to lower aspect ratio cases. Zhou and Acharya [78] experimentally investigated heat transfer in a two-pass 4:1 AR channel with 45 deg ribs and a U-bend with a wide range of Reynolds number and rotation number.

3.1.4 180 degree Turn Effects

In a multi-pass channel, the geometrical design of the 180 deg turn has significant impacts on heat transfer in and after the turn portion. Han et al. [79] reported detailed heat/mass transfer distribution around a 180-deg sharp turn in a two-pass square channel using the naphthalene sublimation technique. Results showed that heat transfer was greatly enhanced after the 180 deg sharp turn for both smooth and ribbed channels. Flow measurements using particle image velocimetry (PIV) technique in ribbed channels with 180-deg sharp turn were carried out by Schabacker et al. [80]. Complicated rib-induced and turn-induced secondary flows were observed in the 180-deg sharp turn region. Under rotating condition, the combined effect of rotation and turn further increases the complexity of the flow and heat transfer. Cheah et al. [81] measured the flow field in a channel with 180 deg U-bend under rotating condition using the laser-Doppler anemometry (LAD). They found that rotation can change the mean and fluctuating motion of the flow substantially within and downstream of the sharp U-bend. Liou and Chen [82] measured the heat transfer coefficients and flow fields inside a rotating two-pass rectangular smooth channel with a 180 deg turn. The results show that the turn-induced secondary flows and the turbulence enhancement associated with the unsteadiness of the separation bubble downstream of the sharp turn are the cause of the significant heat transfer increment in the second passage.

3.1.5 Studies with a Varying Aspect Ratio Channel

All of the above-mentioned studies with multi-pass channels were performed inside a channel with a constant cross-sectional area and aspect ratio for all passages. However,

the cross-sectional area and aspect ratio of a serpentine internal cooling channel are found varying in a real gas turbine engine airfoil. More recently, studies on heat transfer in a multi-pass channel with engine-similar channel geometries can be seen in the open literature. Under stationary condition, Eifel et al. [83] examined the flow and the heat transfer in an engine-like model with four different internal cooling geometries numerically. Jenkins et al. [84] studied the effects of ribs and tip wall distance on heat transfer in a two-pass channel with AR = 1:2 (W:H) inlet and 1:1 outlet using transient liquid crystal technique. CFD simulations were performed by Siddique et al. [85, 86] to compare with the results of Ref. [84]. Under rotating condition, Schüler et al. [87] investigated the effect of rotation on fluid flow and heat transfer in an engine-similar two-pass internal cooling channel with smooth and ribbed walls using CFD simulation. The channel featured a trapezoidal inlet pass and a nearly rectangular outlet pass. Rallabandi et al. [88] and Yang. et al. [89] experimentally investigated the heat transfer in a rotating large scale blade shape serpentine coolant passage at high Reynolds numbers or low Mach numbers. Wu et al. [90] and Yang et al. [91] reported effects on heat transfer in a rotating multi-pass channel with a gradually expanding hub turn and a turning vane and trailing edge ejection.

3.2 Objectives

There is a limited number of studies on engine-similar channel geometries. Among these studies, research with a reduced cross-section and aspect ratio after the turn is scarce. In the present study, a more generalized two-pass rectangular channel with AR = 4:1 in the first pass (radial outward flow) and AR = 2:1 in the second pass (radial inward flow) is proposed to simulate the varying cross-section design in a real engine. Flow acceleration and compression at the 180 deg tip turn will be induced with the current model. Flow velocity and streamlines in the baseline smooth surface case will be visualized with a simple CFD simulation. Roughened surfaces with 60 deg angled ribs as well as 45 deg angled ribs with various rib coverage near the tip turn portion have been considered. Experimental results on the effects of rotation on heat transfer and pressure loss under a broad range of Reynolds number (Re = 10k-70k) and rotation number (Ro = 0-0.39) will be presented.

3.3 Experimental Setup and Design

3.3.1 Test Conditions and Rotating Facility

The rotation number (Ro) is used to evaluate the degree of Coriolis force inside the test channel. It is derived from the ratio between the Coriolis force and the inertia force and is defined in Eq. (4):

$$Ro = (\Omega D_h)/U_b \tag{4}$$

where Ω is the rotational speed, D_h is the hydraulic diameter, and U_b is the bulk fluid velocity. The rotation number and Reynolds number in a typical aircraft or land-based gas turbine engine range from 0 to 0.5 and 10,000 to 100,000, respectively, depending on the design and operating conditions. For a safe operation under a laboratory setting, the rotational speed and the dimension of the test section are usually limited. To achieve the high rotation numbers as seen in the engine, the bulk fluid velocity should be reduced. For the present study, experiments were done under a pressurized condition. The air pressure at the test section inlet was maintained at 570 kPa (68 psig). With this high pressure, the density of the coolant air will be increased, and hence the bulk velocity will be reduced. Eight Reynolds numbers were tested (10,000 to 70,000 in the first passage and 16,000 to 114,000 in the second passage). At each Reynolds number, five rotational speeds from 0 rpm (stationary) to 400 rpm were considered. Detailed Reynolds numbers, rotational speeds, and the corresponding rotation numbers for both passage 1 and passage 2 are listed in Table 4 and Table 5, respectively.

Table 4 Test conditions and corresponding Ro numbers in the first passage

rpm \ Reynolds number ($*10^{-3}$)	10	15	25	35	45	55	65	70
0	0	0	0	0	0	0	0	0
100	0.10	0.07	0.04	0.03	0.02	0.02	0.02	0.01
200	0.20	0.13	0.08	0.06	0.04	0.04	0.03	0.03
300	0.29	0.20	0.12	0.08	0.07	0.05	0.05	0.04
400	0.39	0.26	0.16	0.11	0.09	0.07	0.06	0.06

Table 5 Test conditions and corresponding Ro numbers in the second passage

rpm \ Reynolds number ($*10^{-3}$)	16	24	41	57	73	90	106	114
0	0	0	0	0	0	0	0	0
100	0.04	0.03	0.02	0.01	0.01	0.01	0.01	0.01
200	0.08	0.05	0.03	0.02	0.02	0.01	0.01	0.01
300	0.12	0.08	0.05	0.03	0.03	0.02	0.02	0.02
400	0.16	0.11	0.06	0.05	0.04	0.03	0.02	0.02

The rotating arm facility used to conduct the experiments was supported by a heavy steel table, as shown in Figure 25. A 25 hp electric motor was used to drive the vertical rotating shaft that located at the center of the table. There are two horizontal arms that extend from the vertical shaft. A steel pressure vessel enclosing the test section is attached to the end of an arm. An adjustable counterweight was fixed to the other arm for balance under rotation. Compressed air was supplied by a 125 psig compressor. The mass flow rate was controlled by a regulator and measured by an ASME square-edge orifice meter. Air at a certain mass flow rate then enters the rotating assembly from the bottom of the shaft through a rotary union, passes through the internal channel in the shaft and the arm. A rubber hose is used to direct the air from the arm to the test section pressure vessel. The

hot exhaust air exits the pressure vessel through another rubber hose and is directed to a copper tube that connects the rubber hose and the top rotary union through the center bore of the slip-rings. A needle valve at the downstream of the top rotary union is used to control the inlet pressure of the system.

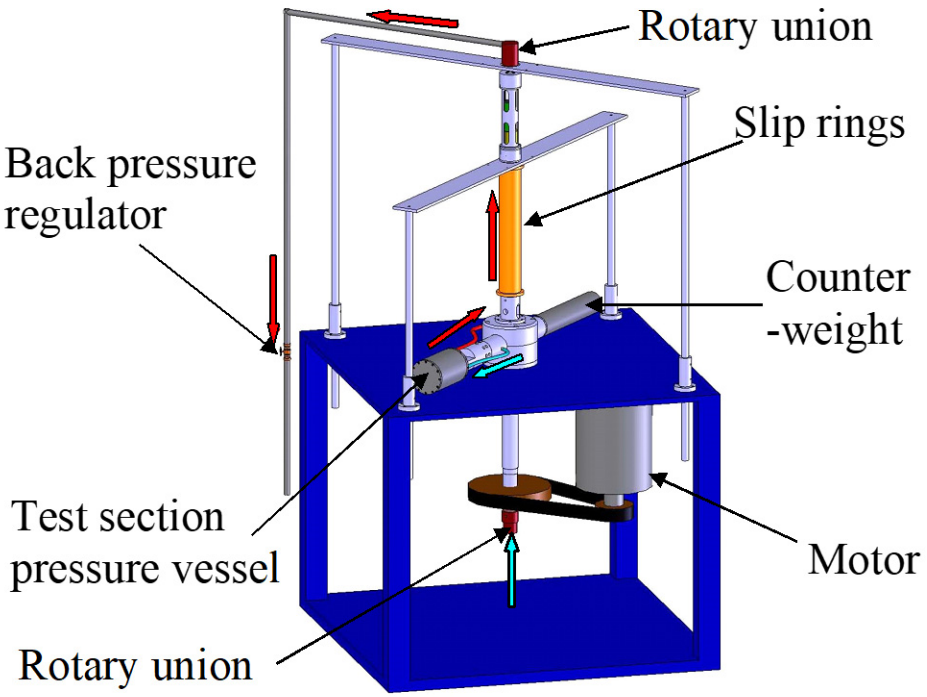

Figure 25 Schematic of the rotating test facility

3.3.2 Test Section and Rib Design

The design of the test section inside the pressure vessel is illustrated in Figure 26. The radial distance from the rotation axis to the center of the test section is 635 mm. The two-pass model has two passages and a 180 deg tip turn. The leading surface of the test section is removed to show the complete assembly of the inner wall, outer wall, tip wall and the trailing surface as viewed from the leading side to the trailing surface. All lengths are non-dimensionalized by the rib height (e) as indicated in Figure 26. The height of the channel remains constant at 6.4e. The coolant air enters the test section through a circular hole on the test section adaptor, then readily enters the expansion section at the inlet. There are three layers of wire meshes inside the expansion section to expedite the flow distribution. The flow then enters the AR = 4:1 rectangular channel (radial outward flow, channel width = 25.6e). After the 180 deg tip turn, the flow enters the second passage with an aspect ratio of AR = 2:1 (radial inward flow, channel width = 12.8e). The second passage is connected to the exit duct with a 180 deg hub turn to simulate the flow exit condition. The spent air exits from the exit duct and enters the pressure vessel. After circulating in the pressure vessel, the flow exits through two exit holes on the adaptor to the outlet piping.

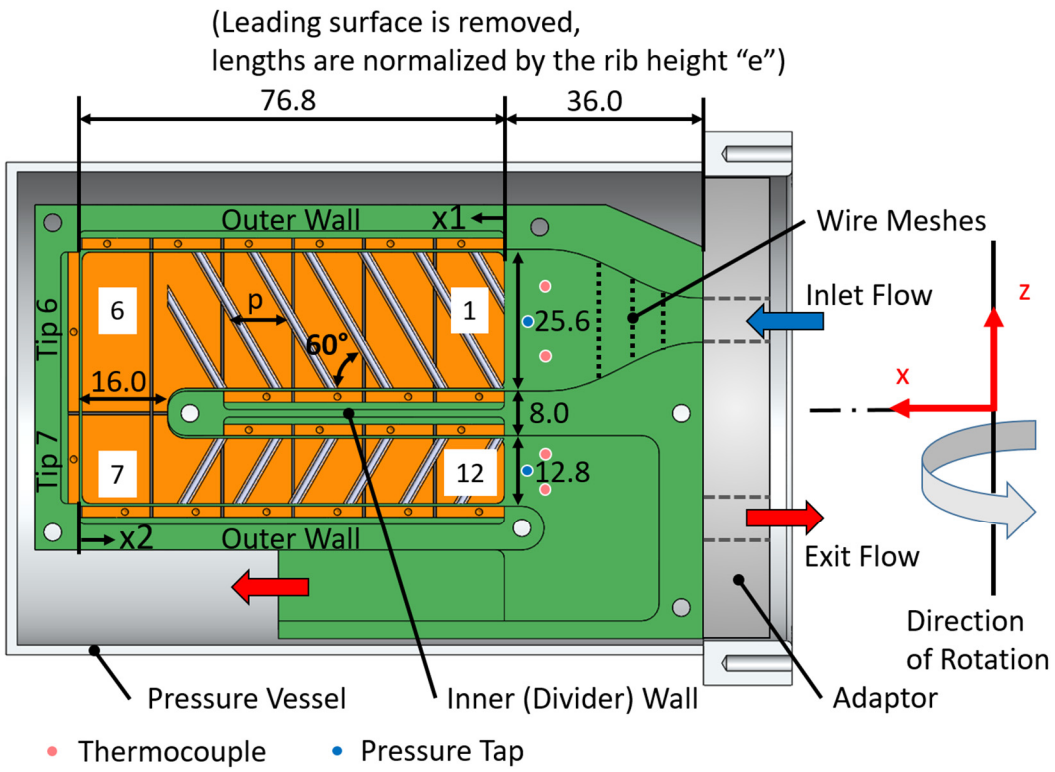

Figure 26 Schematic figure of the test section as viewed from the leading side to the trailing surface (with 60 deg angled ribs)

The inner wall (or divider wall) has a width of 8.0e. The distance between the tip of the divider wall and the tip wall is 16.0e. The length of the unheated expansion zone at the inlet is 36.0e and the length of the heated zone is 76.8e. The body of the test section is made of Garolite G-10 through machining. The heated zone is divided into 6 regions in the radial direction and the radial distance of each region is 12.8e. The test section is divided into 12 regions in the streamwise direction as indicated in Figure 26. Regions 6 and 7 near the tip is divided along the centerline of the inner wall. Copper plates (thickness = 2e) are placed in each region and there is a gap (0.5e) filled by insulation material between each copper plate to prevent thermal conduction. Copper plates and heaters are installed on all surfaces of the channel within the heated zone, including regions 1 to 4 and 9 to 12 on both sides of the inner wall. As a result, there are total 46 regions and copper plates. One thermocouple is affixed inside the blind hole (0.79 mm in diameter) located at the center of each copper plate from the back side by a high thermal conductivity epoxy (OB-101, OMEGA Engineering, Inc. Norwalk, CT). Total 46 thermocouples are used for 46 copper plates to monitor the wall temperatures. Two thermocouples are placed at the inlet and outlet respectively for flow temperature measurement. Total 9 Kapton heaters (Heater Designs, Bloomington, CA) are used to heat the internal surfaces: leading surface, trailing surface, outer surface, and inner surface for both passage 1 and passage 2 plus the tip surface. The heaters are securely attached on the backside of the copper plates by a thin layer of pressure-sensitive adhesive. In addition to temperature measurements, a total of four pressure taps are installed on the LS and TS near the inlet and outlet of the test section for pressure measurements.

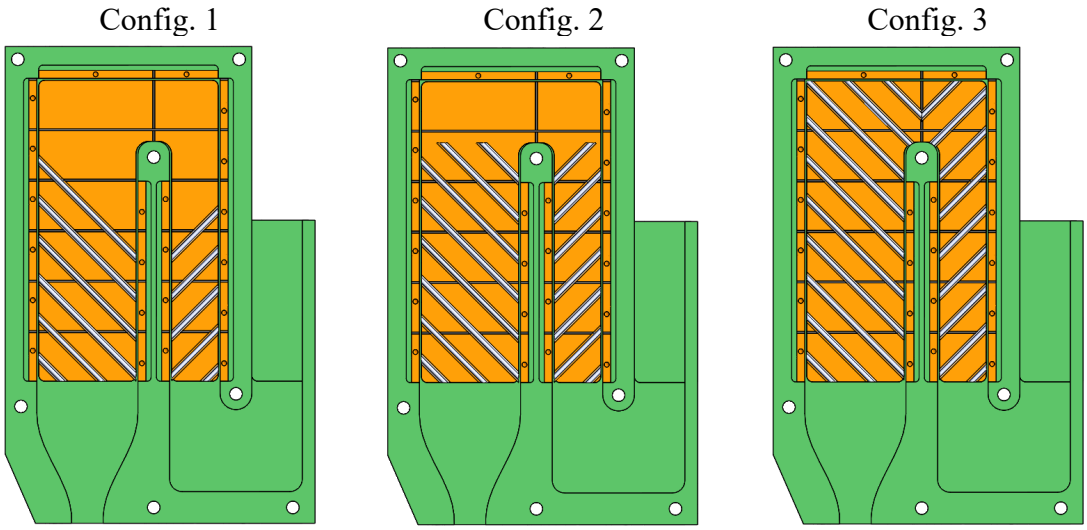

Figure 27 Rib designs for the 45 deg angled rib with various rib coverages near tip turn. (a) less coverage (Config. 1) (b) medium coverage (Config. 2) and (c) full coverage (Config. 3)

A total of five different test section configurations were studied, including the baseline smooth surface case, the 60 deg parallel rib case and the 45 deg parallel rib with less, medium and full coverages near the 180 deg tip turn (Figure 26 and Figure 27) For the rib-roughened case, 60 deg or 45 deg parallel ribs were placed on the leading surface and trailing surface in both passage 1 and passage 2 (inline, not staggered). For the 60 deg rib and 45 deg medium rib coverage cases, the ribs only cover up to the tip of the inner wall, leaving regions 6 and 7 without ribs and regions 5 and 8 partially covered. For the 45 deg less rib coverage case, two ribs near the turn in both passages are removed (on either the LS or the TS) as shown in Figure 27 (a). For the 45 deg full rib coverage case, the ribs cover the entire LS and TS, as shown in Figure 27 (c).

The cross-sectional profile of the rib is shown in Figure 28. The rib height is denoted as “e”. The base of the rib is 2e wide. The ribs were fabricated by direct metal laser sintering (DMLS) using aluminum-based powder (AlSi10Mg), with a thermal conductivity of 120-180 W/m/K. The resolution was ± 0.05 mm in the X-Y direction and 0.15 mm in the Z (rib height) direction. The 3-D printed parts were later machined to the desired dimension. The thickness of the two sharp edges is around 0.08e and is limited by machinability. The pitch over rib height ratio is p/e = 10. Ribs are attached to the smooth surface by a thin layer (glue thickness = 0.04-0.05 mm) of super glue (Loctite 414). The thickness of the glue is so thin that the thermal resistance is considered small and negligible.

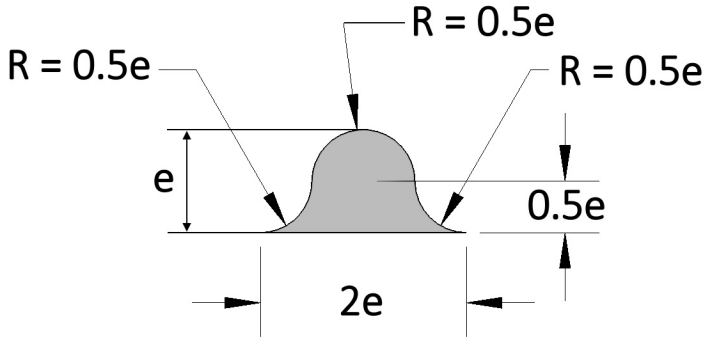

Figure 28 Rib cross-sectional profile

3.3.3 Instrumentation and Data Acquisition

T-type thermocouples were used for wall temperature and fluid temperature measurements. T-type thermocouple pin and socket connectors (SMTC-CU and SMTC-CO, OMEGA Engineering, Inc.) were used for all thermocouple wire connections. Two

pressure transducers were used to measure the static pressure at the inlet. Another two high accuracy pressure transducers were used to measure the pressure drops on the LS and TS, respectively. A multi-channel data acquisition system (cDAQ-9188, National Instruments, Austin, TX) with temperature (NI-9213, National Instruments) and pressure (NI-9219, National Instruments) modules was mounted on the rotating frame. An industrial grade wireless router (MOXA AWK-3121, Taiwan) was used to transmit real-time temperature and pressure data wirelessly to a remote computer. All electronic components are installed very close to the rotating shaft to minimize the centrifugal acceleration. A 50-channel slip ring was used to transmit power to the heaters and electronic equipment. Nine individual variable transformers were used to supply power to each heater. The voltage applied to each heater was measured by a digital multimeter. A DC power supply was used to power the onboard electronics.

3.4 Experimental Method and Data Reduction

The copper plate method is used to measure the regionally averaged heat transfer coefficient. The averaged heat transfer coefficient (h) for each region (n) can be expressed by Eq. (5), where the $Q_{net,n}$ is the net power input, A_n is the smooth surface (projected) area of the copper plate, $T_{w,n}$ is the wall temperature, and $T_{net,n}$ is the bulk fluid temperature. At each region, $T_{w,n}$ was measured by the thermocouple inside the copper plate and $T_{net,n}$ was interpolated from the inlet and outlet fluid temperatures.

$$h_n = \frac{Q_{net,n}}{A_n(T_{w,n} - T_{b,n})} \tag{5}$$

The net power input ($Q_{net,n}$) of each copper plate is calculated as the total power input to each heater times the ratio of the copper plate surface area (A_n) to the summation of all copper plate surface areas associated with that heater ($\sum A_n$), minus the heat loss at region n ($Q_{loss,n}$), as shown in Eq. (6). The power of the heater is calculated by the square of the voltage (V) divided by the resistance of the heater (R). The temperature dependence of the heater resistance was small and assumed negligible (less than 1 % for 7 out of 9 heaters under elevated temperature).

$$Q_{net,n} = \left(\frac{V^2}{R}\right)\left(\frac{A_n}{\sum A_n}\right) - Q_{loss,n} \tag{6}$$

To estimate the heat loss, several steps were taken with two key assumptions. First, steady state heat losses under a no-flow condition at both high and low power inputs were obtained at five rotational speeds (0 to 400 rpm). Heat loss will be increased under rotating condition. Thus, it is necessary to perform heat loss test at all rotational speeds. The wall temperatures of each region at both high and low power under equilibrium condition were recorded. The average wall temperature of all regions under high and low power inputs was about 59 deg C and 40 deg C, respectively. Wall temperatures during the HT test will be maintained within this range. The heat fluxes at two different power inputs for each region were also recorded. The heat loss at region n under no-flow condition ($Q_{loss,no\text{-}flow,n}$) can then be estimated by linear interpolation using the wall temperature during the HT test. However, during the test, the spent air was exhausted into the space between the test section

and the pressure vessel from the exit duct. The convection inside the pressure vessel changed from natural convection (in the no-flow calibration) to forced convection (in real testing). It is nearly impossible to derive the local heat transfer coefficients (HTC) on the external surfaces of the test section under test condition. As a result, it is assumed that the forced convection HTC under test condition is the natural convection HTC under the no-flow calibration condition times a scaling factor (σ) for each region. It can be expressed by Eq. (7). Where σ is a scaling factor and the value will be varied at different Reynolds numbers and rotational speeds. It is also assumed that the σ is the same for all regions under a particular test condition.

$$h_{forced,n} = \sigma h_{natural,n}\,, for\ all\ n \tag{7}$$

From the above assumptions, the regional heat loss can be expressed by Eq. (8).

$$Q_{loss,n} = \sigma Q_{loss,no-flow,n} \tag{8}$$

To derive σ under each test condition, the following equation Eq. (9) is used. Where $\dot{m}$ is the coolant mass flow rate (kg/s) and C_p is the averaged heat capacitance (1005 J/kg/K) of the coolant. T_{outlet} and T_{inlet} are the fluid temperatures measured at the outlet and inlet, respectively.

$$\sum_{1}^{9} \frac{V^2}{R} = \left[\dot{m} C_p (T_{outlet} - T_{inlet})\right] + \sigma \times \sum_{n=1}^{46} Q_{loss,no-flow,n} \quad (9)$$

With Eq. (5) – Eq. (9), the HTC at each region can be derived. The Dittus-Boelter correlation for heating is used to calculate the Nusselt number (Nu_0) for fully developed turbulent flow inside a smooth circular pipe. It is used as a reference for heat transfer enhancement (Nu/Nu_0 ratio) in the current study. The regional Nu/Nu_0 ratio is given by Eq. (10):

$$\left(\frac{Nu}{Nu_0}\right)_n = \frac{\left({h_n D_h}/{k}\right)}{0.023 Re^{0.8} Pr^{0.4}} \quad (10)$$

The HTC is obtained from Eq. (5). The hydraulic diameter (D_h) and Reynolds number (Re) are based on each passage. The thermal conductivity of air (k) is based on the local bulk air temperature ($T_{net,n}$). To evaluate the rotation effect on heat transfer, the Nusselt number obtained under rotating condition is divided by the Nusselt number obtained under stationary condition (Nu_s).

Pressure drops across the two-pass channel are measured under non-heating condition for both configurations under stationary (K_s) and rotating (K_r) conditions. The pressure loss coefficient is defined in Eq. (11):

$$K = (P_{inlet} - P_{outlet}) / \left(\frac{1}{2} \rho {U_b}^2\right)_{ave} \quad (11)$$

Where ($P_{inlet} - P_{outlet}$) is the static pressure difference between the channel inlet and outlet on either the LS or TS. $(\rho U_b^2/2)_{ave}$ is the average fluid dynamic pressure of the two passages, i.e. $(\rho_1 U_{b1}^2/2 + \rho_2 U_{b2}^2/2)/2$.

3.5 Experimental Uncertainty

The uncertainty of the flow Reynolds number was ± 4.3% at Re = 10k and ± 0.5% at Re = 70k. This indicates the fluctuation of the coolant mass flow rate. The uncertainty of temperature measurement and power measurement were estimated at ± 0.2 °C and ± 3%, respectively. The uncertainty in heat transfer coefficient measurement disregarding the heat loss and flow fluctuation was below 4.5%. In terms of heat loss, the total heat loss accounts for about 31% of the total power input at the lowest Reynolds number (Re = 10k) and 14% at the highest Reynolds number (Re = 70k), for the smooth case under stationary condition. The heat loss percentage was relatively high due to the forced convection inside the pressure vessel. Considering the two assumptions made for the heat loss estimation, an additional uncertainty of 20% is assumed for the estimated heat loss. Now the heat loss contributes about 30%*20% = 6% error for Re = 10k and 14%*20% = 2.8% for Re = 70k, then the overall uncertainty goes up to around 10.3% for Re = 10k and 5.1% for Re = 70k. The uncertainties for the inlet static pressure and channel pressure drops are 0.25% and 0.08%, respectively. The resultant uncertainty in the loss coefficient is below 5% for most of the cases studied. Uncertainties are estimated using the method proposed by Kline and McClintock [55].

3.6 Test Matrix

As discussed in section 3.3.1 and 3.3.2, there are five different rib configurations including the smooth surface case. For each configuration, 8 Reynolds numbers varied from 10k to 70k at 5 rotational speeds from 0 to 400 rpm were tested. As a result, there are a total of 5*8*5 = 200 test cases.

3.7 Results and Discussion – Smooth Surface and 60 deg Angled Ribs

Heat transfer results in terms of Nusselt number ratios will be presented for both smooth surface and 60 deg rib-roughened surface under stationary and rotating conditions. Reynolds number (Re) from 10k to 70k and rotation number (Ro) from 0 to 0.39 were covered. The heat transfer characteristics of an internal cooling channel featuring varying aspect ratio (AR = 4:1 to 2:1) and a converging 180 deg tip turn will be discussed. Smooth surface results with a simple CFD simulation will be presented in the first part followed by the 60 deg rib-roughened results in the second part. Data validation is provided and discussed for both configurations. Pressure loss coefficient results are presented in section 3.9.

3.7.1 Smooth Surface Results

CFD simulation was performed at a medium Reynolds number (Re = 45k) for the smooth wall under stationary condition. Streamlines at the middle plane between the LS and TS are shown in Figure 29. The simulation was run using the commercial software ANSYS Fluent v17.2 and the realizable k-ε (Menter-Lechner) model. A uniform velocity inlet and a pressure outlet were assumed. The grid sensitivity test has been performed and

the final model has a total 2.07 million cells. The velocity is normalized by the inlet velocity. The flow is uniform near the inlet, then it starts to deflect in regions 5 and 6 due to the tip turn. The turn induced two circulation bubbles inside the two-pass channel. One is located at the corner between the tip wall and outer wall in region 6. The second one is located at the inner wall right after the turn in regions 8 and 9. Unlike traditional constant cross-section and aspect ratio channels, the current reduced cross-section design induced flow acceleration in and after the turn. The accelerating flow has three major effects. The first effect is that the corner vortex which can normally be seen in the second passage of a two-pass square duct is diminished (between the tip wall and outer wall in region 7). Secondly, the size of the circulation bubble (or flow separation) that can be typically seen near the inner wall after the 180 deg turn [82] is significantly reduced. Thirdly, the accelerated flow is expected to elevate the heat transfer coefficients in the second passage. However, the relative heat transfer enhancement (Nu/Nu_0, based on the second passage) is reduced due to the relatively weakening of the secondary flows compared to constant AR channels. It seems that the accelerating flow in this converging 180 deg bend reduced the flow instability and turbulence intensity. Flow impingement on the tip wall in region 6 and on the outer wall in regions 7 and 8 can be seen clearly and is expected to enhance the heat transfer.

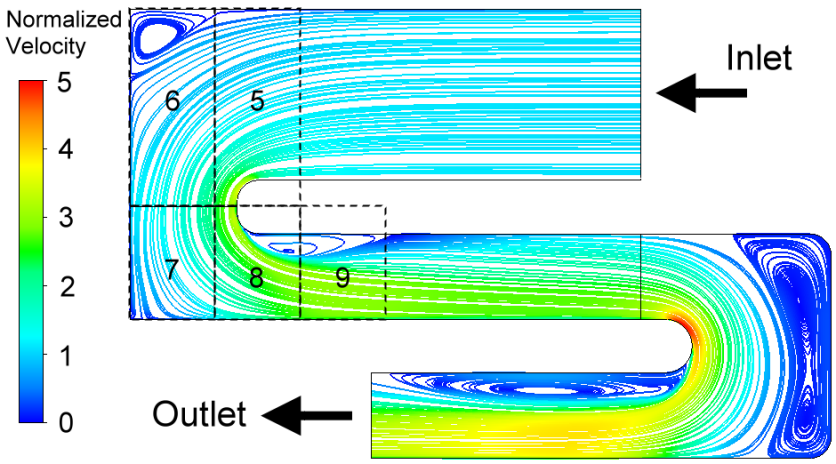

Figure 29 CFD simulated velocity streamlines at the middle plane at Re = 45k, 0rpm

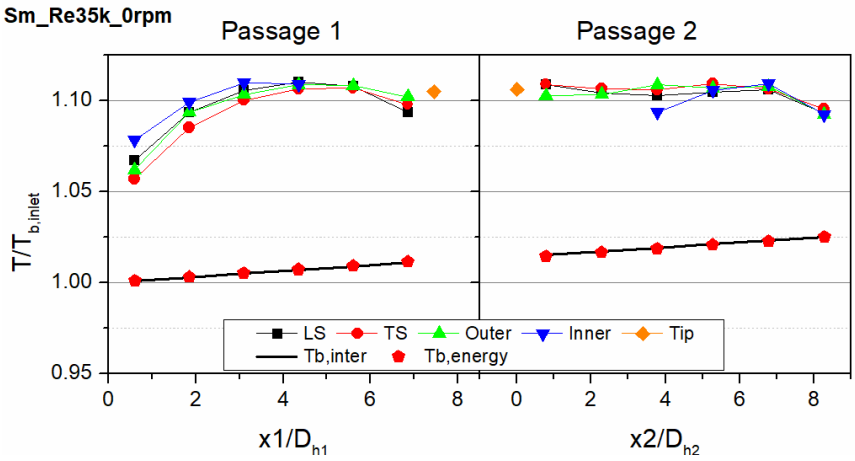

(a)

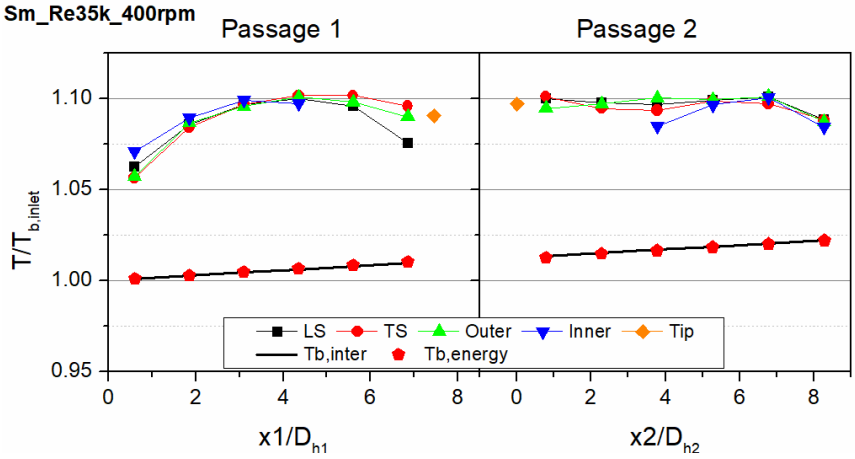

(b)

Figure 30 Smooth surface temperature distribution at Re = 35k under (a) 0 rpm and (b) 400 rpm

Wall temperature distributions at a selective Reynolds number Re = 35k under stationary (0 rpm) and the highest rotational speed (400 rpm) are presented in Figure 30. Temperatures are normalized by the bulk air temperature at the inlet ($T_{b,inlet}$). The bulk temperature increases gradually from the inlet toward the outlet. This is expected under constant heat flux boundary condition. An energy balance calculation was performed based on the calculated regional heat loss. Since the heat loss calculation was based on the inlet and outlet temperatures, the bulk temperature derived from the energy balance method ($T_{b,energy}$) at the outlet was forced to be identical to the measured outlet temperature ($T_{b,outlet}$). The $T_{b,energy}$ shows great consistency with the interpolated bulk temperature ($T_{b,inter}$) in all regions. The wall temperatures for all regions were maintained at around 1.05 to 1.11 times of the inlet temperature. Heat conduction between adjacent regions was minimized by controlling the power of each heater so that the wall temperature difference of all adjacent regions was reduced. In Figure 30 (a), the wall temperatures at the inlet are lower than other regions due to higher heat transfer and higher conduction heat loss. The temperature gradually increases up to $x1/D_{h1} = 4.35$ then gradually decreases near the tip. This trend indicates that the heat transfer is higher near the tip turn portion. The wall temperatures show less variation in the second passage except for the last data point which is located at the outlet. The lower temperature is also a result of higher conduction heat loss. The temperature distribution under rotating condition Figure 30 (b) is very similar to the stationary condition. However, the power required to maintain a small temperature difference between adjacent regions will be different. The difference in power inputs will result in different HTCs under rotating conditions.

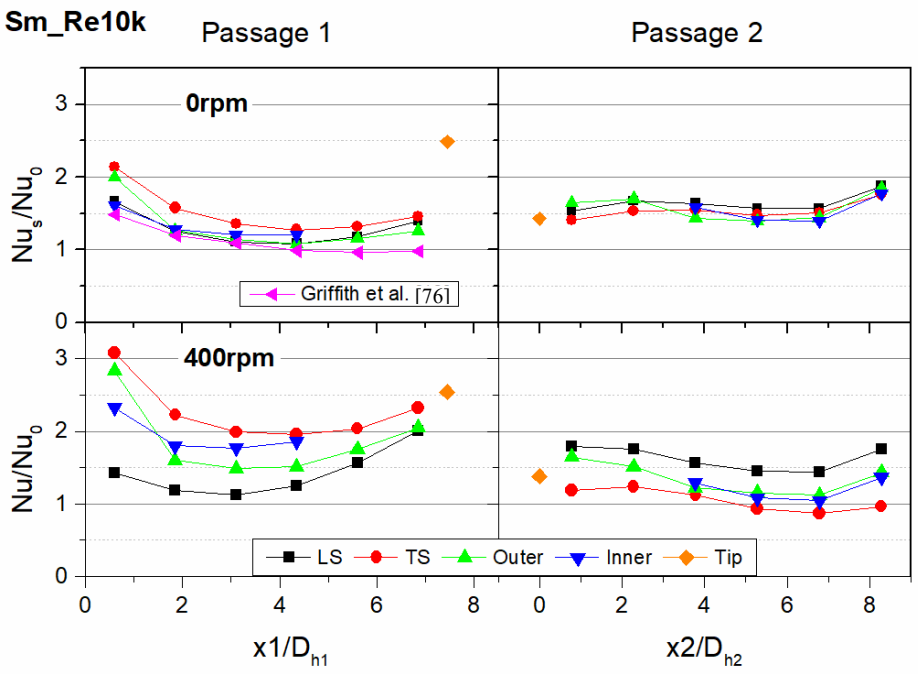

Figure 31 Smooth surface streamwise Nu/Nu_0 ratio at Re = 10k under 0 and 400 rpm

Figure 31 shows the streamwise Nu/Nu_0 distributions on the leading surface (LS), trailing surface (TS), inner wall (Inner), outer wall (Outer) and tip wall at Re = 10k and rotational speeds of 0 and 400 rpm. For the stationary case, a higher heat transfer (Nu/Nu_0 = 1.6-2.2) was observed near the entrance due to the developing thermal and momentum boundary layers. In the near fully-developed region ($x1/D_{h1} \approx 4$), the Nusselt number ratio Nu/Nu_0 for all four surfaces dropped to 1.1-1.3. The enhanced heat transfer compared to the Dittus-Boelter correlation is a result of the high aspect ratio rectangular channel as well as the developing flow. As the flow approaches the turn region ($x1/D_{h1}$ = 5-7), heat transfer increases slightly to around 1.4. The results in the first passage are in good agreement with Griffith et al. [76] (Re = 10k) in which an AR = 4:1 single pass channel was used. The

results are about 20% higher than the reference in the developing zone and may be attributed to the entrance geometry effect. The tip wall in the first passage has the highest heat transfer enhancement ($Nu/Nu_0 = 2.5$) due to the impingement of the radial outward flow. The difference between the leading surface and the trailing surface is believed to be caused by the imperfect surface roughness. Nevertheless, this effect is expected to be eliminated in the Nu/Nu_s ratio comparisons because the surface roughness acts in the same way for both cases.

In the second passage, Nu is based on the hydraulic diameter of passage 2 D_{h2} and Nu_0 is based on the Reynolds number in passage 2. The Nu/Nu_0 values are around 1.5 from $x2/D_{h2} = 0$ to 7. Heat transfer at $x2/D_{h2} = 2.3$ is slightly higher due to the turn-induced secondary flows. However, as discussed earlier, the effect is smaller than usual due to the suppressed secondary flows and turbulence in an accelerating flow. Heat transfer at $x2/D_{h2} = 0.8$-2.3 for the outer wall is also slightly higher than the LS and TS due to flow impingement. At 400 rpm, a positive rotation effect can be seen clearly on the TS, inner wall and outer wall in passage 1. In passage 2, a negative effect can be seen on the TS, as well as the inner wall and outer wall for $x2/D_{h2} = 2.3$-8.3. The rotation effects on the TS in passage 1 and passage 2 follow the general trends as found in previous studies (such as Refs. [69-71, 73, 74]).

The rotation effects in terms of the rotation number Ro will be discussed for selected surfaces and regions in the first pass, tip turn, and second pass. These representative surfaces include the LS and TS in regions 4 and 6 in passage 1 and regions 7 and 11 in passage 2, as well as the Tip surfaces in regions 6 and 7. To show the rotation effect more clearly, the rotating Nusselt number is normalized by the stationary Nusselt number (Nu_s). Thus, for a rotation number Ro = 0, the Nu/Nu_s ratio is 1.

Figure 32 shows the rotation number effect on LS and TS heat transfer in regions 4 and 6 in the first passage. Since the rotation number is relatively small at higher Reynolds numbers, the results for lower Re (Re = 10k and 15k) and higher Re (Re = 25k to 70k) are shown separately for better legibility. In general, heat transfer on the TS in both regions 4 and 6 continually increases with increasing Ro with up to 61% relative to zero rotation as expected. However, some negative effect with up to 9% can be seen at higher Reynolds numbers in part of the Ro range (Ro ≈ 0-0.12). For LS-4, Nu/Nus first decreases with Ro with up to 21% until Ro ≈ 0.13 then gradually increases to Nu/Nus = 1.16 at Ro = 0.39. This trend is very similar to the results found in Ref. [76]. For LS-6, the effect is generally positive with up to 46% increase except for Re = 15k, 25k, 35k and 45k at Ro ≈ 0-0.13.

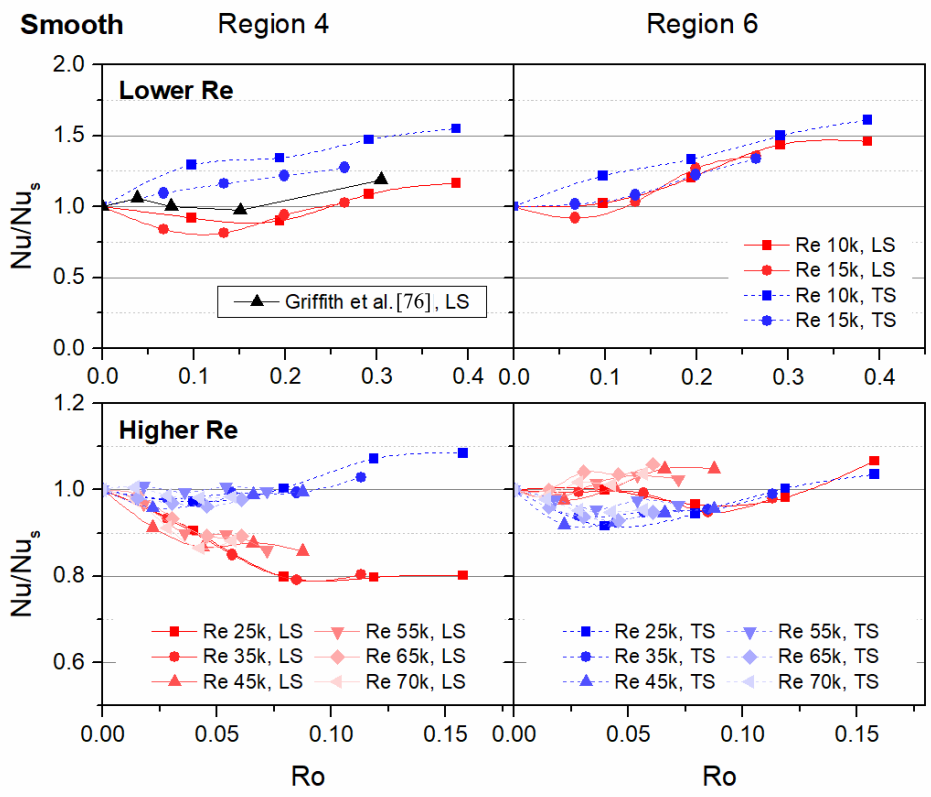

Figure 32 Effect of rotation number (Ro) on LS and TS heat transfer (Nu/Nu_s) in regions 4 and 6 for smooth case

Figure 33 shows the rotation effect on the LS and TS in regions 7 and 11 in the second passage. For the TS, the Nu/Nus shows a general decreasing trend with increasing Ro with up to 42% in region 11. This trend is also what is expected for a radial inward flow. For LS-7, the heat transfer increases with increasing Ro with up to 20% at lower Reynolds numbers. However, at higher Reynolds numbers, the Nu/Nu_s shows an increasing and then decreasing trend between Ro = 0 and 0.05. Rotation has a small positive effect (5-9%) on heat transfer on LS-11 at low rotation numbers, i.e. Ro = 0-0.03 for higher Re and Ro ≈ 0-0.12 for lower Re. Nu/Nu_s decreased up to 7% at the highest Ro.

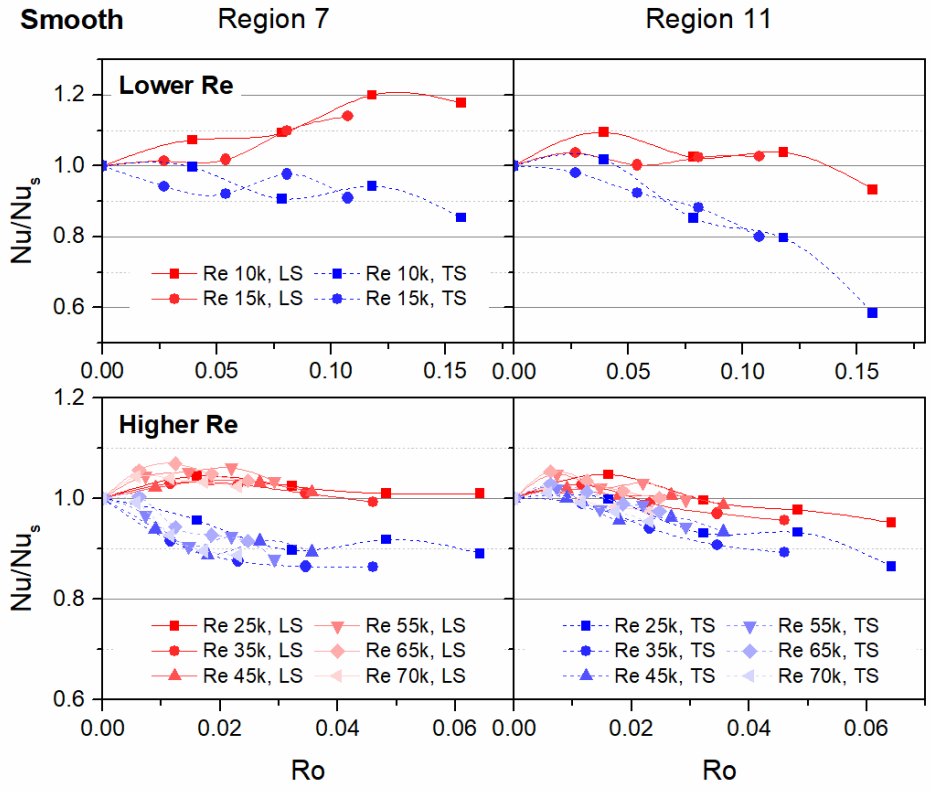

Figure 33 Effect of rotation number (Ro) on LS and TS heat transfer (Nu/Nu_s) in regions 7 and 11 for smooth case

The effect of rotation on heat transfer on the tip wall is shown in Figure 34. For both Tip-6 and Tip-7, heat transfer first decreases with rotation number then increases. This trend is quite different from a typical two-pass channel, in which the tip heat transfer increases with rotation number due to the pumping effect induced by the centrifugal force. For Tip-6, Nu/Nu_s reduces to 0.72 at Ro = 0.1 then gradually increases to 1.03 at the highest Ro. For Tip-7, Nu/Nu_s drops 36% at Ro ≈ 0.04 then increases to 0.98 at the highest Ro. Also, for both regions, there is a significant Reynolds number dependence. There is less rotation number effect at higher Reynolds numbers.

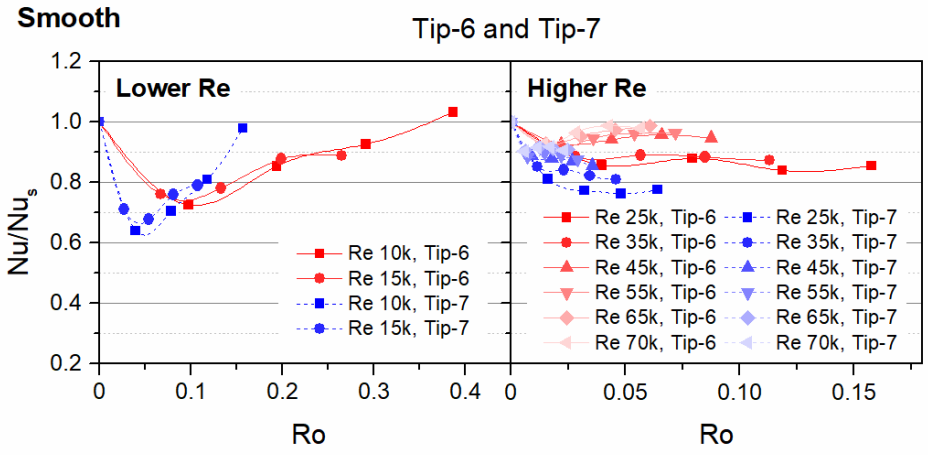

Figure 34 Effect of rotation number (Ro) on Tip wall heat transfer (Nu/Nu_s) in regions 6 and 7 for smooth case

3.7.2 60 deg Rib Roughened Surface Results

The rib-induced secondary flows will change the heat transfer characteristics under both stationary and rotating conditions. Figure 35 shows the streamwise Nus/Nu_0 distribution for the rib-roughened case at a selective Re = 35k under stationary condition. Similar to the smooth case, the first and last data points should be neglected due to higher conduction heat loss. The Nus/Nu_0 values on the LS and TS reach around 2.6 in passage 1 and about 2.4 in passage 2. The results in the first passage are quite comparable to Ref. [76] (45 deg, in-line, parallel, P/e = 10, e/D_h = 0.078, sharp-edge, Re = 40k) and Ref. [78] (45 deg, staggered, parallel, P/e = 10, e/D_h = 0.1, sharp-edge, Re = 25k), even though the rib angles and profiles are different. It should be noted that the enhancement in regions 6 & 7 (turn portion) is the lowest due to the absence of ribs. Also, regions 5 and 8, i.e. $x1/D_{h1}$ = 5.6 and $x2/D_{h2}$ =2.3, which are only partially covered by ribs, have the second lowest Nus/Nu_0 values. Heat transfer on the inner and outer walls is augmented by the rib-induced secondary flows. In the high aspect ratio (AR = 4:1) passage 1, the rib-induced vortex pair may be arrested in its development due to limited channel height. However, the turbulence induced on the inner wall seems to be magnified, resulting in a higher heat transfer as compared to the outer wall. In passage 2 (AR = 2:1), the rib induced vortex pair is expected to be impinging on the outer wall, leading to a higher heat transfer than the inner wall. Remarkably, heat transfer on Tip-6 and Tip-7 is significantly reduced (Nu/Nus = 1.71 and 1.07) as compared to the smooth channel (Nu/Nu_s = 2.25 and 1.30). This reduction may be due to the reduced flow impingement that is caused by the rib-induced secondary flows.

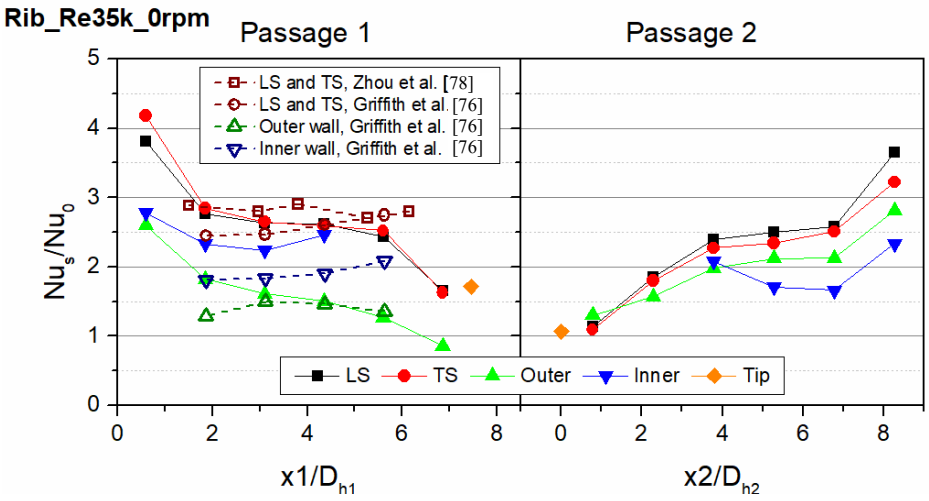

Figure 35 Ribbed surface streamwise Nu/Nu_0 ratio at Re = 35k under 0 rpm

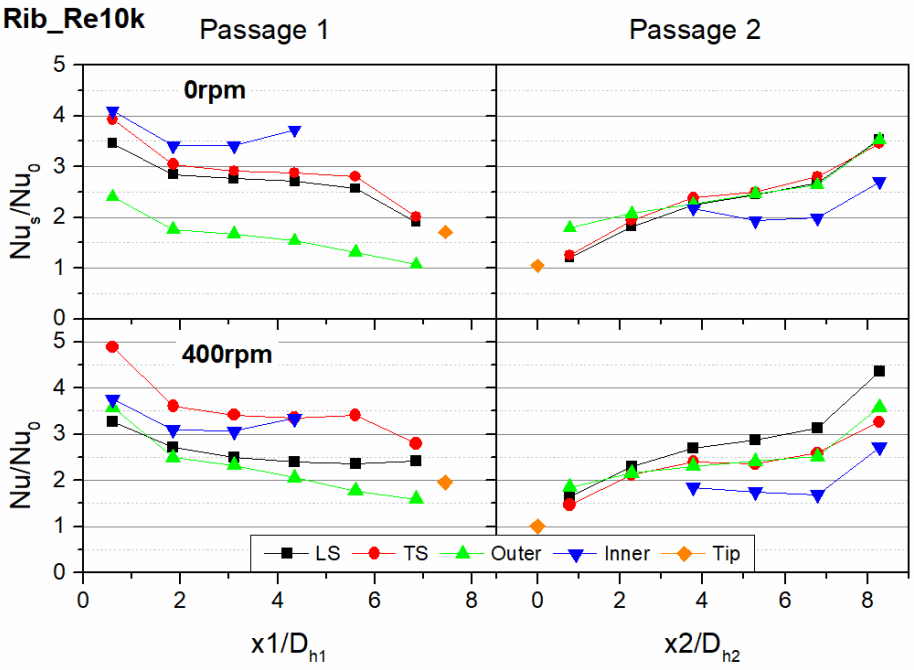

Figure 36 Ribbed surface streamwise Nu/Nu_0 ratio at Re = 10k under 0 and 400 rpm

Figure 36 shows the comparison of the streamwise Nu/Nu_0 distributions at Re = 10k under 0 and 400 rpm. For the stationary case, we can see the Reynolds number effect when compared to Figure 35. Interestingly, heat transfer enhancement on the inner wall is higher than the rib-roughened LS and TS in passage 1. This may be due to the higher turbulence induced near the inner wall than the LS and TS. In passage 2, heat transfer on the outer wall is comparable to the LS and TS. The flow impingement effect on the outer wall at $x2/D_{h2}$ =0.8 is more significant at this low Reynolds number than the case shown in Figure 35. These results demonstrate the dependence on Reynolds number, especially for inner and outer walls when ribs are present. Under rotation, we can see a general trend of increased heat transfer on the TS and outer wall and decreased heat transfer on both the LS and inner wall in passage 1. On the other hand, heat transfer is increased on the LS but decreased on the inner wall in passage 2. The effect of rotation seems to be small on the tip wall. In reality, there is a decreasing then increasing trend with Ro and this will be explained later.

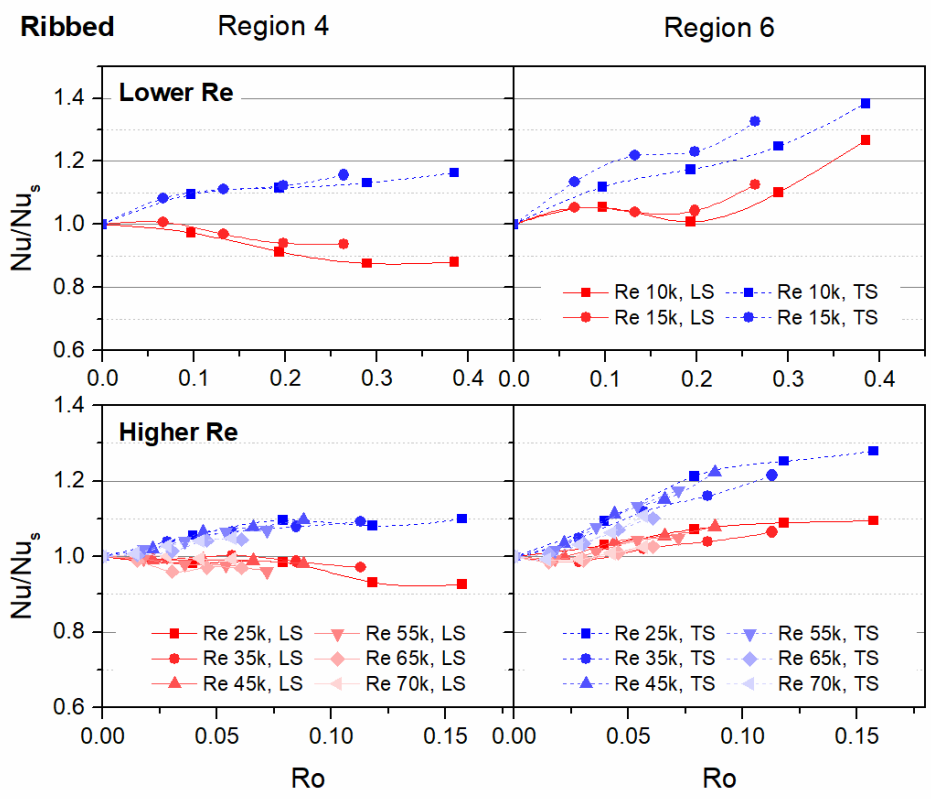

Figure 37 Effect of rotation number (Ro) on LS and TS heat transfer (Nu/Nu_s) in regions 4 and 6 for ribbed case

Figure 37 shows the rotation number effect on LS and TS heat transfer in regions 4 and 6 for the rib-roughened surface. The general trends in both regions are clear. In region 4, heat transfer increases with Ro with up to 16% on the TS. For the LS, Nu/Nus decreases with Ro with up to 12%. This behavior resembles the general trend found in the square channel Refs. [68-70]. In region 6, heat transfer increased on both LS (up to 27%) and TS (up to 38%). However, for the lower Re values the increasing trend on the LS is not monotonic and has a minimal value at Ro ≈ 0.2. This may be attributed to the enhanced vortical structures inside the ribbed channel under rotation that alters the local heat transfer.

There is some dependence on Re at lower Re of 10k and 15k, however, the data correlate well at higher Re between 25k and 70k, as seen at the bottom right corner of Figure 37.

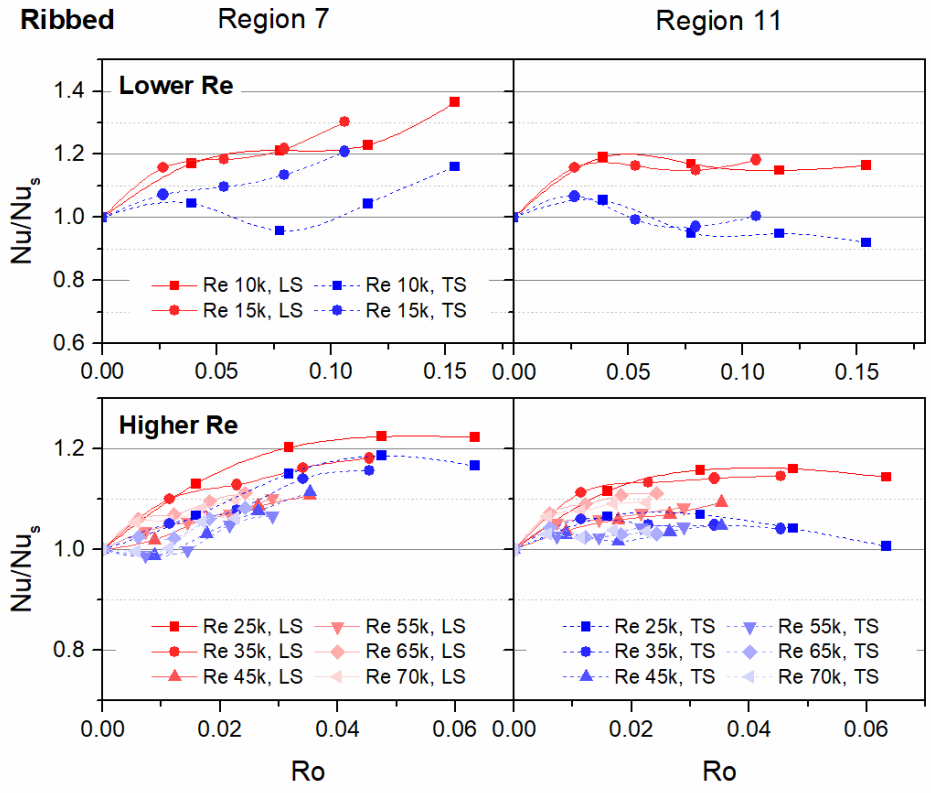

Figure 38 Effect of rotation number (Ro) on LS and TS heat transfer (Nu/Nu_s) in regions 7 and 11 for ribbed case

Heat transfer enhancement on the LS and TS in region 7 and 11 can be seen in Figure 38. In region 7, the results show an enhancement of up to 36 % and 16% for the LS and the TS, respectively. However, there is a strong Reynolds number dependence at Re = 10k and 15k on the TS. The increasing trend with some Reynolds number dependence is similar to region 6. It seems that the heat transfer on the LS and TS in the turn portion (both

regions 6 and 7) is more sensitive to the Reynolds number effect. Again, it may be attributed to the complicated flow structure associated with the combined effects of the rib-induced and turn-induced secondary flows. At more downstream in region 11, heat transfer enhancement on the LS can be seen for all Reynolds numbers. For Re = 10k and 15k, Nu/Nu_s remained at a level around 1.18 on the LS. For TS-11, the results show an increasing then decreasing trend for Ro = 0-0.075. The lowest Nu/Nus value found was 0.92 at the highest Ro and Re = 10k. There is a small dependence on the Reynolds number on the LS in both region 7 and 11. Nevertheless, the trend is consistent at all Reynolds numbers.

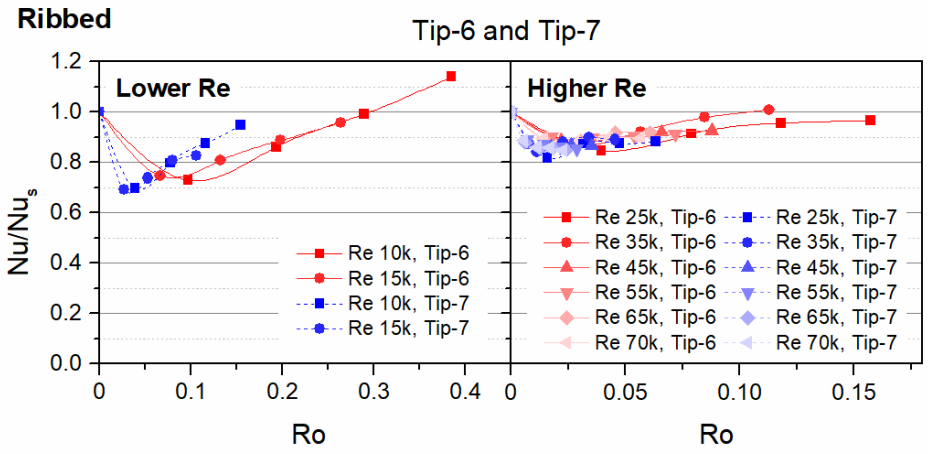

Figure 39 Effect of rotation number (Ro) on Tip wall heat transfer (Nu/Nu_s) in regions 6 and 7 for ribbed case

The effect of rotation on heat transfer in the regions Tip-6 and Tip-7 is shown in Figure 39. The Nusselt number ratio Nu/Nu_s shows a decreasing then increasing trend with rotation number for both regions. This trend is quite similar to the smooth surface, with a

smaller dependence on the Reynolds number. For region Tip-6, the lowest Nu/Nus value was 0.73 found at Ro = 0.1 and Re = 10k. The heat transfer then gradually increases up to Nu/Nu_s = 1.14 at higher Ro. For region Tip-7, the lowest Nu/Nu_s value of 0.69 is seen at Ro ≈ 0.03 and Re = 15k. Heat transfer then increases monotonically at higher Ro up to Nu/Nu_s = 0.95.

The overall effect of rotation on heat transfer for all the surfaces considered in the current study is compared and presented in Figure 40. For the smooth surface, significant heat transfer enhancement is seen on TS-4, LS-6, and TS-6 under rotation (46%-61%). Generally, heat transfer enhancement can be seen on both LS and TS in passage 1 under high rotation numbers (Ro > 0.27). Substantial heat transfer reduction, on the other hand, is seen on TS-11 (41%), Tip-6 (28%) and Tip-7 (36%). For the rib-roughened case, the rotation effect is reduced on most surfaces when rib-induced secondary flows come into the picture. Heat transfer enhancement can be seen on most surfaces under rotation. It is worthy to point out that the heat transfer on the tip wall (Tip-6 and Tip-7) reduced drastically with up to 31% for the two lower Reynolds number cases and lower rotation numbers (Ro = 0.1 for Tip-6 and 0.03 for Tip-7). These effects of rotation must be taken into consideration for the design of a gas turbine airfoil with similar internal cooling geometries and features.

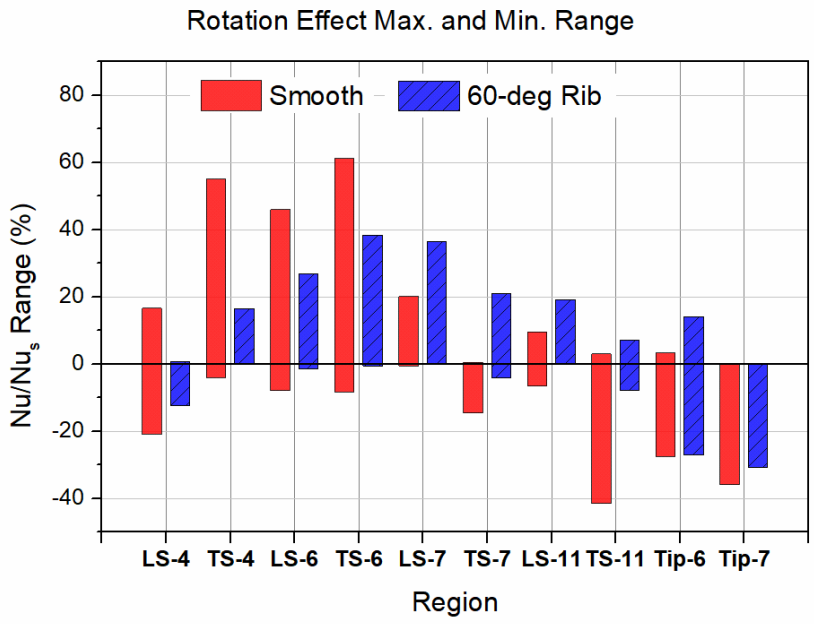

Figure 40 Comparison of the maximum and minimum Nu/Nu_s for all surfaces considered within the Re and Ro range

3.7.3 Conclusions – Smooth Surface and 60 deg Angled Ribs

The rotation effects on heat transfer and pressure loss coefficient have been investigated in a two-pass rectangular internal cooling channel featuring a reduced cross-sectional area and aspect ratio (AR= 4:1 to 2:1), after a 180 deg tip turn. A wide range of Reynolds number (10k to 70k) and rotation number (0 to 0.39) was considered. Both smooth surface (baseline case) and 60 deg rib-roughened surface are included. Regionally averaged heat transfer (copper plate) method was used. According to the results, the following conclusions can be made:

1. The size of the secondary flows that can be seen in the second pass near the 180 deg turn in a typical two-pass channel is significantly reduced due to flow

acceleration. The accelerating flow seems to increase the flow stability and reduce the turbulence level, resulting in a relatively low Nu/Nu0 downstream of the turn compared to a typical constant aspect ratio channel.

2. For smooth case in the first passage (regions 4 and 6), rotation enhanced HT on the TS (at Ro > 0.12) as expected. For LS-4, the results show a decreasing then increasing trend. For LS-6, HT generally increases with Ro at Ro > 0.13.
3. For smooth case in the second passage (regions 7 and 11), HT decreases with Ro on the TS. The rotation has a positive effect on LS-7. HT increases then decreases on LS-11.
4. For ribbed case in the first passage (regions 4 and 6), HT on the TS increases with Ro (up to 38%). In general, HT decreases on LS-4 but increases on LS-6 with Ro.
5. For ribbed case in the second passage, HT on both LS and TS generally increases with Ro in region 7. For LS-11, $Nu/Nu_s \approx 1.8$ for Ro > 0.03. For TS-11 HT first increases then decreases with Ro.
6. For both smooth and ribbed cases on the tip wall, HT shows a decreasing then increasing trend. The lowest Nu/Nu_s value found was around 0.7 at $Ro \leq 0.1$.
7. In general, rotation effects on heat transfer are reduced in the rib-roughened channel. Dependence on the Reynolds number can be seen for this particular internal cooling channel design, especially for the smooth case. More research is needed for channels with varying aspect ratios (converging or diverging at the 180 deg turn). And these geometrical effects should be taken into consideration in the internal cooling design.

3.8 Results and Discussion – 45 deg Angled Ribs with Rib Coverage Effect

Heat transfer results in terms of Nusselt number ratios will be presented for the three different rib configurations under stationary and rotating conditions. Reynolds number (Re) from 10k to 70k and rotation number (Ro) from 0 to 0.39 were covered. The heat transfer characteristics of three different rib configurations in an internal cooling channel featuring varying aspect ratio (AR = 4:1 to 2:1) and a converging 180 deg tip turn will be discussed. The rib configurations include 45 deg angled rib with less coverage (Config. 1), medium coverage (Config. 2), and full coverage (Config. 3). The results will be presented in the following order: Temperature distribution, Nusselt number distribution, rotation effects on heat transfer. The pressure loss coefficient will be presented in section 3.9.

3.8.1 Temperature Distribution

Temperature distributions of Config. 2 at an intermediate Reynolds number of Re = 35k at both the lowest and highest rotational speeds are selected for demonstration, as shown in Figure 41. All temperatures are normalized by the inlet temperature $T_{b,inlet}$. The temperatures of the LS, TS, outer surface and inner surface are kept at around $T/T_{b,inlet}$ = 1.10. The temperatures of the nearby surfaces at a certain region are kept at a similar level in order to reduce the heat conduction error, as discussed in the experimental section. The temperatures at the inlet $x1/D_{h1}$ = 0.6 and outlet $x2/D_{h2}$ = 8.3 are slightly lower due to the higher conduction heat loss to the adjacent test section material. In the turn portion $x1/D_{h1}$ = 6.9 and $x2/D_{h2}$ = 0.8, the temperatures are significantly higher on the LS, TS, and the outer wall due to the absence of the ribs. For the 0 rpm case, the $T/T_{b,inlet}$ values go up to

1.13 to 1.16 in the turn portion. For the Tip-6 ($x1/D_{h1} = 7.5$) and Tip-7 ($x2/D_{h2} = 0$) surfaces, the power of the heater is controlled so that the temperatures are fairly close to the adjacent surfaces at $T/T_{b,inlet} \approx 1.15$. Bulk fluid temperatures derived by means of linear interpolation of the measured inlet and outlet temperatures ($T_{b,inter}$) and the energy balance method ($T_{b,energy}$) are also provided. The $T_{b,energy}$ at the channel outlet is forced to be identical to the measured value due to the assumptions made for the heat loss analysis. The results are generally in good agreement except for a small deviation (≈ 0.4%) near the turn portion. For the 400 rpm case, the temperature distributions are pretty similar to the 0 rpm case. However, the power input of individual heaters are adjusted in order to control the temperatures of different surfaces at a similar level.

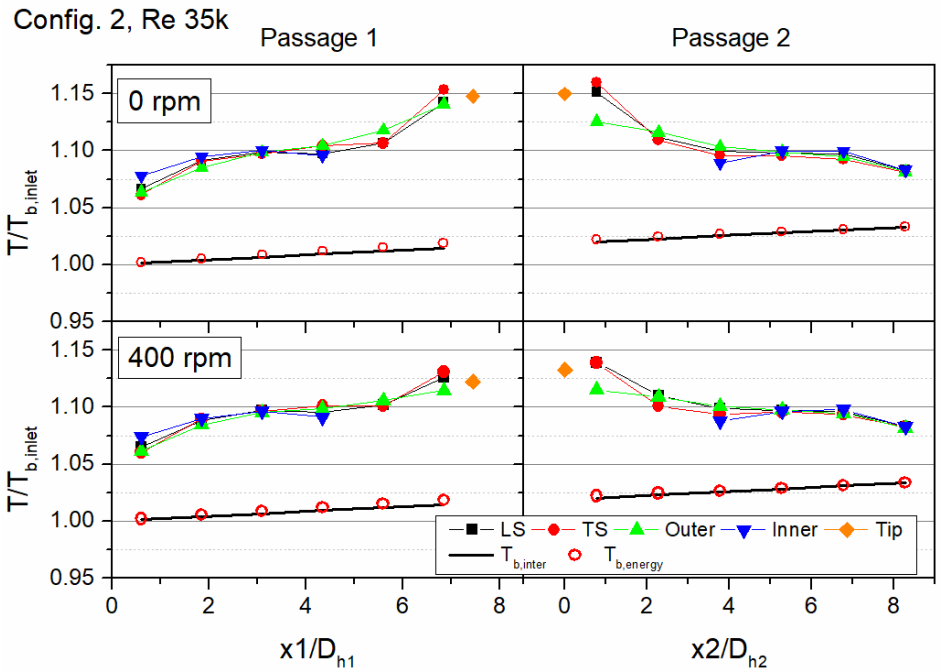

Figure 41 Temperature distribution for Config. 2 at Re = 35k, 0 and 400 rpm

3.8.2 Nusselt Number Distribution

Stationary normalized Nusselt number Nu_s/Nu_0 distributions for the three configurations at Re = 10k are presented in Figure 42. Please note that the reference Nusselt number Nu_0 is based on each passage. From this figure, we can see clearly that the rib coverage near the tip turn portion alters the heat transfer results considerably. The general trend on the LS and TS heat transfer of a typical internal cooling channel is found to be decreasing from the inlet due to the developing thermal and momentum boundary layers. The Nusselt number ratio then gradually converges to a certain number further downstream as can be seen in the previous section 3.7. A similar trend can be expected in the 45 deg angled rib roughened channels. A general decreasing trend can be seen in the first passage for all configurations on all surfaces (except the inner surface for Config. 2 and Config. 3). Heat transfer on the LS and TS is higher than the inner and outer surfaces due to the rib turbulators. Heat transfer on the inner surface is higher than the outer surface due to the stronger rib-induced turbulence near the inner wall, as expected.

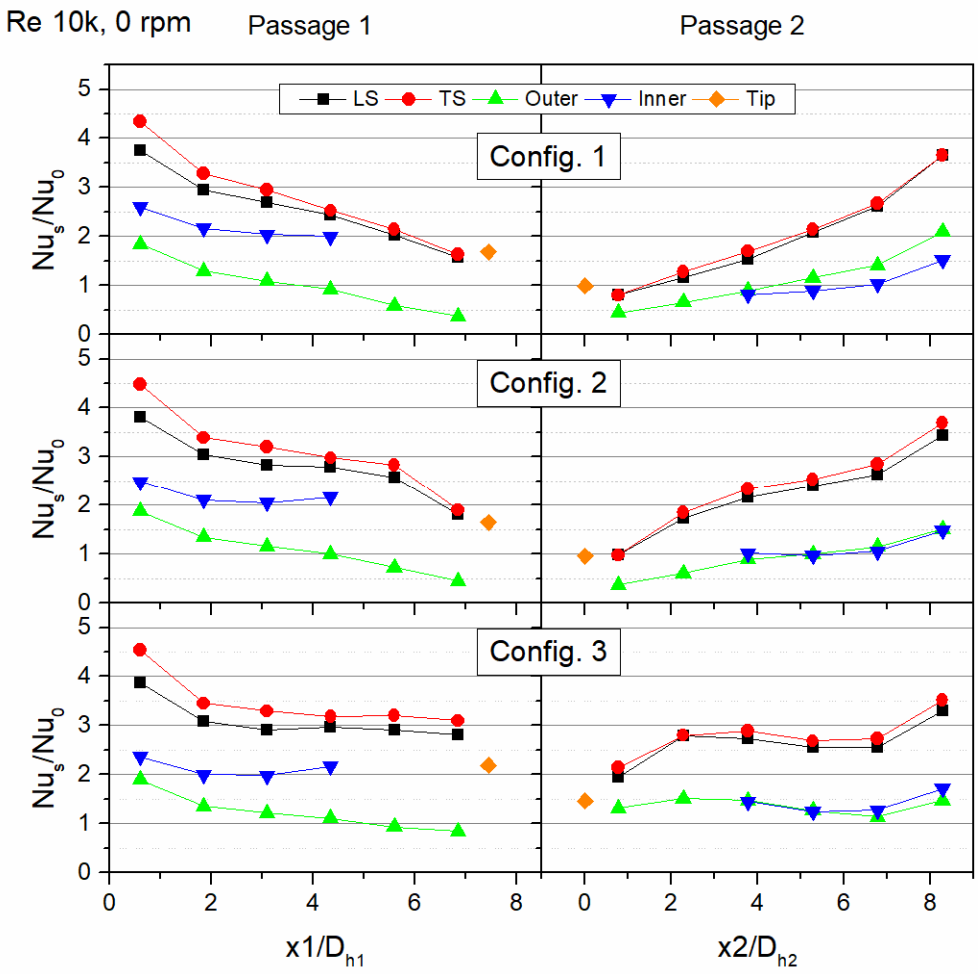

Figure 42 Stationary Nu_s/Nu_0 distribution at Re = 10k

For Config. 1, regions 4 ($x1/D_{h1}$ = 4.4), 5 ($x1/D_{h1}$ = 5.6) and 9 ($x2/D_{h2}$ = 3.8) are only partially covered by ribs (Figure 27). As a result, the Nu_s/Nu_0 ratio on the LS and TS gradually decreases from the inlet to the tip turn in passage 1 and gradually increases from the tip turn to the outlet in passage 2. The Nusselt number ratios are around Nu_s/Nu_0 = 4 to 1.6 in passage 1 and Nu_s/Nu_0 = 0.8 to 3.7 in passage 2. In passage 1, the Nusselt number ratio on the inner surface is around Nu_s/Nu_0 = 2. The Nusselt number ratio on the outer

surface gradually decreases from Nu_s/Nu_0 = 1.9 to 0.4 and is lower than the inner surface. A significant heat transfer reduction on the outer surface is seen near the turn portion $x1/D_{h1}$ = 4.4 to 6.9. In passage 2, heat transfer reduction is also seen on the outer surface near the turn with Nu_s/Nu_0 = 0.4 at $x2/D_{h2}$ = 0.8 and Nu_s/Nu_0 = 0.9 at $x2/D_{h2}$ = 3.8. The results suggest that the rib-induced secondary flows continue to affect the heat transfer downstream of the rib turbulators, even after the tip turn. It seems that the flow impingement effect on the outer surface in region 7 is reduced. Heat transfer is slightly higher on the outer surface than the inner surface at further downstream $x2/D_{h2}$ = 3.8 to 8.3 in passage 2. The Nu_s/Nu_0 ratios of the inner and outer surfaces are around 0.85 at $x2/D_{h2}$ = 3.8 and gradually increase to 1.5-2.1 at the outlet $x2/D_{h2}$ = 8.3. Heat transfer on the tip surface in passage 1 (Tip-6, $x1/D_{h1}$ = 7.5) is enhanced to Nu_s/Nu_0 = 1.7 due to the flow impingement. However, heat transfer on the tip surface in passage 2 (Tip-7, $x2/D_{h2}$ = 0) remains at Nu_s/Nu_0 = 1.

For Config. 2, heat transfer enhancement on the LS and TS remains at around Nu_s/Nu_0 = 3 with a slight decrease from region 2 to 5, $x1/D_{h1}$ = 1.9 to 5.6. Then the Nusselt number ratio drops to around Nu_s/Nu_0 = 1.9 in the turn portion at $x1/D_{h1}$ = 6.9, where there is no rib coverage. In the second pass, the addition of 2 more ribs near the turn enhances the heat transfer at $x2/D_{h2}$ = 2.3, 3.8, and 5.3 (regions 8, 9, and 10) by around 45%, 37%, and 22%, respectively as compared to Config. 1. Heat transfer on the inner, outer and tip surfaces remains at a similar level as in Config. 1, except for the slight decrease on the outer surface in the downstream part of the second passage.

For Config. 3, heat transfer is generally enhanced than the previous two configurations with a full rib coverage design. The Nusselt number ratios on the LS and

TS remain at around $Nu_s/Nu_0 = 3.1$ in the first passage (except for region1). Compared to Config. 2, the additional ribs in the tip turn portion significantly enhanced the heat transfer on all surfaces (LS, TS, outer, inner and tip) in and after the turn from region 6 to region 10 ($x1/D_{h1} = 6.9$ to $x2/D_{h2} = 5.3$). Furthermore, the streamwise variation in Nusselt number ratio is reduced in both passages, especially for the LS and TS. There is a small difference (maximum ≈ 12%, disregarding region 1) between the LS and TS data. It may be originated from the slightly mismatch of the parallel ribs due to human error involved in the installation process. Nevertheless, this effect would not affect the rotation effect results, which are presented by the Nusselt number under rotation divided by the stationary Nusselt number, i.e. Nu/Nu_s.

The normalized Nusselt number distributions at the highest rotational speed of 400 rpm are shown in Figure 43. At the lowest Reynolds number of Re = 10k, this specific case gives the highest rotation number of Ro = 0.39. The rotation effects on each surface can be seen when compared to Figure 42. In general, heat transfer is enhanced on all surfaces except for the LS in passage 1. In the second passage, significant heat transfer enhancement can be seen on all surfaces near the turn ($x2/D_{h2} = 0$ to 2.3) for Config. 1 and Config. 2. For Config. 3, slight heat transfer enhancement is also seen at $x2/D_{h2} = 0$ to 0.8 on all surfaces. Heat transfer on the LS is enhanced along passage 2 for all three configurations.

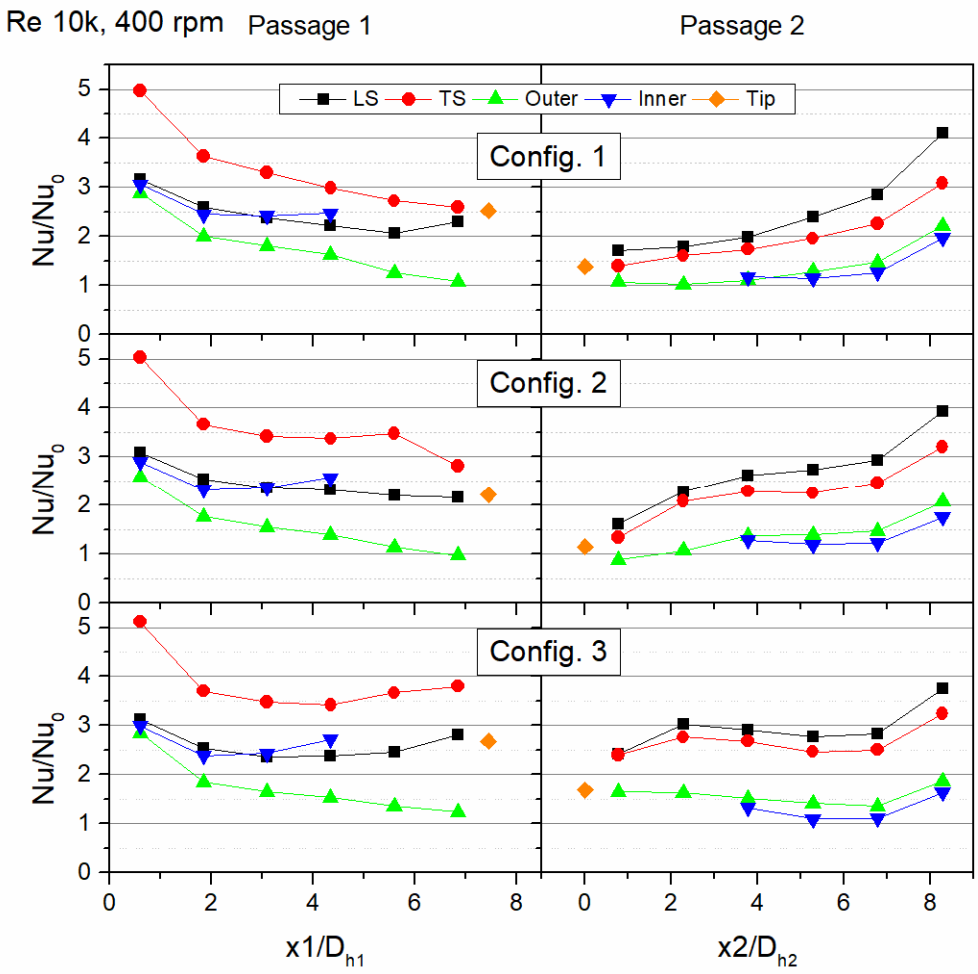

Figure 43 Nu/Nu_0 distribution at Re = 10k and 400 rpm

3.8.3 Rotation Effects on Heat Transfer

The rotation effects on heat transfer will be discussed for several representative regions, including the LS and TS of regions 4, 6, 7, 11, and the tip surfaces (Tip-6 and Tip-7). An overall comparison of the rotation effect on heat transfer of the three configurations will be made at the end of this section.

The effect of rotation on heat transfer on the LS and TS in region 4 is compared and presented in Figure 44. Region 4 is located right before the turning portion, where the flow is closer to fully developed flow. As in a typical AR = 1:1 or 2:1 channel, an enhancement on the TS and reduction on the LS can be expected. Please note that for Config. 1, region 4 is only partially covered by ribs. However, the rib coverages in region 4 are the same for Config. 2 and Config. 3. In this figure, the data obtained at lower Reynolds numbers Re = 10k and 15k are separated from the data obtained at higher Reynolds numbers Re = 25k-70k for an improved legibility. For Config. 1, we can see a maximum heat transfer enhancement of 17.5% on the TS and a maximum reduction of 9.4% on the LS for the lowest Reynolds number Re = 10k at the highest rotation number Ro = 0.39. This trend is consistent with all the previously published data. The effects are majorly due to the rotation induced secondary flow, which is a Coriolis force induced vortex pair that impinges on the TS. When this vortex pair forms, the heat transfer on the opposite stabilized surface (LS) will be reduced. A small Reynolds number dependence can be seen when comparing the lower Re and higher Re cases. In general, it seems that the rotation effect is reduced at higher Reynolds numbers.

For Config. 2, the rotation effect is reduced on the TS but augmented on the LS as compared to Config. 1. The maximum Nusselt number ratio obtained was $Nu/Nu_s = 1.13$ on the TS while a minimum of $Nu/Nu_s = 0.83$ was obtained on the LS at the highest Ro = 0.39. There is approximately a 4% reduction on the TS and a 9% reduction on the LS when compared to the Config. 1, owing to the additional rib near the inner wall in region 4. The rotation effects on heat transfer are very similar for Config. 2 and Config. 3 as expected, except for a peculiar point on the TS at Ro = 0.1 and Re = 10k. However, the uncertainty

at the lower Reynolds numbers are known to be high. Consequently, the result is still considered reasonable. The general trend of heat transfer enhancement on the TS and reduction on the LS in a radial outward flow remains the same for the three configurations.

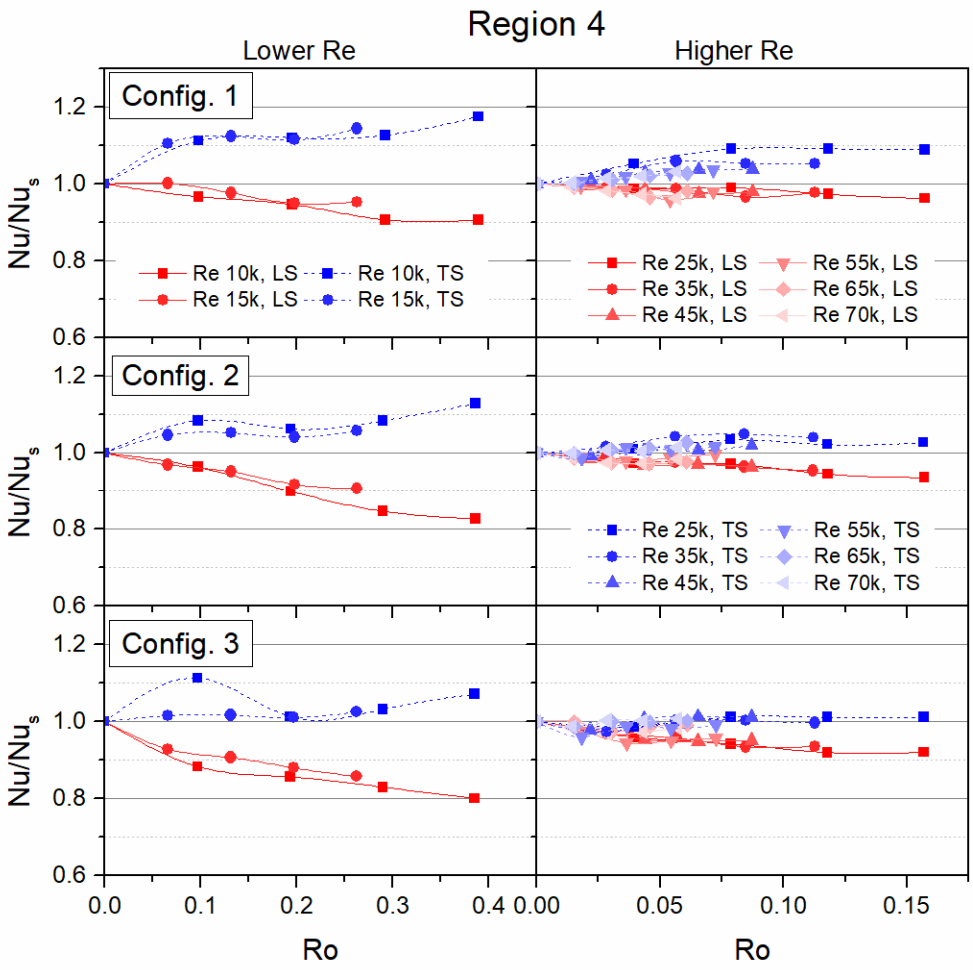

Figure 44 Effect of rotation number (Ro) on LS and TS heat transfer (Nu/Nu$_s$) in region 4

Figure 45 shows the rotation number effect on LS and TS heat transfer in region 6, which is adjacent to the tip surface in the first passage. The rib coverages upstream of region 6 are different for the three different configurations. As a result, different rotation effects on heat transfer can be expected. For Config. 1, the most notable difference from region 4 is that the heat transfer is enhanced on both the LS and the TS under rotation. The rotation and rib induced complex vortical flows in this turn region may be responsible for the enhanced heat transfer. The Nusselt number ratios are found to be as high as Nu/Nu_s = 1.58 on the TS and Nu/Nu_s = 1.45 on the LS at Ro = 0.39. The data at higher Reynolds numbers correlate well on both surfaces and show an increasing trend with Ro up to Nu/Nu_s = 1.30 on the TS and Nu/Nu_s = 1.15 on the LS at Ro = 0.16.

For Config. 2, the rotation effect is reduced as compared to Config. 1. The Nusselt number ratio reduced to Nu/Nu_s = 1.48 on the TS and Nu/Nu_s = 1.19 on the LS at Ro = 0.39. The data at higher Reynolds numbers correlate well with an increasing trend up to $Nu/Nu_s \approx 1.21$ on the TS at Ro = 1.11-1.16 and $Nu/Nu_s \approx 1.10$ on the LS at Ro = 0.07-0.16. For Config. 3, the rotation effect becomes negative on the LS. The rib-induced secondary flows become more dominant in this case. The growth of the rotation-induced secondary flows is restricted by the presence of the additional ribs. The heat transfer enhancement is also reduced to Nu/Nu_s = 1.22 at Ro = 0.39 on the TS. A minimum Nusselt number ratio of Nu/Nu_s = 0.91 is found on the LS at Ro = 0.19. The correlations at higher Reynolds numbers are almost linear and close to unity, with a highest enhancement of 5.6% on the TS at Ro = 0.16. This indicates that the additional ribs near the turn portion in passage 1 have a negative impact on heat transfer enhancement under rotation. On the other hand, similar to region 4, the Nusselt number ratios are generally higher on the TS than the LS.

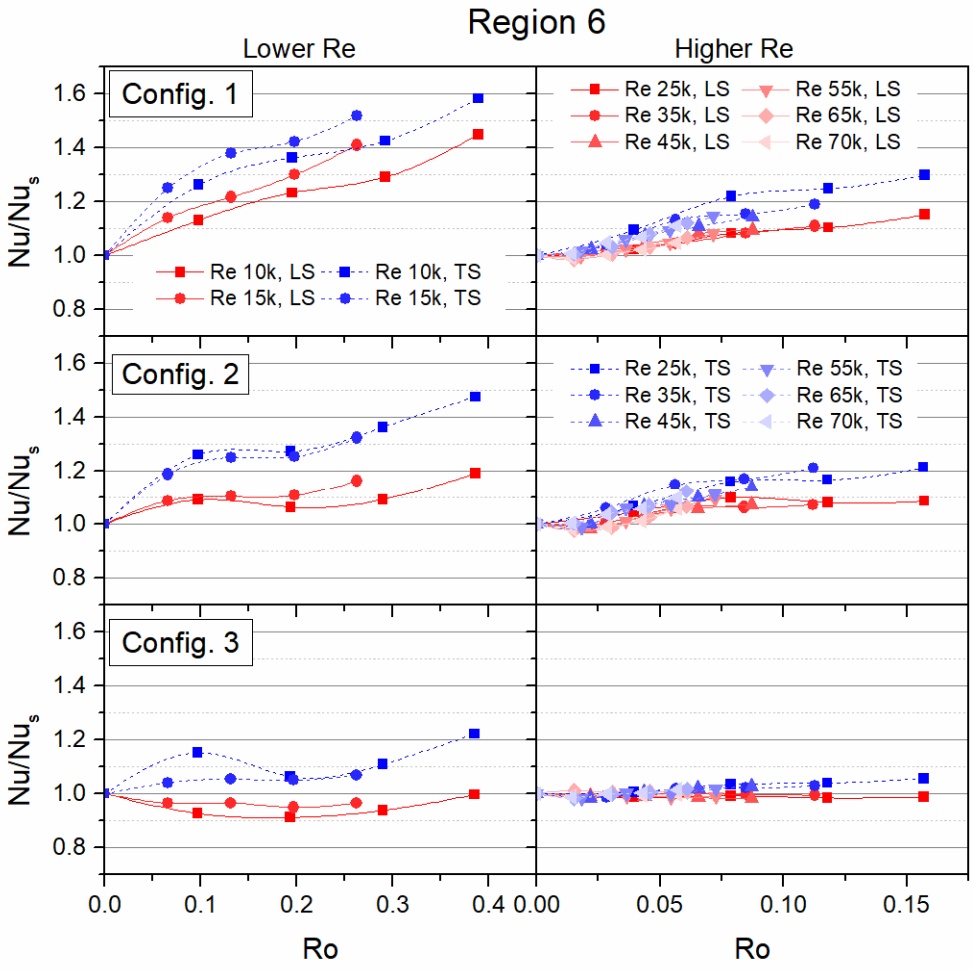

Figure 45 Effect of rotation number (Ro) on LS and TS heat transfer (Nu/Nu_s) in region 6

The effect of rotation number on heat transfer in region 7 is shown in Figure 46. The most prominent difference between the results in the first passage may be that the Nusselt number ratios on the LS become higher than the TS for most of the data points. The results show different degrees of heat transfer enhancement on both the LS and TS for the three configurations under rotation. Heat transfer enhancement on the LS and TS is the highest for Config. 1, reaching $Nu/Nu_s = 2.10$ on the LS and $Nu/Nu_s = 1.75$ on the TS at Ro = 0.156. Given the relatively lower Ro than the first passage, this level of enhancement is quite remarkable. The higher Reynolds number cases also correlate better than the lower Reynolds number cases. The Nusselt number ratio approaches $Nu/Nu_s \approx 1.5\text{-}1.6$ at Ro = 0.063 for both surfaces.

For Config. 2, the effect of rotation is reduced. The highest values are lowered to $Nu/Nu_s = 1.65$ and 1.37 at Ro = 0.154 for the LS and TS, respectively. The Reynolds number effect is more apparent between Re = 10k and 15k on the TS, nevertheless, the data also correlate well at higher Reynolds numbers and show an increasing trend up to $Nu/Nu_s = 1.32$ at Ro = 0.063 for both surfaces. For the full rib coverage case, the effect of rotation is further reduced, with a highest $Nu/Nu_s = 1.24$ at Ro = 0.153. The heat transfer enhancement remains at around 8-12% for the LS at Ro = 0.026-0.104. The enhancement on the TS is always lower than the LS. The results also show a weakened rotation number effect with increasing rib coverages near the turn portion. It is worthy to note that the 45 deg angled ribs upstream of region 7 seems to create a constructive interaction of the rib and rotation induced secondary flows, leading to a purely positive effect on heat transfer under rotation.

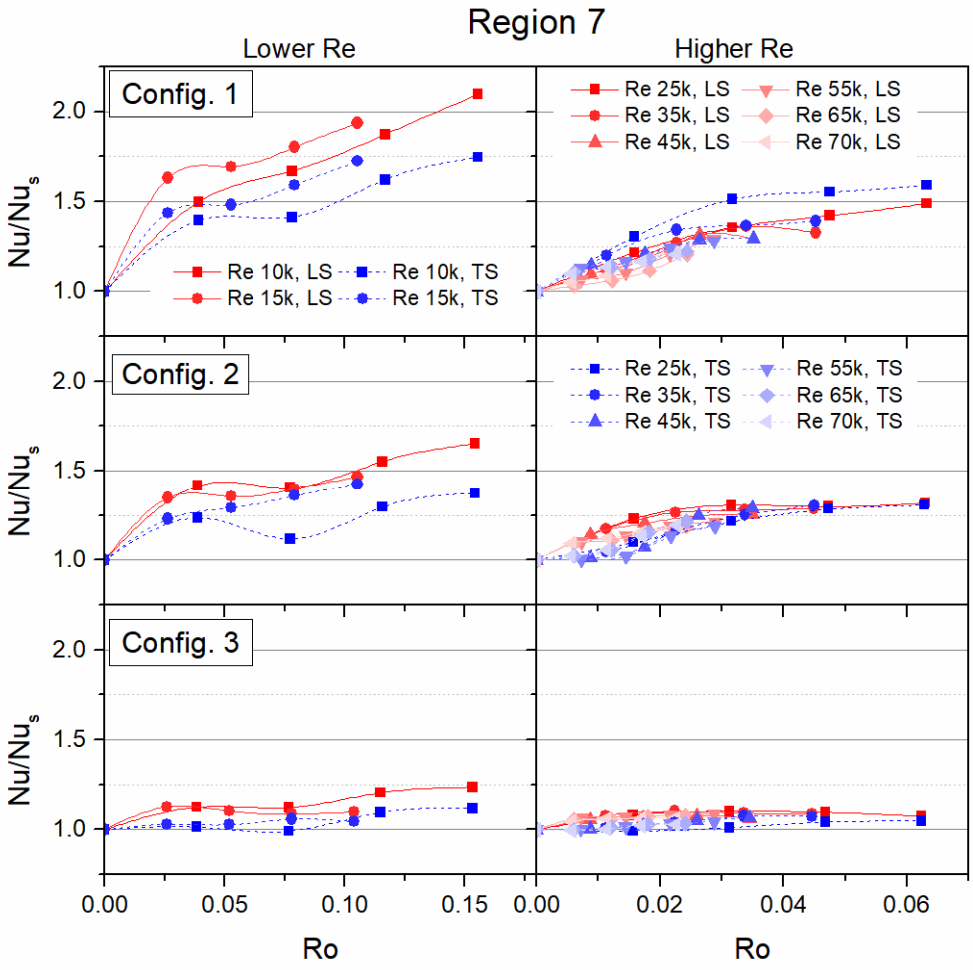

Figure 46 Effect of rotation number (Ro) on LS and TS heat transfer (Nu/Nu_s) in region 7

At further downstream in region 11 ($x2/D_{h2} = 6.8$), although the local rib coverages are the same for the three configurations, the effects from the upstream rib coverage differences can be seen in this region. The results are shown in Figure 47. At lower Reynolds numbers, a positive effect on the LS and a negative effect on the TS were observed (except for a small positive effect on the TS at $Ro < 0.05$). This trend is consistent with the results found in many previous studies with a radial inward flow. It is a result of the Coriolis force induced vortex pair that impinges on the LS. For the LS, the Reynolds number effect seems to be more apparent in Config. 1. The Nusselt number ratio first increases up to $Nu/Nu_s = 1.2$ at $Ro = 0.026$ then gradually decreases down to $Nu/Nu_s = 1.09$ at $Ro = 0.156$. For higher Reynolds number cases, Nu/Nu_s first increases then gradually level out within the range $Nu/Nu_s = 1.08$-1.16. For the TS, there is a small positive effect when $Ro < 0.03$-0.05, then the effect turns negative. The lowest value is $Nu/Nu_s = 0.84$ at $Ro = 0.156$.

The rotation effect on heat transfer is quite similar for the three configurations in region 11 as expected. As the rib configuration changes from Config. 1 to Config. 2 and Config. 3, there are several observable trends. Firstly, the Reynolds number dependence on the LS is diminishing. Secondly, the rotation effect is slightly reducing on both LS and TS, meaning the minimum and maximum values are closer to unity. Thirdly, the decreasing trend is gone on the TS at higher Reynolds numbers for the Config. 3 (lower right of Figure 47).

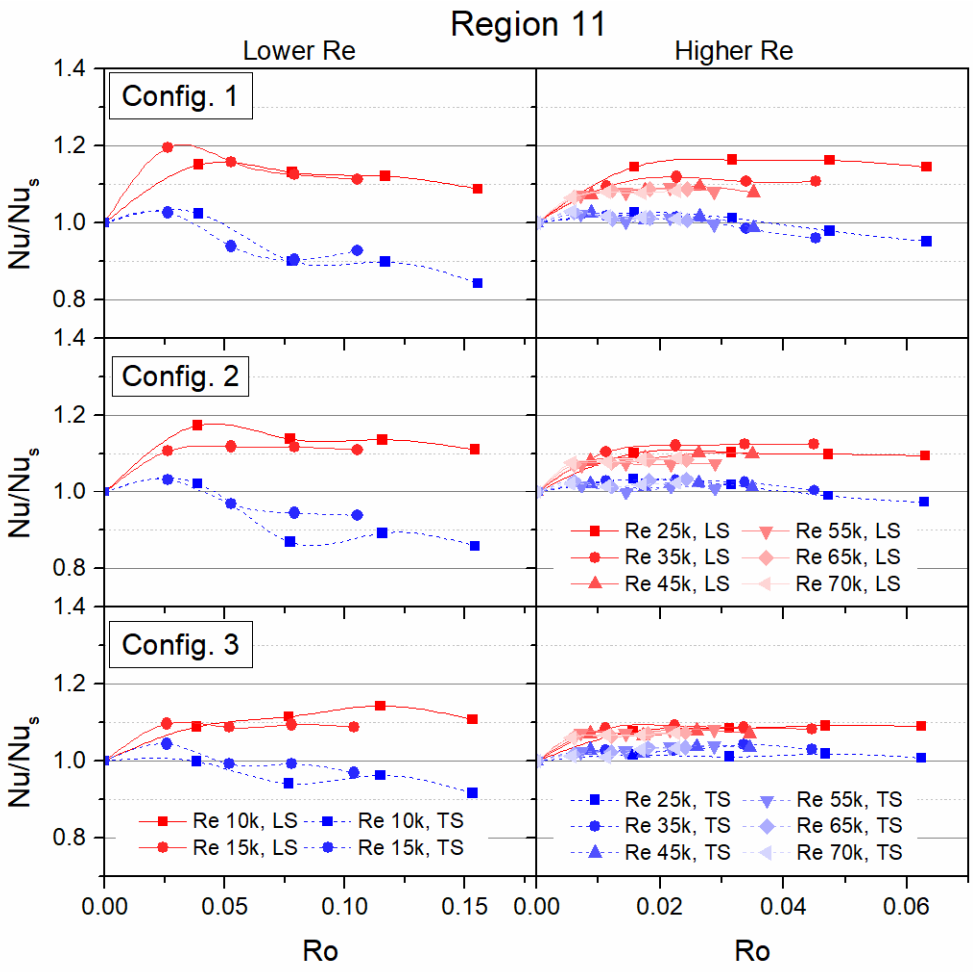

Figure 47 Effect of rotation number (Ro) on LS and TS heat transfer (Nu/Nu_s) in region 11

The effect of rotation on heat transfer in regions Tip-6 and Tip-7 is shown in Figure 48. The Nusselt number ratio Nu/Nus shows a decreasing then increasing trend with rotation number for both regions. Similar to earlier discussions, the number of ribs (or an increase of rib coverage) generally reduces the Reynolds number dependence and the rotation effect. The highest Nusselt number ratio on Tip-6 reduced from $Nu/Nu_s = 1.48$ to 1.34 and 1.22, for Config. 1 to Config. 2 and Config. 3. A similar trend is found on Tip-7, where the values drop from $Nu/Nu_s = 1.39$ to 1.19 and 1.15 for Config. 1 to Config. 2 and Config. 3. The lowest Nusselt number ratio occurs at Ro = 0.1 for Tip-6 and Ro = 0.04 for Tip-7. The lowest values are around $Nu/Nu_s = 0.75$ for Config. 1 and Config. 2 and are around $Nu/Nu_s = 0.83$ for Config. 3. The results suggest that extra care should be taken on the tip surface at lower rotation numbers.

Unlike the traditional constant cross-section and constant aspect ratio channel, the converging tip turn of the current design affects the heat transfer characteristics not only at the downstream of the turn in passage 2 but also dramatically changes the heat transfer on the tip surfaces under rotation. From the available literature and test data, the tip surface heat transfer is always elevated under rotation in a constant AR and cross-section channel due to the so-called pumping effect. The decreasing then increasing trend with rotation number is first observed and reported for this test section design with a converging tip turn (AR = 4:1 to 2:1). It is believed that the flow impingement on the tip surfaces in an accelerating flow in the turn portion is greatly reduced under rotation (at lower rotation numbers). The momentum of the fluid core toward the tip surface may be reduced due to the development and strengthening of the rotation induced vortices. This information is hence critical in the internal cooling design for a channel with a comparable design.

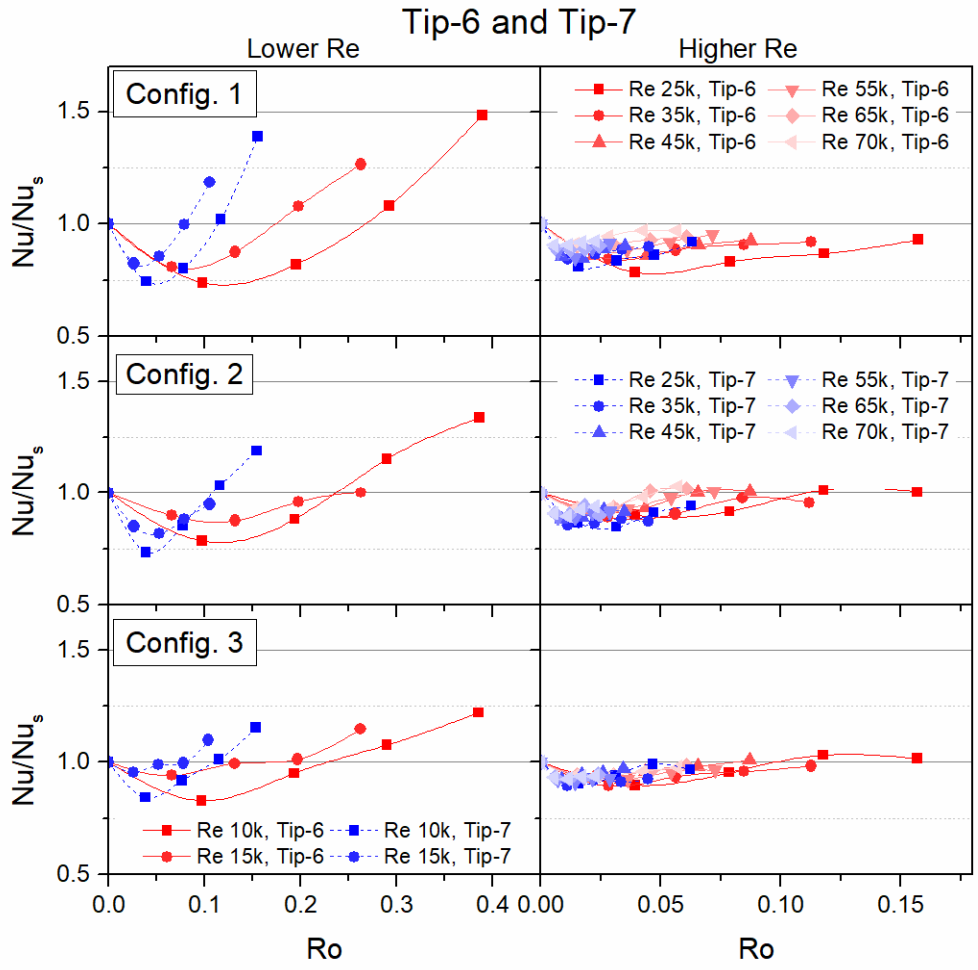

Figure 48 Effect of rotation number (Ro) on tip surface heat transfer (Nu/Nu_s) in regions 6 and 7 (Tip-6 and Tip-7)

The overall effect of rotation on heat transfer for all the surfaces considered in the current study is compared and presented in Figure 49. The results show heat transfer enhancement in most of the regions under rotation. Some negative effects up to 20% can be seen in regions LS-4 and TS-11. In general, the additional rib coverage in or near the turn portion greatly reduces the rotation effect on heat transfer, except for the LS-4 and TS-4. It is worthy to point out that the heat transfer on the tip wall (Tip-6 and Tip-7) reduced

drastically with up to 27% for the lower Reynolds number cases at lower rotation numbers (Ro = 0.1 for Tip-6 and 0.04 for Tip-7). These effects of rotation must be taken into consideration for the design of a gas turbine airfoil with similar internal cooling geometries and features.

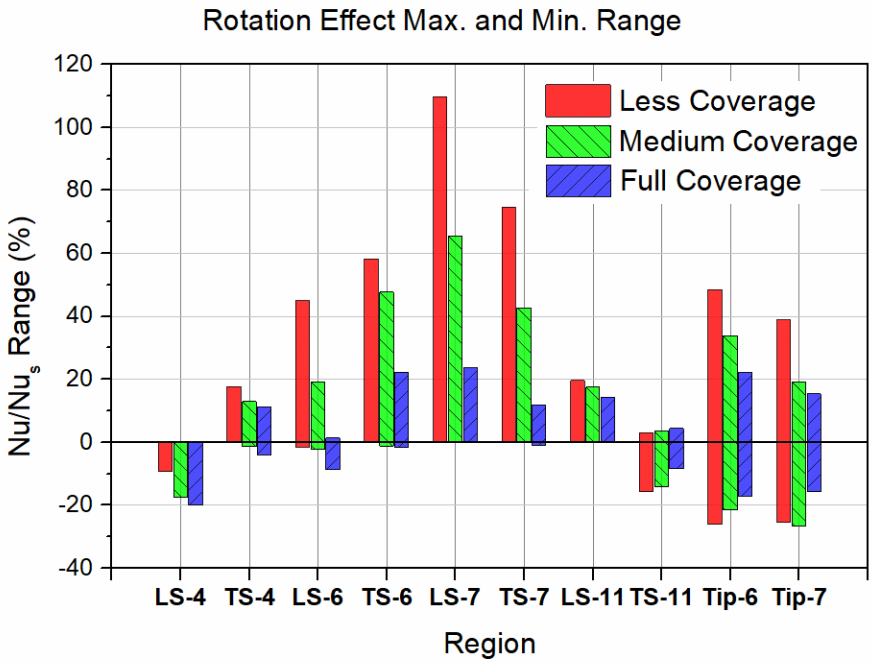

Figure 49 Comparison of the maximum and minimum Nu/Nu$_s$ for all surfaces considered within the Re and Ro range

3.8.4 Conclusions – 45 deg Angled Ribs with Rib Coverage Effect

The rotation effects on heat transfer and pressure loss coefficient have been investigated in a two-pass rectangular internal cooling channel featuring a reduced cross-sectional area and aspect ratio (AR= 4:1 to 2:1), after a 180 deg tip turn. A wide range of Reynolds number (10k to 70k) and rotation number (0 to 0.39) was considered. 45 deg

angled ribs are implemented on the LS and TS with three different rib coverages near the tip turn portion. Regionally averaged heat transfer (copper plate) method was used. According to the results, the following conclusions can be made:

1. There is small differences in the rotation effects on heat transfer among the three configurations in regions 4 and 11, which are located upstream of the turn and far downstream after the turn, respectively. The rotation effect is generally positive in TS-4 and LS-11 with up to +20% increment and negative in LS-4 and TS-11 with up to -20% decrement.
2. Under rotation, heat transfer is enhanced in general in region 6 up to 58% except for LS-6 for the Config. 3 where a minimum $Nu/Nu_s = 0.91$ was observed. The enhancement on the TS is higher than the LS at a fixed Ro.
3. Great heat transfer enhancement on both the LS and the TS up to 110% is seen in region 7 under rotation. Unlike in region 6, the enhancement on the LS is higher than the TS at a fixed Ro.
4. Heat transfer on the tip surface (Tip-6 and Tip-7) first decreases then increases with increasing Ro for all configurations. The minimum Nusselt number ratio is $Nu/Nu_s = 0.73$ at Ro = 0.04-0.1 while the maximum is $Nu/Nu_s = 1.48$ at Ro = 0.39. This behavior is quite different than a constant aspect ratio channel and is a result of the converging tip turn.
5. In general, rotation effects on heat transfer are reduced with an increased rib coverage. Different rib coverages near the tip turn significantly change the heat transfer and pressure drop in and after the turn. Dependence on the Reynolds number can be seen for this particular internal cooling channel design. The

combined geometrical and rib coverage effects should be taken into consideration in the internal cooling design.

3.9 Results and Discussion – Pressure Loss Coefficient

High accuracy pressure loss coefficients under both stationary (K_s) and rotating (K_r) conditions were obtained for five different configurations including the smooth surface case. The stationary results are presented in Figure 50. The horizontal axis is the average Reynolds number ($Re_{,ave}$) of the two passages. The loss coefficients are generally higher at lower Reynolds numbers as expected. The loss coefficients for the smooth wall case are around 1.9 to 2.3. The 45 deg – full coverage case has the highest pressure loss, followed by the 60 deg rib case, then the 45 deg – medium coverage and the 45 deg – less coverage cases. The average loss coefficient over the Reynolds numbers studied are summarized in Table 6. The ratios of the $K_{s,ave}$ to the smooth wall case are also provided. The highest loss coefficient seen in the 45 deg – full coverage case is around 4.3 times of the smooth case. Comparing the 45 deg – full coverage to the 45 deg – medium coverage, there is a nearly 40% increase in pressure loss coefficient due to the additional rib coverage in the turn region.

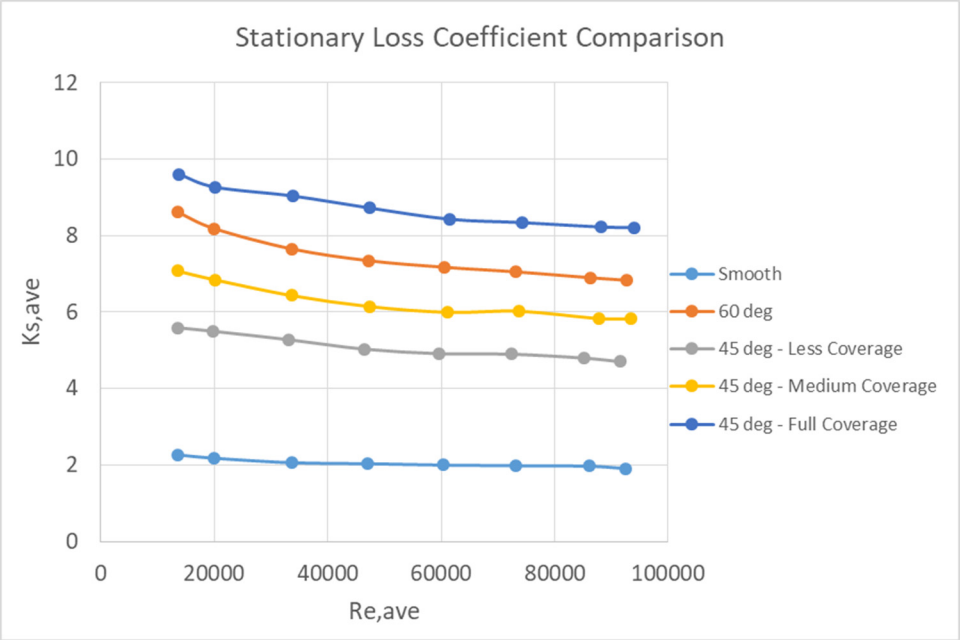

Figure 50 Stationary pressure loss coefficient comparison for five different configurations

Table 6 Static pressure loss coefficient comparison

	Smooth	60 deg	45deg Less Coverage	45deg Medium Coverage	45deg Full Coverage
$K_{s,ave}$	2.05	7.47	5.09	6.27	8.73
Ratio to the smooth case	1	3.6	2.5	3.1	4.3

Effects of rotation on the pressure loss coefficient on both the LS and TS for five different configurations are shown in Figure 51. The horizontal axis is the average rotation number ($Ro_{,ave}$) of the two passages. It is very interesting to see not only the rotation effect on heat transfer, but also the rotation effect on pressure loss coefficient over a wide range of rotation numbers. For the smooth case, the loss coefficient ratio (K_r/K_s) on the TS generally increases with increasing rotation number up to $K_r/K_s = 1.27$. A reverse trend was found on the LS where the values are reduced with a minimum of $K_r/K_s = 0.8$. The results indicate that the overall (average of the LS and TS) loss coefficient remains close to unity under rotation. For the 60 deg ribbed case, K_r/K_s decreases with increasing Ro for both leading and trailing surfaces with a minimum of $K_r/K_s = 0.79$ for the LS at the highest average rotation number of $Ro_{,ave} = 0.28$. This is dramatically different than the smooth case. The results suggest that for the 60 deg ribbed case, the overall pressure loss may be reduced under high rotation numbers. It may be a consequence of reduced energy dissipation of the rib-induced vortical structures under high rotation numbers.

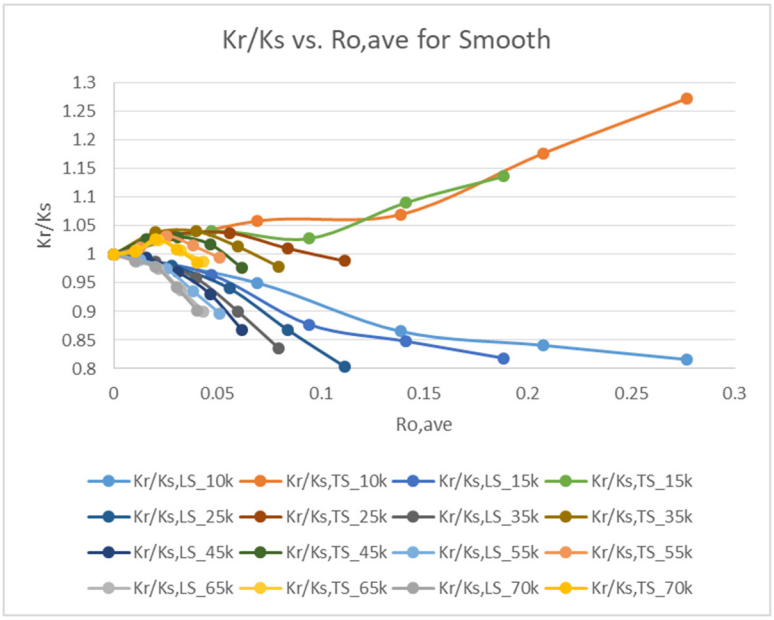

(a)

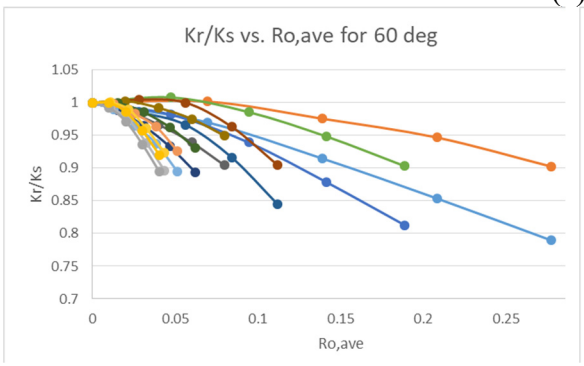

(b)

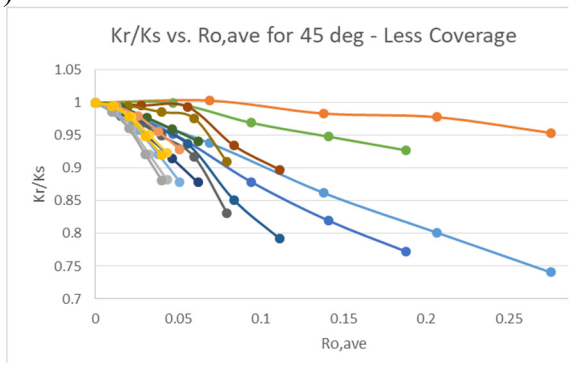

(c)

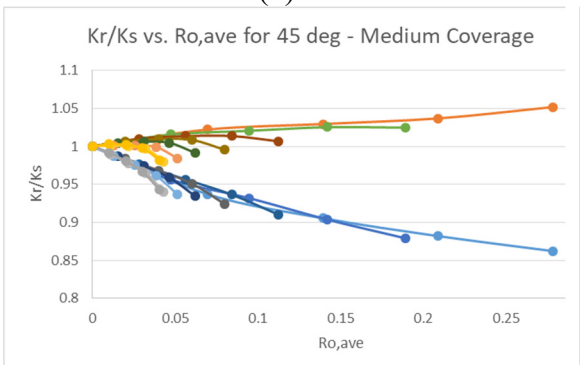

(d)

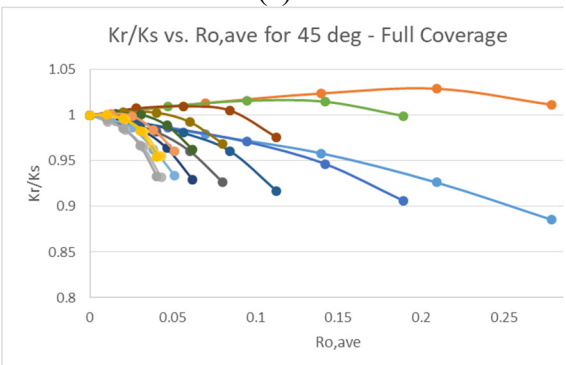

(e)

Figure 51 Effect of rotation on pressure loss coefficient for five different configurations

A similar trend can be seen in the 45 deg – less coverage channel. The lowest pressure coefficient ratio is $K_r/K_s = 0.74$ at the highest average rotation number $Ro_{,ave} = 0.27$. For the 45 deg – medium coverage case, pressure coefficients show a better correlation among different Reynolds numbers on both the LS and the TS. Also, there is a small increasing trend at lower Reynolds numbers (Re = 10k-15k) on the TS, up to $K_r/K_s = 1.05$ at $Ro_{,ave} = 0.28$. The reduction on pressure coefficient at the highest average rotation number on the LS is less than the 45 deg – less coverage case, where the $K_r/K_s = 0.86$. For the 45 deg – full coverage channel, there is an increasing than decreasing trend on the TS at lower Reynolds numbers (Re = 10k-25k). The lowest pressure coefficient ratio is $K_r/K_s = 0.89$ at $Ro_{,ave} = 0.28$ and the highest pressure coefficient ratio is $K_r/K_s = 1.03$ at $Ro_{,ave} = 0.21$.

The results show that, in general, the 45 deg– less coverage and 60 deg rib cases reduce the pressure drop on both LS and TS under rotation. For the 45 – deg angled ribs with medium and full coverages, a slight increase in pressure drop up to 5% was seen on the TS at lower Reynolds numbers and a pressure drop reduction up to ≈ 13% was seen on the LS at the highest average rotation number $Ro_{,ave} = 0.28$.

3.10 Summary – Internal Cooling

Heat transfer and pressure drop characteristics of this specific internal cooling channel have been identified under both stationary and rotating conditions. The rectangular cooling channel features a varying aspect ratio with AR = 4:1 in the first passage and AR = 2:1 in the second passage and a converging tip turn. The baseline smooth surface case and four other roughened surface cases have been considered. The rib configurations include 60 angled parallel ribs, 45 deg parallel ribs with less, medium and full coverages near the tip turn. Reynolds numbers from Re = 10k to 70k based on the first passage are covered. The highest rotation number achieved is Ro = 0.39 in the first passage and 0.16 in the second passage. The results indicate that the heat transfer and pressure drop are significantly affected by the geometrical design and the rib configuration of the test section. Substantial heat transfer reduction on the tip surface was observed under rotation. Extra care is needed in the internal cooling design of a comparable internal cooling channel, especially for the surfaces in or near the tip turn.

4. CONCLUSIONS

The efficiency, specific power output and reliability of gas turbine engines have been improving owing to the advanced technologies in cooling, material, design, manufacturing, and so on. With a higher heat load on the turbine components, there is an increasing demand for better cooling designs that ensure an adequate thermal protection of the components with a minimized overall coolant consumption. In this study, both external and internal cooling techniques have been considered. In the first part, detailed film cooling effectiveness distributions on a blade platform combined with several realistic cooling features were measured by the pressure sensitive paint technique. In the second part, stream-wise heat transfer data in a two pass (AR = 4:1 in the first passage and AR = 2:1 in the second passage) channel with a converging tip turn were obtained by the regionally averaged copper plate method under both stationary and rotating conditions. Based on the test results, the following conclusions can be drawn.

On the turbine platform, the upstream purge flow and the slashface leakage flow serve as good cooling sources. Both features provide good coolant film coverage and effectiveness on the platform. Nevertheless, the cooling benefit from the upstream purge flow is limited by the strong passage crossflows and the swirling effect under rotation. The performance of the slashface leakage flow have been documented via the contour plots. A higher blowing ratio is desired for an extended coverage toward upstream and effectiveness values are increased at a higher density ratio. In general, the fan-shaped hole design outperforms the cylindrical hole design on the endwall film cooling, including the upstream injection holes near the pressure side leading edge. The area average effectiveness

comparison reveals the overall film cooling protection on the platform over a wide range of blowing and density ratios. The results show that the optimal momentum flux ratios are I = 1.35 and I = 1.65 for the cylindrical and fan-shaped hole designs, respectively.

Heat transfer characteristics in the internal coolant passages are reported in terms of Nusselt number ratios. A total of five different rib configurations have been considered, including the smooth surface case, the 60 deg rib, and 45 deg rib with various rib coverages near the tip turn. The strength of the turn induced secondary flows and the turbulence intensity seem to be suppressed by the accelerating flow in the second passage. The geometry of the 180 deg tip turn together with the rib turbulators greatly alter the heat transfer characteristics, especially for the surfaces in and after the turn portion. Rotation effects on heat transfer on the leading and trailing surfaces in regions upstream and far downstream of the turn generally follow the trends as found in a constant aspect ratio channel. For the tip surface, significant heat transfer reduction was seen at certain rotation numbers for all surface configurations. Pressure loss coefficients on both the leading and trailing surfaces under rotation are presented. A decrease in the overall pressure penalty was observed for all roughened surface cases under rotation. To conclude, heat transfer and pressure loss characteristics are highly sensitive to the geometrical and rib design of the cooling channel and these factors should be taken into consideration in the design process.

REFERENCES

[1] Han, J. C., Dutta, S., and Ekkad, S., 2012, *Gas Turbine Heat Transfer and Cooling Technology*, CRC Press, Taylor & Francis Group, Florida.

[2] Chen, A. F., Shiau, C.-C., and Han, J.-C., 2017, "Turbine Blade Platform Film Cooling with Simulated Swirl Purge Flow and Slashface Leakage Conditions," J Turbomach, 139(3), p. 031012.

[3] Chen, A. F., Shiau, C.-C., and Han, J.-C., 2018, "Turbine Blade Platform Film Cooling with Fan-Shaped Holes under Simulated Swirl Purge Flow and Slashface Leakage Conditions," J Turbomach, 140(1), p. 011006.

[4] Bogard, D. G., and Thole, K. A., 2006, "Gas Turbine Film Cooling," J Propul Power, 22(2), pp. 249-270.

[5] Han, J. C., 2013, "Fundamental Gas Turbine Heat Transfer," J Therm Sci Eng Appl, 5(2), p. 021007.

[6] Goldstein, R. J., 1971, "Film Cooling," Advances in Heat Transfer, F. I. Thomas, and P. H. James, eds., Elsevier, pp. 321-379.

[7] Chen, A. F., Li, S.-J., and Han, J.-C., 2015, "Film Cooling for Cylindrical and Fan-Shaped Holes Using Pressure-Sensitive Paint Measurement Technique," Journal of Thermophysics and Heat Transfer, 29(4), pp. 775-784.

[8] Chen, A. F., Li, S.-J., and Han, J.-C., 2014, "Film Cooling with Forward and Backward Injection for Cylindrical and Fan-Shaped Holes Using Psp Measurement Technique," Proc. of the ASME Turbo Expo 2014, Paper No. GT2014-26232.

[9] Li, S.-J., Chen, A. F., Wang, W.-H., and Han, J.-C., 2014, "Experimental and Computational Film Cooling with Backward Injection for Cylindrical and Fan-Shaped Holes," Proc. of the ASME 15th International Heat Transfer Conference, Paper No. IHTC15-9584.

[10] Langston, L. S., 1980, "Crossflows in a Turbine Cascade Passage," Journal of Engineering for Power, 102(4), pp. 866-874.

[11] Langston, L. S., 2001, "Secondary Flows in Axial Turbines - a Review," Ann Ny Acad Sci, 934, pp. 11-26.

[12] Wang, H. P., Olson, S. J., Goldstein, R. J., and Eckert, E. R. G., 1997, "Flow Visualization in a Linear Turbine Cascade of High Performance Turbine Blades," J Turbomach, 119(1), pp. 1-8.

[13] Chyu, M. K., 2001, "Heat Transfer near Turbine Nozzle Endwall," Ann Ny Acad Sci, 934, pp. 27-36.

[14] Simon, T. W., and Piggush, J. D., 2006, "Turbine Endwall Aerodynamics and Heat Transfer," J Propul Power, 22(2), pp. 301-312.

[15] Friedrichs, S., Hodson, H. P., and Dawes, W. N., 1996, "Distribution of Film-Cooling Effectiveness on a Turbine Endwall Measured Using the Ammonia and Diazo Technique," J Turbomach, 118(4), pp. 613-621.

[16] Friedrichs, S., Hodson, H. P., and Dawes, W. N., 1999, "The Design of an Improved Endwall Film-Cooling Configuration," J Turbomach, 121(4), pp. 772-780.

[17] Jabbari, M. Y., Marston, K. C., Eckert, E. R. G., and Goldstein, R. J., 1996, "Film Cooling of the Gas Turbine Endwall by Discrete-Hole Injection," J Turbomach, 118(2), pp. 278-284.

[18] Burd, S. W., Satterness, C., and Simon, T., 2000, "Effects of Slot Bleed Injection over a Contoured End Wall on Nozzle Guide Vane Cooling Performance: Part Ii — Thermal Measurements," Proc. of the ASME Turbo Expo 2000, Paper No. 2000-GT-200.

[19] Knost, D. G., and Thole, K. A., 2005, "Adiabatic Effectiveness Measurements of Endwall Film-Cooling for a First-Stage Vane," J Turbomach, 127(2), pp. 297-305.

[20] Nicklas, M., 2001, "Film-Cooled Turbine Endwall in a Transonic Flow Field: Part Ii - Heat Transfer and Film-Cooling Effectiveness," J Turbomach, 123(4), pp. 720-729.

[21] Oke, R., Simon, T., Shih, T., Zhu, B., Lin, Y. L., and Chyu, M., 2001, "Measurements over a Film-Cooled, Contoured Endwall with Various Coolant Injection Rates," Proc. of the ASME Turbo Expo 2001, Paper No. 2001-GT-0140.

[22] Thrift, A. A., Thole, K. A., and Hada, S., 2012, "Effects of Orientation and Position of the Combustor-Turbine Interface on the Cooling of a Vane Endwall," J Turbomach, 134(6), p. 061019.

[23] Zhang, L. J., and Jaiswal, R. S., 2001, "Turbine Nozzle Endwall Film Cooling Study Using Pressure-Sensitive Paint," J Turbomach, 123(4), pp. 730-738.

[24] Gao, Z. H., Narzary, D., and Han, J. C., 2009, "Turbine Blade Platform Film Cooling with Typical Stator-Rotor Purge Flow and Discrete-Hole Film Cooling," J Turbomach, 131(4), p. 041004.

[25] Gao, Z. H., Narzary, D., Mhetras, S., and Han, J. C., 2012, "Upstream Vortex Effect on Turbine Platform Film Cooling with Typical Purge Flow," Journal of Thermophysics and Heat Transfer, 26(1), pp. 75-84.

[26] Liu, K., Yang, S. F., and Han, J. C., 2014, "Influence of Coolant Density on Turbine Platform Film-Cooling with Stator-Rotor Purge Flow and Compound-Angle Holes," J Therm Sci Eng Appl, 6(4), p. 041007.

[27] Wright, L. M., Blake, S. A., and Han, J. C., 2008, "Film Cooling Effectiveness Distributions on a Turbine Blade Cascade Platform with Stator-Rotor Purge and Discrete Film Hole Flows," J Turbomach, 130(3), p. 031015.

[28] Wright, L. M., Blake, S. A., Rhee, D. H., and Han, J. C., 2009, "Effect of Upstream Wake with Vortex on Turbine Blade Platform Film Cooling with Simulated Stator-Rotor Purge Flow," J Turbomach, 131(2), p. 021017.

[29] Papa, M., Srinivasan, V., and Goldstein, R. J., 2011, "Film Cooling Effect of Rotor-Stator Purge Flow on Endwall Heat/Mass Transfer," J Turbomach, 134(4), p. 041014.

[30] Takeishi, K., Oda, Y., and Kozono, S., 2015, "Experimental Study of Leakage Flow on Flow Field and Film Cooling of High Pressure Turbine Blade Platform," Proc. of the ASME Turbo Expo: Turbine Technical Conference and Exposition, Paper No. GT2015-42898.

[31] Suryanarayanan, A., Mhetras, S. P., Schobeiri, M. T., and Han, J. C., 2008, "Film-Cooling Effectiveness on a Rotating Blade Platform," J Turbomach, 131(1), p. 011014.

[32] Suryanarayanan, A., Ozturk, B., Schobeiri, M. T., and Han, J. C., 2010, "Film-Cooling Effectiveness on a Rotating Turbine Platform Using Pressure Sensitive Paint Technique," J Turbomach, 132(4), p. 041001.

[33] Rezasoltani, M., Schobeiri, M. T., and Han, J. C., 2014, "Experimental Investigation of the Effect of Purge Flow on Film Cooling Effectiveness on a Rotating Turbine with Nonaxisymmetric End Wall Contouring," J Turbomach, 136(9), p. 091009.

[34] Schobeiri, M. T., Lu, K., and Rezasoltani, M., 2015, "Effect of Non-Axisymmetric Contouring on Performance and Film Cooling of a Rotating Turbine Endwall Subjected to the Secondary Air Purge: A Combined Numerical and Experimental Study," Proceedings of the Institution of Mechanical Engineers, Part A: Journal of Power and Energy, 229(8), pp. 813-831.

[35] Barigozzi, G., Franchini, G., Perdichizzi, A., Maritano, M., and Abram, R., 2013, "Influence of Purge Flow Injection Angle on the Aerothermal Performance of a Rotor Blade Cascade," J Turbomach, 136(4), p. 041012.

[36] Stinson, M., Goldstein, R. J., Simon, T. W., Shu, F., and Nakamata, C., 2014, "Effect of Swirled Leakage Flow on Endwall Film-Cooling," Proc. of the 15th International Heat Transfer Conference, Paper No. IHTC 15-9600.

[37] Li, S.-J., Lee, J., Han, J.-C., Zhang, L., and Moon, H.-K., 2016, "Turbine Platform Cooling and Blade Suction Surface Phantom Cooling from Simulated Swirl Purge Flow," J Turbomach, 138(8), p. 081004.

[38] Yu, Y., and Chyu, M. K., 1998, "Influence of Gap Leakage Downstream of the Injection Holes on Film Cooling Performance," J Turbomach, 120(3), pp. 541-548.

[39] Piggush, J. D., and Simon, T. W., 2007, "Heat Transfer Measurements in a First-Stage Nozzle Cascade Having Endwall Contouring: Misalignment and Leakage Studies," J Turbomach, 129(4), pp. 782-790.

[40] Piggush, J. D., and Simon, T. W., 2012, "Flow Measurements in a First Stage Nozzle Cascade Having Endwall Contouring, Leakage, and Assembly Features," J Turbomach, 135(1), p. 011002.

[41] Cardwell, N. D., Sundaram, N., and Thole, K. A., 2005, "Effect of Midpassage Gap, Endwall Misalignment, and Roughness on Endwall Film-Cooling," J Turbomach, 128(1), pp. 62-70.

[42] Cardwell, N. D., Sundaram, N., and Thole, K. A., 2006, "The Effects of Varying the Combustor-Turbine Gap," J Turbomach, 129(4), pp. 756-764.

[43] Chowdhury, N. H. K., Shiau, C.-C., Han, J.-C., Zhang, L., and Moon, H. K., 2017, "Turbine Vane Endwall Film Cooling with Slashface Leakage and Discrete Hole Configuration," J Turbomach, 139(6), p. 061003.

[44] Shiau, C.-C., Chen, A. F., Han, J.-C., Azad, S., and Lee, C.-P., 2016, "Full-Scale Turbine Vane Endwall Film-Cooling Effectiveness Distribution Using Pressure-Sensitive Paint Technique," J Turbomach, 138(5), p. 051002.

[45] Shiau, C.-C., Chen, A. F., Han, J.-C., Azad, S., and Lee, C.-P., 2017, "Film Cooling Effectiveness Comparison on Full-Scale Turbine Vane Endwalls Using Pressure-Sensitive Paint Technique," J Turbomach, 140(2), p. 021009.

[46] Ranson, W. W., Thole, K. A., and Cunha, F. J., 2005, "Adiabatic Effectiveness Measurements and Predictions of Leakage Flows Along a Blade Endwall," J Turbomach, 127(3), pp. 609-618.

[47] Roy, A., Jain, S., Ekkad, S. V., Ng, W. F., Lohaus, A. S., and Crawford, M. E., 2014, "Heat Transfer Performance of a Transonic Turbine Blade Passage in Presence of Leakage Flow through Upstream Slot and Mateface Gap with Endwall Contouring," Proc. of the ASME Turbo Expo 2014, Paper No. GT2014-26476.

[48] Lynch, S., and Thole, K. A., 2017, "Heat Transfer and Film Cooling on a Contoured Blade Endwall with Platform Gap Leakage," J Turbomach, 139(5), p. 051002.

[49] Wright, L. M., McClain, S. T., and Clemenson, M. D., 2011, "Effect of Density Ratio on Flat Plate Film Cooling with Shaped Holes Using Psp," J Turbomach, 133(4), p. 041011.

[50] Barigozzi, G., Benzoni, G., Franchini, G., and Perdichizzi, A., 2005, "Fan-Shaped Hole Effects on the Aero-Thermal Performance of a Film-Cooled Endwall," J Turbomach, 128(1), pp. 43-52.

[51] Colban, W., Thole, K. A., and Haendler, M., 2008, "A Comparison of Cylindrical and Fan-Shaped Film-Cooling Holes on a Vane Endwall at Low and High Freestream Turbulence Levels," J Turbomach, 130(3), p. 031007.

[52] Bunker, R. S., 2005, "A Review of Shaped Hole Turbine Film-Cooling Technology," J Heat Trans, 127(4), pp. 441-453.

[53] Ekkad, S., and Han, J. C., 2015, "A Review of Hole Geometry and Coolant Density Effect on Film Cooling," Frontiers in Heat and Mass Transfer, 6(8), p. 013008.

[54] Han, J. C., and Rallabandi, A. P., 2010, "Turbine Blade Film Cooling Using Psp Technique," Frontiers in Heat and Mass Transfer, 1, p. 013001.

[55] Kline, S. J., and McClintock, F. A., 1953, "Describing Uncertainties in Single-Sample Experiments," Mechanical Engineering, 75(1), pp. 3-8.

[56] Han, J.-C., 2004, "Recent Studies in Turbine Blade Cooling," International Journal of Rotating Machinery, 10(6), pp. 443-457.

[57] Han, J.-C., and Chen, H.-C., 2006, "Turbine Blade Internal Cooling Passages with Rib Turbulators," J Propul Power, 22(2), pp. 226-248.

[58] Ligrani, P., 2013, "Heat Transfer Augmentation Technologies for Internal Cooling of Turbine Components of Gas Turbine Engines," International Journal of Rotating Machinery, Vol. 2013(Article ID 275653), pp. 1-32.

[59] Metzger, D. E., and Stan, R. L., 1977, "Entry Region Heat Transfer in Rotating Radial Tubes," Journal of Energy, 1(5), pp. 297-300.

[60] Mori, Y., Fukada, T., and Nakayama, W., 1971, "Convective Heat Transfer in a Rotating Radial Circular Pipe (2nd Report)," Int J Heat Mass Tran, 14(11), pp. 1807-1824.

[61] Morris, W. D., and Ayhan, T., 1979, "Observations on the Influence of Rotation on Heat Transfer in the Coolant Channels of Gas Turbine Rotor Blades," Proceedings of the Institution of Mechanical Engineers, 193(1), pp. 303-311.

[62] Han, J. C., 1988, "Heat Transfer and Friction Characteristics in Rectangular Channels with Rib Turbulators," J Heat Trans, 110(2), pp. 321-328.

[63] Han, J. C., and Park, J. S., 1988, "Developing Heat Transfer in Rectangular Channels with Rib Turbulators," Int J Heat Mass Tran, 31(1), pp. 183-195.

[64] Han, J. C., Park, J. S., and Ibrahim, M. Y., 1986, *Measurement of Heat Transfer and Pressure Drop in Rectangular Channels with Turbulence Promoters*, National Aeronautics and Space Administration, Scientific and Technical Information Branch.

[65] Park, J. S., Han, J. C., Huang, Y., Ou, S., and Boyle, R. J., 1992, "Heat Transfer Performance Comparisons of Five Different Rectangular Channels with Parallel Angled Ribs," Int J Heat Mass Tran, 35(11), pp. 2891-2903.

[66] Ekkad, S. V., Huang, Y., and Han, J.-C., 1998, "Detailed Heat Transfer Distributions in Two-Pass Square Channels with Rib Turbulators and Bleed Holes," Int J Heat Mass Tran, 41(23), pp. 3781-3791.

[67] Schüler, M., Zehnder, F., Weigand, B., von Wolfersdorf, J., and Neumann, S. O., 2010, "The Effect of Turning Vanes on Pressure Loss and Heat Transfer of a Ribbed Rectangular Two-Pass Internal Cooling Channel," J Turbomach, 133(2), p. 021017.

[68] Wagner, J. H., Johnson, B. V., and Hajek, T. J., 1991, "Heat Transfer in Rotating Passages with Smooth Walls and Radial Outward Flow," J Turbomach, 113(1), pp. 42-51.

[69] Wagner, J. H., Johnson, B. V., and Kopper, F. C., 1991, "Heat Transfer in Rotating Serpentine Passages with Smooth Walls," J Turbomach, 113(3), pp. 321-330.

[70] Han, J. C., Zhang, Y. M., and Kalkuehler, K., 1993, "Uneven Wall Temperature Effect on Local Heat Transfer in a Rotating Two-Pass Square Channel with Smooth Walls," J Heat Trans, 115(4), pp. 912-920.

[71] Taslim, M. E., Bondi, L. A., and Kercher, D. M., 1991, "An Experimental Investigation of Heat Transfer in an Orthogonally Rotating Channel Roughened with 45 Deg Criss-Cross Ribs on Two Opposite Walls," J Turbomach, 113(3), pp. 346-353.

[72] Wagner, J. H., Johnson, B. V., Graziani, R. A., and Yeh, F. C., 1992, "Heat Transfer in Rotating Serpentine Passages with Trips Normal to the Flow," J Turbomach, 114(4), pp. 847-857.

[73] Fu, W.-L., Wright, L. M., and Han, J.-C., 2005, "Heat Transfer in Two-Pass Rotating Rectangular Channels (Ar=1:2 and Ar=1:4) with 45 Deg Angled Rib Turbulators," J Turbomach, 127(1), pp. 164-174.

[74] Lei, J., Han, J.-C., and Huh, M., 2012, "Effect of Rib Spacing on Heat Transfer in a Two Pass Rectangular Channel (Ar = 2:1) at High Rotation Numbers," J Heat Trans, 134(9), p. 091901.

[75] Huh, M., Lei, J., and Han, J. C., 2012, "Influence of Channel Orientation on Heat Transfer in a Two-Pass Smooth and Ribbed Rectangular Channel (Ar=2:1) under Large Rotation Numbers," J Turbomach, 134(1), p. 011022.

[76] Griffith, T. S., Al-Hadhrami, L., and Han, J.-C., 2002, "Heat Transfer in Rotating Rectangular Cooling Channels (Ar=4) with Angled Ribs," J Heat Trans, 124(4), pp. 617-625.

[77] Saha, A. K., and Acharya, S., 2005, "Unsteady Rans Simulation of Turbulent Flow and Heat Transfer in Ribbed Coolant Passages of Different Aspect Ratios," Int J Heat Mass Tran, 48(23), pp. 4704-4725.

[78] Zhou, F., and Acharya, S., 2008, "Heat Transfer at High Rotation Numbers in a Two-Pass 4:1 Aspect Ratio Rectangular Channel with 45deg Skewed Ribs," J Turbomach, 130(2), p. 021019.

[79] Han, J. C., Chandra, P. R., and Lau, S. C., 1988, "Local Heat/Mass Transfer Distributions around Sharp 180 Deg Turns in Two-Pass Smooth and Rib-Roughened Channels," J Heat Trans, 110(1), pp. 91-98.

[80] Schabacker, J., Bölcs, A., and Johnson, B. V., 1998, "Piv Investigation of the Flow Characteristics in an Internal Coolant Passage with Two Ducts Connected by a Sharp 180° Bend," Proc. of the ASME 1998 International Gas Turbine and Aeroengine Congress and Exhibition, Paper No. 98-GT-544.

[81] Cheah, S. C., Iacovides, H., Jackson, D. C., Ji, H., and Launder, B. E., 1996, "Lda Investigation of the Flow Development through Rotating U-Ducts," J Turbomach, 118(3), pp. 590-596.

[82] Liou, T. M., and Chen, C. C., 1999, "Heat Transfer in a Rotating Two-Pass Smooth Passage with a 180° Rectangular Turn," Int J Heat Mass Tran, 42(2), pp. 231-247.

[83] Eifel, M., Caspary, V., Hönen, H., and Jeschke, P., 2010, "Experimental and Numerical Analysis of Gas Turbine Blades with Different Internal Cooling Geometries," J Turbomach, 133(1), p. 011018.

[84] Jenkins, S. C., Zehnder, F., Shevchuk, I. V., von Wolfersdorf, J., Weigand, B., and Schnieder, M., 2012, "The Effects of Ribs and Tip Wall Distance on Heat Transfer for a Varying Aspect Ratio Two-Pass Ribbed Internal Cooling Channel," J Turbomach, 135(2), p. 021001.

[85] Siddique, W., El-Gabry, L., Shevchuk, I. V., Hushmandi, N. B., and Fransson, T. H., 2012, "Flow Structure, Heat Transfer and Pressure Drop in Varying Aspect Ratio Two-Pass Rectangular Smooth Channels," Heat and Mass Transfer, 48(5), pp. 735-748.

[86] Siddique, W., Shevchuk, I. V., El-Gabry, L., Hushmandi, N. B., and Fransson, T. H., 2013, "On Flow Structure, Heat Transfer and Pressure Drop in Varying Aspect Ratio Two-Pass Rectangular Channel with Ribs at 45°," Heat and Mass Transfer, 49(5), pp. 679-694.

[87] Schüler, M., Dreher, H. M., Neumann, S. O., Weigand, B., and Elfert, M., 2011, "Numerical Predictions of the Effect of Rotation on Fluid Flow and Heat Transfer in an Engine-Similar Two-Pass Internal Cooling Channel with Smooth and Ribbed Walls," J Turbomach, 134(2), p. 021021.

[88] Rallabandi, A., Lei, J., Han, J.-C., Azad, S., and Lee, C.-P., 2014, "Heat Transfer Measurements in Rotating Blade–Shape Serpentine Coolant Passage with Ribbed Walls at High Reynolds Numbers," J Turbomach, 136(9), p. 091004.

[89] Yang, S.-F., Han, J.-C., Azad, S., and Lee, C.-P., 2015, "Heat Transfer in Rotating Serpentine Coolant Passage with Ribbed Walls at Low Mach Numbers," J Therm Sci Eng Appl, 7(1), p. 011013.

[90] Wu, H.-W., Zirakzadeh, H., Han, J.-C., Zhang, L., and Moon, H. K., 2018, "Heat Transfer in a Rib and Pin Roughened Rotating Multi-Pass Channel with Hub Turning Vane and Trailing-Edge Slot Ejection," J Therm Sci Eng Appl, p. 021011.

[91] Yang, S.-F., Wu, H.-W., Han, J.-C., Zhang, L., and Moon, H.-K., 2018, "Heat Transfer in a Smooth Rotating Multi-Passage Channel with Hub Turning Vane and Trailing-Edge Slot Ejection," Int J Heat Mass Tran, 109, pp. 1-15.

APPENDIX A

DRAWINGS OR PICTURES OF TEST SECTIONS

Some CAD drawings and a picture of the test sections are documented in this section.

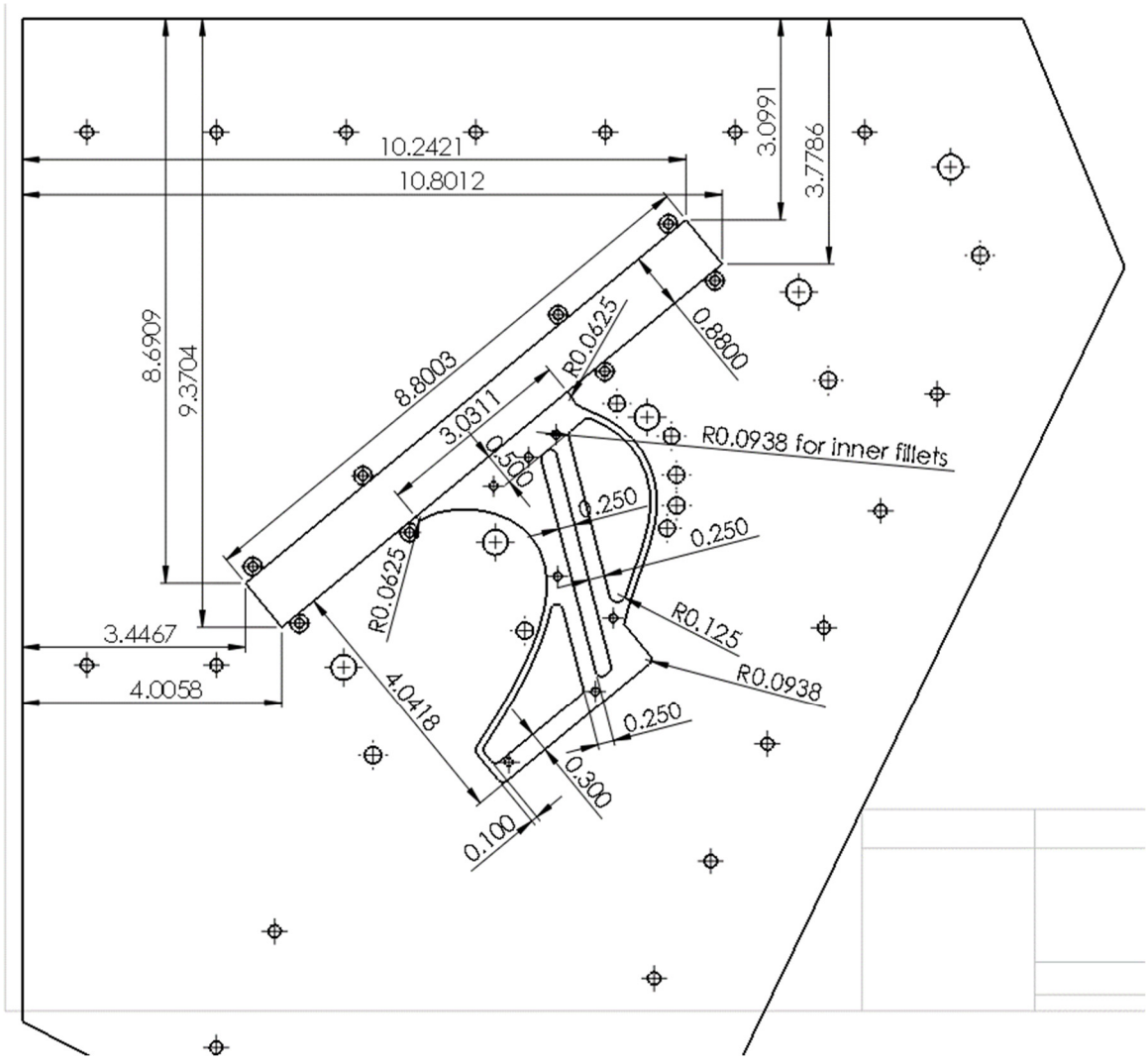

Figure 52 Design of the base plate of the five-blade linear blade cascade

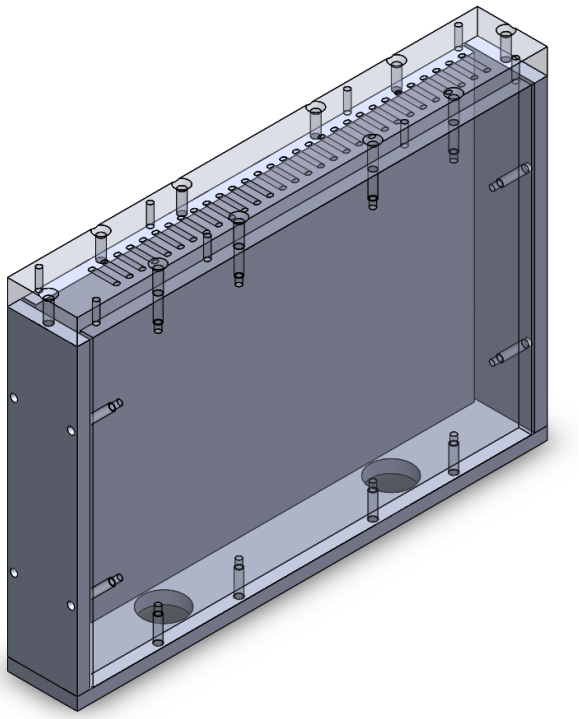

Figure 53 Design of the upstream purge plenum assembly with swirled injection holes

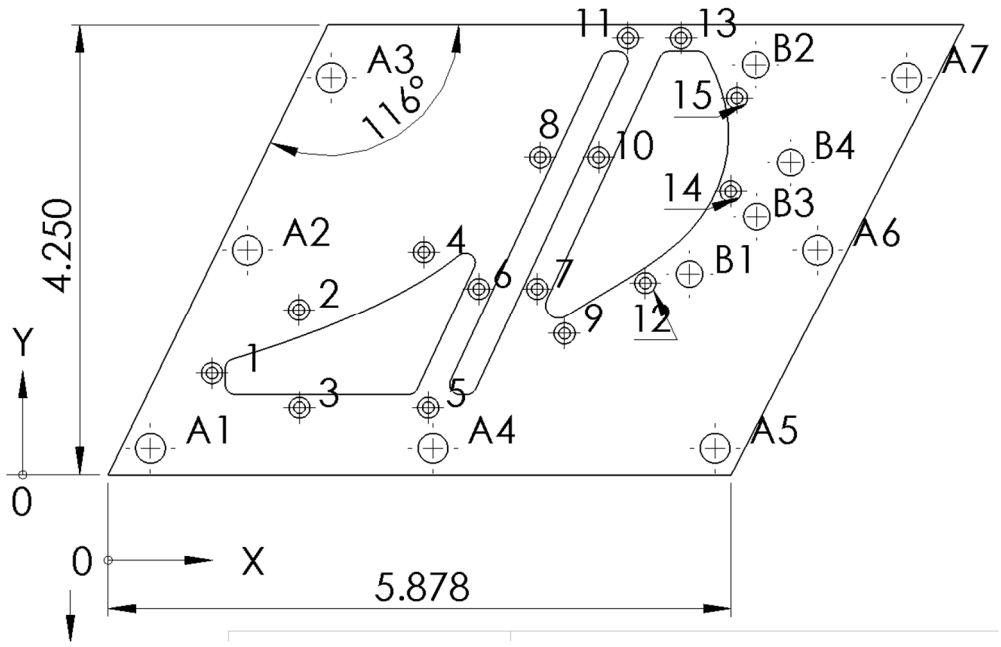

Figure 54 Design of the platform plenum adaptor

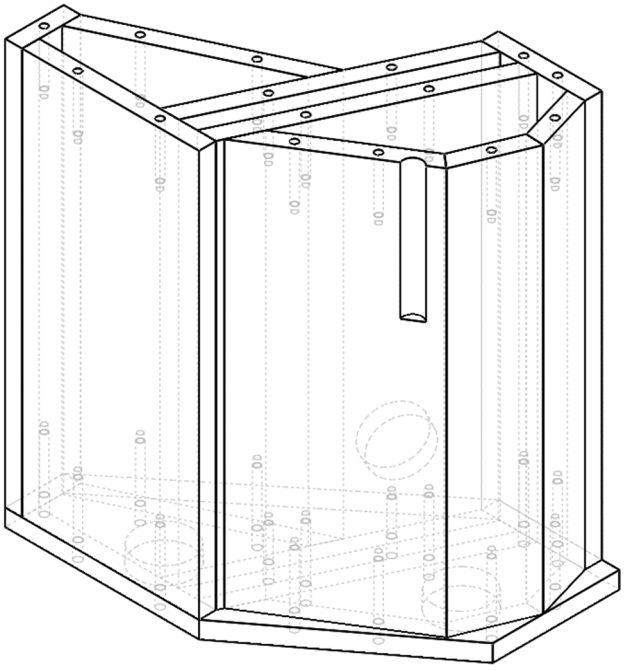

Figure 55 Design of the platform plenum

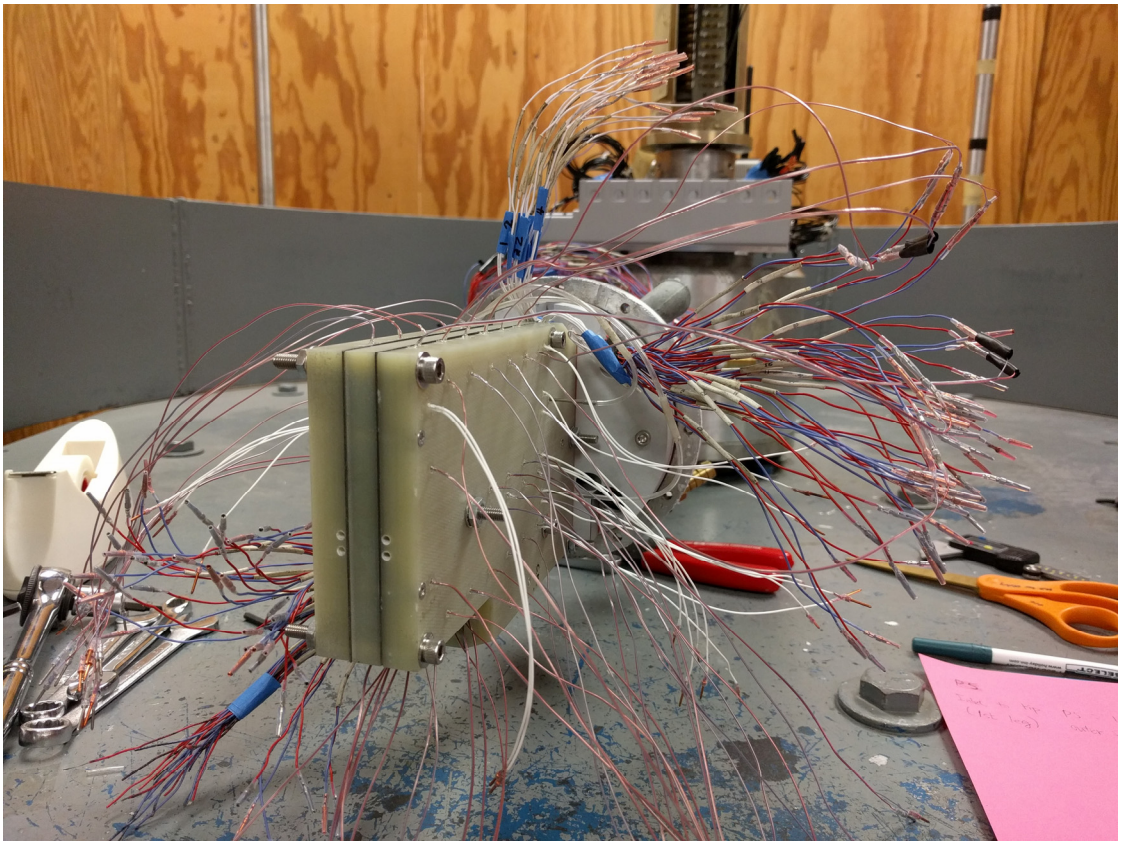

Figure 56 Internal cooling test section assembly on the rotating facility